




Universitetet  
i Stavanger

**FACULTY OF SCIENCE AND TECHNOLOGY**

## **MASTER'S THESIS**

Study program/specialization:  Petroleum Engineering, Reservoir Engineering	Spring semester, 2020  Open
Author: Christine Oswald	 (signature of author)
Faculty supervisor: Pål Østebø Andersen, Associate Professor in Reservoir Management  External supervisor: Eirik Jenssen, Reservoir Engineer	
Title of master's thesis:  Paleo Residual Gas Impact on Water Influx and Recovery Potential	
Credits: 30	
Keywords:  Trapped Gas Paleo Residual Gas Hysteresis Secondary Drainage ECLIPSE	Number of pages: 82  + supplemental material/other: 17  Stavanger, 15.07.2020



# Paleo Residual Gas Impact on Water Influx and Recovery Potential

Master Thesis in Cooperation with Wintershall Dea Norge As

Submitted 15.07.2020

*Graduate Student:*

Christine Oswald

MSc. Petroleum Engineering – Reservoir Engineering Student

Faculty of Energy Resources

*Company Supervision:*

Eirik Jenssen

Reservoir Engineer

*University Supervision:*

Pål Østebø Andersen

Associate Professor in Reservoir Management

## ABSTRACT

Whereas residual gas has been studied by many researchers, there has been little discussion about paleo residual gas. When encountered in a well, these dead gas columns are usually immobile, and the well is considered dry. However, under changing conditions, the gas can remobilize and contribute to economic recovery. The review of present publications revealed, that paleo gas remobilization during depletion takes place after overcoming a remobilization threshold ( $\Delta S_{g,remob}$ ). Prior studies have noted the importance of applying secondary drainage curves to reliably simulate the remobilization process.

This thesis presents a reservoir simulation study on modelling paleo residual gas expansion and remobilization during pressure depletion in a gas field case using the commonly applied Killough hysteresis model. In the presented field case, paleo residual gas is indicated by a wireline log showing gas columns below measured FWL and an unsuccessful drill stem test of these gas saturations.

The major contribution of this thesis is to provide an assessment of paleo residual gas and its general influence on incremental recovery potential and water influx. Investigating, how paleo residual gas will remobilize subjected to the field-specific prolific layers, i. e. an upper and lower high permeability layer, is a second aim of the study. A field-specific estimate of the incremental recovery potential and impact on water influx is elaborated.

An one-dimensional core model is used to derive reliable saturation functions from experimental data and a two-dimensional conceptual model is used to solve the above mentioned objectives. Different paleo column height ( $d_{paleo}$ ) scenarios are tested as well as different initial gas saturations in the paleo column ( $S_{gi,paleo}$ ) and different critical gas saturations.

The conclusions of this study are that paleo residual gas columns can be initialized by using imbibition negative  $P_c$  and hydrostatic equilibrium option, which is a standard option in commercial simulators.

Paleo gas saturations increase recovery potential during depletion with increasing  $d_{paleo}$ , with increasing  $S_{gi,paleo}$  and decreasing  $\Delta S_{g,remob}$ . Disregarding  $\Delta S_{g,remob}$  leads to overestimation of the recovery potential.

Paleo gas saturations increase water production during depletion with increasing  $d_{paleo}$ , with decreasing  $S_{gi,paleo}$  and increasing  $\Delta S_{g,remob}$ . Disregarding  $\Delta S_{g,remob}$  leads to underestimation of the water production. The water produced in this model originates from two different regions: from the aquifer and from the paleo gas column due to expulsion by depletion induced gas expansion before remobilization. The influence of the aquifer is dimmed by the presence of paleo residual gas due to water mobility reduction.

Due to the field-specific weak aquifer, the counteracting effect of paleo gas is less significant on reducing water production originating from the aquifer influx. Water production is less related to the aquifer influx but more result of water expulsion due to gas expansion before remobilization. The field-specific high permeability layers cause increased total gas production and increase the risk for earlier water breakthrough. Water breakthrough appears significantly earlier and more pronounced with high permeability layers.

## ACKNOWLEDGEMENTS

When I started writing this thesis in January 2020, nobody could have imagined what was lying in front of us. The global COVID-19 pandemic changed the daily life of the world within weeks. And so my thesis work changed drastically: From starting with a day-to-day office life as a team member of my Subsurface Team in Wintershall Dea, I soon had to turn my dormitory room of 12 m<sup>2</sup> into a home office. My refuge to recover became my own little ‘prison cell’ for almost 18 weeks.

I want to thank my supervisors Eirik Jenssen from Wintershall Dea and Pål Østebø Andersen from the University of Stavanger for all their support, even when only digitally possible: Pål, thank you for shedding light in the mysteries of core flooding and for answering e-mails at every day- and nighttime. Eirik, thank you for filling my ‘reservoir engineering toolbox’ with valuable advices and practicable strategies and for all your constructive feedback.

I appreciate the support of my team in Wintershall Dea, who welcomed me warmly, cared from day one and cheered me up with every Teams meeting during the home office period.

I acknowledge the support of Wintershall Dea. The company provided me with everything I needed during my thesis work.

My warmest thanks go to Germany to my family, to my boyfriend and to my friends, who always had an open ear for my worries and who never stopped believing in me during my time here in Norway – especially during the demanding time of the thesis. Thank you all, I love you.

# CONTENTS

Abstract .....	III
Acknowledgements .....	IV
Contents.....	V
Figures .....	VII
Tables .....	IX
Diagrams .....	X
Abbreviations .....	XI
Symbols.....	XII
Indices .....	XIII
1 Introduction .....	1
1.1 Motivation .....	1
1.2 Problem Description .....	1
1.3 Objectives .....	1
1.4 Methodology.....	2
2 Paleo Residual Gas.....	3
2.1 Formation of Paleo Residual Gas .....	3
2.2 Identification and Quantification of Paleo Residual Gas .....	5
2.3 Drainage and Imbibition: Paleo Residual Gas (Re)Mobilization .....	7
2.4 Reservoir Engineering Fundamentals.....	9
2.5 Gas Trapping Models .....	16
2.6 Hysteresis Models.....	19
2.7 Residual Gas Studies .....	22
3 Gas Field Case Study .....	26
3.1 Overview .....	26
3.2 Paleo Residual Gas in the field.....	29
4 One-Dimensional Core Model .....	32
4.1 Data Origin .....	32
4.2 Model Assumptions .....	33
4.3 Creation of the Saturation Functions for the History Match .....	36
5 Two-Dimensional Conceptual Model .....	40
5.1 Data Origin .....	40
5.2 Initialization and Saturation Regions .....	42
5.3 Paleo Column Height.....	47
5.4 Aquifer.....	48

6	Results and Discussion.....	50
6.1	Core Model Simulations.....	50
6.2	Conceptual Model Simulations .....	57
6.3	Limitations and Further Work .....	77
7	Conclusions .....	80
7.1	Literature Study .....	80
7.2	Simulation Study .....	80
7.3	Implications for Field Case.....	82
	Bibliography.....	XIV

## FIGURES

Figure 2.1-1: Conceptual illustration of formation of residual gas saturation by capillary jump .....	4
Figure 2.1-2: Top seal leak causing formation of paleo residual gas .....	5
Figure 2.3-1: Hysteresis cycle before charge to primary drainage to imbibition over remobilization threshold to secondary drainage, saturation intervals indicated with dotted arrows .....	7
Figure 2.4-1: Contact angle hysteresis in water-wet reservoir: (a) imbibition; (b) drainage, ..	10
Figure 2.4-2: Water entrapment in water-wet reservoir between grains: increasing $S_w$ with increasing radius, .....	11
Figure 2.4-3: Capillary pressure function, .....	11
Figure 2.6-1: Non-wetting phase hysteretic relative permeability characteristics, including scanning curve (dashed black) .....	20
Figure 2.7-1: Paleo contact detected from deviation of saturation behavior in transition zone. Left: $S_w$ from logs versus $S_w$ by J-function, fitting values (blue dots) and deviating values (orange crosses). Right: primary drainage (blue) imbibition (red), drainage overlay (green), from Cense et al., (2016). .....	22
Figure 3.1-1: Well location of wells A and C in the East structure. ....	26
Figure 3.2-1: Log data of well A showing paleo residual gas saturations .....	30
Figure 4.2-1: One-dimensional core simulation model with initial water saturation.....	34
Figure 5.1-1: Two-dimensional conceptual model with attached aquifer model (red) .....	40
Figure 5.1-2: High permeability layer scenarios I to III from left to right.....	41
Figure 5.2-1: Example for initial fluid distribution, short transition zone .....	43
Figure 5.2-2: Saturation regions of conceptual model, exemplified for paleo gas column height of 147 m. ....	44
Figure 5.3-1: Example for initial GDT scenario .....	48
Figure 6.1-1: Uniform gas distribution during expansion in core model at $t = 5,089$ just before remobilization. ....	54
Figure 6.2-1: Fundamental sensitivity runs on conceptual model .....	58
Figure 6.2-2: Observation grid block (2,1,32) in live column: gas production starts immediately without saturation threshold.....	60
Figure 6.2-3: Observation grid block (7,1,58) in paleo column: gas remobilizes only after achieving its $S_{gc}$ as illustrated by black arrows.....	60
Figure 6.2-4: Cum. gas production vs. time, $S_{gi,paleo}$ 0,42: cum. gas production increases with increasing $d_{paleo}$ , becomes more sensitive towards $\Delta S_{g,remob}$ with increasing $d_{paleo}$ and with increasing $S_{gi,paleo}$ . ....	61
Figure 6.2-5: Cum. gas production vs. time, $S_{gi,paleo}$ 0,5: cum. gas production increases with increasing $d_{paleo}$ , becomes more sensitive towards $\Delta S_{g,remob}$ with increasing $d_{paleo}$ and with increasing $S_{gi,paleo}$ . ....	62
Figure 6.2-6: Cum. gas production vs. time, $S_{gi,paleo}$ 0,6: cum. gas production increases with increasing $d_{paleo}$ , becomes more sensitive towards $\Delta S_{g,remob}$ with increasing $d_{paleo}$ and with increasing $S_{gi,paleo}$ . ....	62
Figure 6.2-7: Gas production rate over time for different $\Delta S_{g,remob}$ : a higher $\Delta S_{g,remob}$ causes an earlier fall off of the production plateau. ....	63
Figure 6.2-8: Cum. gas production vs time, subjected to absence of high permeability layer: absence of the high permeability layers for the paleo gas bearing cases with $\Delta S_{g,remob}$ shows a reduction in the total gas production .....	65

Figure 6.2-9: Cum. gas production vs time related to lower KRG (dashed): reduction of KRG to 0,5 (0,1) leads to a decrease in the cumulative gas production .....	66
Figure 6.2-10: Cum. water production vs. time for $S_{gi,paleo}$ 0,42: cum. water production increases with increasing $d_{paleo}$ , becomes more sensitive towards $\Delta S_{g,remob}$ with increasing $d_{paleo}$ and with decreasing $S_{gi,paleo}$ .....	68
Figure 6.2-11: Cum. water production vs. time for $S_{gi,paleo}$ 0,5: cum. water production increases with increasing $d_{paleo}$ , becomes more sensitive towards $\Delta S_{g,remob}$ with increasing $d_{paleo}$ and with decreasing $S_{gi,paleo}$ .....	68
Figure 6.2-12: Cum. water production vs. time for $S_{gi,paleo}$ 0,6: cum. water production increases with increasing $d_{paleo}$ , becomes more sensitive towards $\Delta S_{g,remob}$ with increasing $d_{paleo}$ and with decreasing $S_{gi,paleo}$ .....	69
Figure 6.2-13: Water production vs. time with constant $S_{gi,paleo}$ of 0,42: presence of high permeability layers causes earlier and stronger water breakthrough. ....	70
Figure 6.2-14: Total aquifer production vs. time: smaller $d_{paleo}$ is connected to higher aquifer influx; higher $\Delta S_{g,remob}$ leads to lower aquifer influx .....	72
Figure 6.2-15: Total water production vs. time: smaller $d_{paleo}$ is connected to lower total water production .....	73
Figure 6.2-16: Field pressure vs. time: higher $\Delta S_{g,remob}$ leads to higher pressure support .....	73
Figure 6.2-17: Detail of cum. water production vs. time vs aquifer strength: earlier water breakthrough due to stronger aquifer behavior of the case without paleo gas is extremely high compared to the paleo gas cases .....	75
Figure 6.2-18: Log. relative water permeability vs. time: presence of paleo gas reduces water relative permeability substantially .....	76
Figure 6.2-19: Detail of cum. water production vs. time: delayed water breakthrough in the absence of high permeability layers.....	77



## TABLES

Table 2.6-1: ODD3P hysteresis cycles .....	21
Table 2.7-1: Analogues: gas saturation threshold for remobilization .....	25
Table 3.1-1: Rounded reservoir fluid composition of the East structure .....	29
Table 3.2-1: Average properties of well A.....	30
Table 3.2-2: Gas-Down-To scenarios inferred from well logs .....	31
Table 4.1-1: Comparison of cores .....	32
Table 4.2-1: Initial conditions and boundary conditions of imbibition – low rate water flooding – study.....	35
Table 4.2-2: Initial conditions and boundary conditions of secondary drainage – depletion – study.....	36
Table 4.3-1: Saturation endpoints from SCAL report.....	37
Table 4.3-2: Curve-fitted and history matched Corey exponents. ....	37
Table 5.1-1: Properties of conceptual model.....	42
Table 5.2-1: Saturation endpoints applied in the conceptual model. ....	47
Table 5.3-1: Gas-Down-To scenarios for simulation study, GWC assumed to be at 4300 mTVDSS.....	48
Table 5.4-1: Aquifer parameters for weak aquifer behavior. ....	49
Table 6.2-1: Preliminary recovery potential of paleo residual gas (KRG = 1) .....	64
Table 6.2-2: Preliminary recovery potential of paleo gas (KRG = 0,5).....	66
Table 6.2-3: Preliminary recovery potential of paleo gas (KRG = 0,1).....	66
Table 6.2-4: Water influx due to paleo residual gas .....	71
Table 6.2-5: Aquifer parameters for weak and strong aquifer behavior. ....	74
Table 6.2-6: Effect of aquifer influx on total water production water (both high permeability layers).....	74
Table 6.2-7: Effect of aquifer influx on total water production water (no high permeability layers).....	76

## DIAGRAMS

Diagram 2.5-1: Typical initial residual non-wetting-phase (gas) saturations curves.....	18
Diagram 2.5-2: Comparison of Land's trapping model equ. (2.5-1) with Jerauld's trapping model equ. (2.5-4) and Mulyadi's trapping model equ. (2.5-5); grey curves of Diagram 2.5-1. ....	19
Diagram 2.7-1: No trends visible: residual gas saturation and critical gas saturation versus log. permeability from Table 2.7-1. ....	25
Diagram 3.1-1: Hydrostatic pressure (blue) and reservoir pressure (black) of the East structure versus depth: visible overpressurization .....	28
Diagram 4.3-1: Curve-fitted and history matched Corey relative permeabilities: primary drainage (dashed), imbibition (solid) and secondary drainage (dotted) for water (blue) and gas (red).....	38
Diagram 4.3-2: Curve-fitted and history matched capillary pressure curves. Secondary drainage not visible as it is assumed to be equal to imbibition curve.....	39
Diagram 5.2-1: Pc input data for conceptual model, paleo initial gas saturation 0,5 .....	43
Diagram 5.2-2: Correlation between residual gas saturation and critical gas saturation from Table 2.7-1 (analogues) and sensitivity cases.....	46
Diagram 5.2-3: Correlation between residual gas saturation and remobilization threshold from Table 2.7-1 (analogues) and sensitivity cases.....	46
Diagram 6.1-1: Final match of cumulative gas volume produced over pore volumes injected. All relevant features of the historical curve displayed by match.....	50
Diagram 6.1-2: Final match of gas saturation over pore volumes injected. All relevant features of the historical curve displayed by match.....	51
Diagram 6.1-3: Final match of differential pressure over pore volumes injected. All relevant features of the historical curve displayed by match.....	51
Diagram 6.1-4: Differential pressure can be subdivided into three zones depending on the fluid production .....	52
Diagram 6.1-5: Changing the gas Corey exponent affects mainly the transition zone between gas and water production of the differential pressure curve: smaller $N_g$ causes smaller $\Delta P$ peak .....	52
Diagram 6.1-6: Changing the water Corey exponent affects mainly the outer zones of the differential pressure curve dominated by gas or water production resp.: smaller $N_w$ causes smaller $\Delta P$ in gas dominated zone and higher $\Delta P$ in the water dominated zone.....	53
Diagram 6.1-7: Secondary drainage model gas production rate and gas saturation obeying the critical gas saturation $S_{gc} = 0,318$ ; top: full 5 hours of simulation; bottom: enlarged first 0,5 hours of simulation .....	55
Diagram 6.1-8: No effect of varying either Corey exponent on gas or water production rate over time .....	56
Diagram 6.1-9: Varying maximum relative permeability has influence on gas or water production rate over time: Increasing KRW or decreasing KRG delays water and gas production; top: varying KRW, bottom: varying KRG .....	57

## ABBREVIATIONS

### $\Delta$

$\Delta S_{g,remob.}$  *remobilization threshold*

### B

BHP. *bottom hole pressure*

BV. *bulk volume*

### D

$d_{paleo.}$  *paleo column height*

DST. *drill stem test*

### F

FFM. *full field model*

Fm. *Formation*

FWL. *free water level*

### G

GDT. *Gas-Down-To*

GIP. *gas in place*

### M

MBE. *mass balance equations*

### N

NMR. *nuclear magnetic resonance*

### O

ODD3P. *Odd Hustad's three phase hysteresis model*

OGIP. *original gas in place*

### P

pu. *per unit*

PV. *pore volume*

### R

RF. *recovery factor*

### S

$S_{gi,paleo.}$  *initial gas saturation in paleo column*

### T

TVDSS. *true vertical depth below mean sea level*

## SYMBOLS

<b>B</b>	<b>Q</b>
B. <i>formation volume factor</i>	q. <i>flow rate</i> Q. <i>source term</i>
<b>C</b>	<b>R</b>
c. <i>entry pressure in Skjaeveland correlation, compressibility</i> C. <i>Land's trapping constant</i>	r. <i>radius</i> R. <i>resistivity</i>
<b>D</b>	<b>S</b>
d. <i>vertical distance from a reference level</i>	S. <i>saturation</i>
<b>G</b>	<b>T</b>
g. <i>gravity acceleration</i>	T. <i>temperature, aquifer time constant</i>
<b>J</b>	<b>V</b>
J. <i>Leverett J-function, productivity index in aquifer model</i>	v. <i>Darcy velocity</i> V. <i>volume</i>
<b>K</b>	<b>Z</b>
k. <i>absolute permeability</i> KRG. <i>maximum gas relative permeability</i> KRW. <i>maximum water relative permeability</i>	z. <i>gas compressibility factor</i>
<b>L</b>	<b>MISC</b>
L. <i>core length</i>	$\gamma$ . <i>specific gravity</i>
<b>M</b>	<b><math>\Theta</math></b>
M. <i>mobility ratio</i>	$\Delta$ . <i>difference</i> $\mu$ . <i>viscosity</i> 1/a. <i>pore size distribution index in Skjaeveland correlation</i>
<b>N</b>	$\Theta$ . <i>contact angle</i> $\lambda$ . <i>phase mobility</i> $\sigma$ . <i>surface tension</i>
N. <i>Corey exponent</i>	$\Phi$ . <i>porosity</i> $\psi$ . <i>fluid potential</i>
<b>P</b>	
p. <i>phase pressure</i> P. <i>pressure</i>	

## INDICES

### A

a. *aquifer*

### B

B. *backpressure*

### C

c. *critical (gas), capillary*  
crit. *critical (water)*

### D

drain. *drainage*

### F

f. *flowing*

### G

g. *gas*  
GWC. *referring to GWC*

### I

i. *grid block i, initial*  
imb. *imbibition*

### L

l. *liquid, i.e. water, oil, gas*

### M

max. *maximum*  
mf. *mud filtrate*  
mob. *mobilized*

### N

norm. *normalized*

### O

o. *oil*

### R

r. *relative, residual*  
remob. *remobilization*

### T

t. *time, total*

### W

w. *water*

### X

xo. *near wellbore*

# 1 INTRODUCTION

## 1.1 Motivation

Natural gas might play an important role in addressing the issue of a growing global demand for carbon dioxide reduced energy supply. With the transition towards a more natural gas-based fossil fuel supply, a step into more sustainable energy usage might be reached. Hence it is next to obvious economic reasons a key objective to maximize production from gas reservoirs.

Whereas residual gas has been studied by many researchers, there has been little discussion about paleo residual gas. Paleo residual gas can form when due to geological movements water encroaches into a gas accumulation. This creates a discontinuous phase, which is usually immobile when encountered in a well and may lead to the well being considered dry. However, under changing conditions, the gas can remobilize and contribute to economic recovery.

This thesis aims to be a valuable contribution to understand the impact of paleo residual gas on water influx and recovery potential. This shall be achieved by a vast literature research and a sensitivity analysis of the encountered mechanisms at lab scale in a core model and at field scale in a conceptual cross-sectional model.

## 1.2 Problem Description

Many gas reservoirs at the appraisal stage exhibit evidence of gas saturations below free water level (FWL). Paleo residual gas can expand upon pressure depletion and hence cause additional gas production as well as increase of water production (Taggart, 2019).

Paleo residual gas might also be present in the presented gas field. First evidence is given by one appraisal well of the field from the 1980s. The wireline log of this exploration well, located in the East structure, provides indications of gas columns below measured FWL. The log shows residual gas located circa 150 m below the FWL. A drill stem test (DST) of these gas saturations showed a period of water production before limited gas production. The reason for the limited mobilization of the gas during the DST might be indicating residual gas expansion under pressure depletion.

## 1.3 Objectives

The major contribution of this thesis is to provide an assessment of paleo residual gas and its general influence on incremental recovery potential and water influx. Investigating, how paleo residual gas will remobilize subjected to the field-specific prolific layers, i. e. an upper and lower high permeability layer, is a second aim of the study. A field-specific estimate of the incremental recovery potential and impact on water influx is elaborated.

In summary, the following aspects shall be investigated:

- How can paleo gas columns be initialized?
- What is the influence of increasing paleo gas column height on water influx and recovery potential?

- What is influence of increasing initial paleo gas column saturation on water influx and recovery potential?
- What is the influence of different critical gas saturations on water influx and recovery potential?
- How will the field-specific high permeability layers affect the paleo gas production and the water influx?
- Is the presence of paleo gas affecting the aquifer behavior?

#### **1.4 Methodology**

The present thesis is formed by a symbiosis of literature, publications, experimental laboratory data and a simulation study. The foundation of the thesis originates from reservoir engineering fundamentals and widely known knowledge about residual saturations. The review of present publications allows for conclusions about how to access and model paleo residual gas. Some crucial values, e. g. residual gas saturation, are additionally supported by experimental data and can such supply solid groundwork for the simulations. Nevertheless, the field-specific data is limited, since the gas field is green field and not yet in production.

An one-dimensional core model is used to derive reliable saturation functions from experimental data and a two-dimensional conceptual model is used to solve the above mentioned objectives. Different paleo column height scenarios are tested as well as different initial gas saturations in the paleo column and different critical gas saturations.

The present thesis is composed of seven chapters, divided into three sections: The introductory section consists of the first three chapters; the core section contains the following two chapters; the results and conclusions are covered by the last two chapters.

The introductory section starts in chapter 1 with the motivation of the thesis and a problem description as well as a list of objectives and a description how these are assessed within the thesis. The 2nd chapter is concerned with the theory and literature foundation about paleo residual gas. It begins with the paleo residual gas fundamentals, focusing on formation, identification, quantification and remobilization of paleo residual gas. The relevant reservoir engineering fundamentals used in this study follow. Models relevant for residual gas modelling are presented, i.e. trapping models and hysteresis models and relevant literature regarding experimental and simulation studies is summarized. The first section of the thesis is concluded by an overview of relevant properties of field case in chapter 3.

The thesis will then go on to the main section. The objectives of this thesis shall be investigated by starting with a core-scale model in chapter 4 to examine the remobilization of residual gas and develop reliable saturation functions based on experimental data. The main findings of the core scale-model will be implemented in a cross-sectional conceptual model in chapter 5 to develop an initialization concept and give insight in water influx and recovery potential under the interpreted imbibition state.

The remaining part of the thesis proceeds as follows: Chapter 6 analyses and discusses the results of simulations undertaken during the scope of the thesis and chapter 7 summarizes the conclusions.

## 2 PALEO RESIDUAL GAS

Paleo residual gas can broadly be described as pore space occupied by an immobile gas phase, which in water-wet sandstones is usually encompassed by a mobile water phase.

According to Cross, et al. (2008) paleo residual gas is a low, at reservoir conditions irreducible gas saturation that remains when paleo traps leak. Woods, et al. (2012) describe paleo residual gas as apparent residual gas below the live gas column. Taggart (2019) defines paleo residual gas as an accumulation having finite gas saturation that extends a distance below the FWL at the appraisal resp. discovery time.

The understanding of paleo residual gas is of vast importance for exploration success and reliable field performance predictions. The correct petrophysical quantification of rock properties is strongly dependent on the consideration of paleo residual gas (Woods et al., 2012). Sub-chapter 2.2 will discuss these issues. For example, it is necessary to perform hydrocarbon correction for density porosity calculations.

Woods, et al. (2012) and Cense, et al. (2016) underline the importance of modelling saturation-height function based on the imbibition model instead of the widely used drainage model when paleo residual gas saturations are present. Using the drainage model would involuntarily result in an overestimation of the water saturation in transition zone. Compared to a fully water-saturated rock, a weakened aquifer support is encountered within the residual gas zone due to a substantial reduction of the water relative permeability.

According to Babadimas (2017) and Woods et al. (2012) residual gas expansion and remobilization allows potentially for additional pressure support (also Cense, et al. (2016)) and additional recovery (also Taggart (2019)).

### 2.1 Formation of Paleo Residual Gas

The formation of residual gas saturations  $S_{gr}$  embodies a multitude of concepts. To enhance the understanding of the mechanisms, the thesis distinguishes between micro-scale and macro-scale formation of residual gas saturations in the following sub-sub-chapters. The micro-scale mechanisms include *pore-scale* mechanisms. The macro-scale mechanisms encompass *paleo* and *production* induced mechanisms. A discussion of relevant trapping models can be found in sub-chapter 2.5.

#### 2.1.1 Micro-Scale

During drainage the non-wetting phase enters the largest pores first, later followed by pores decreasing in size. During imbibition pores are invaded in the opposite order: The smallest pores are invaded first by the wetting phase. Drainage and imbibition processes are described in detail in sub-chapter 2.3.

The main mechanism on pore-scale causing entrapment of gas behind the advancing water layer in sandstones is the formation of  $S_{gr}$  by capillary jumps according to Legatski, et al. (1964). As the waterfront moves unevenly in the rock, capillary forces result in a jump of the water across the pore space when constriction was first created by water bridging. Figure 2.1-1 visualizes



schematically the formation of residual gas saturation caused by capillary jumps during water encroaching.

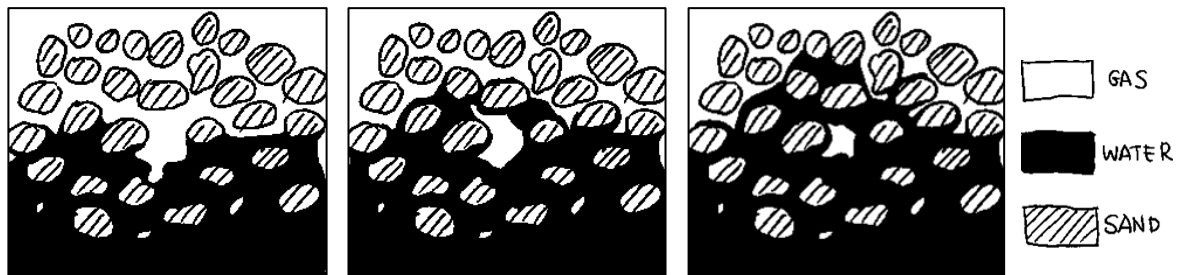


Figure 2.1-1: Conceptual illustration of formation of residual gas saturation by capillary jump (Legatski et al., 1964).

These trapped gas saturations are immobile, as the capillary entry pressures of the pore throats exceed buoyancy forces at reservoir conditions (Cross et al., 2008).

The residual gas phase needs to expand to reconnect in the water phase to remobilize. This expansion is only possible under changing of the present conditions: E. g. during pressure depletion the bubble clusters expand and merge (Babadimas, 2017).

### 2.1.2 Macro-Scale

The macro-scale processes are distinguished by time of their occurrence. The term *production* mechanisms is used to refer to the processes of residual gas formation initiated by gas production in the reservoir, whereas the *paleo* mechanisms refer to processes during the structure's charging history respectively.

*Production* induced residual gas saturations in developed accumulations are the most common ones (O'Sullivan, et al., 2010). Due to high production rates in order to out-run aquifer influx, residual gas saturations become trapped behind the encroaching water front (Babadimas, 2017). These trapped volumes can be produced by inducing pressure depletion with e. g. substantial withdrawal of water volumes.

In this study the focus lies on *paleo* mechanisms, as the field under investigation is undeveloped. Several authors describe various paleo processes related to the geological history of the hydrocarbon fields. O'Sullivan et al. (2010), Woods, et al. (2012) and Taggart (2019) provide a number of important geological mechanisms leading to paleo residual gas columns below the FWL. The authors present the origin of paleo gas accumulations as variations in charging history, e.g. leakage (breached or tilted trap, fault leaks and uplift) and aquifer movement (gas replaced by water encroachment) over geological time. The anticipated charging history of the field case is discussed in sub-sub-chapter 3.1.3. For the present field case the likely paleo mechanism is a top seal leak and is shown in Figure 2.1-2.

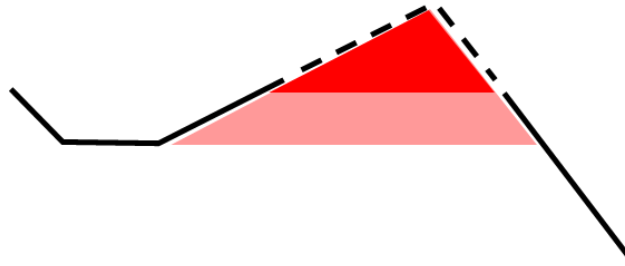


*Figure 2.1-2: Top seal leak causing formation of paleo residual gas as described by O'Sullivan et al. (2010).*

Naturally, next to formation the preservation of the accumulations is a key factor for encountering paleo accumulations at present date. O'Sullivan et al. (2010) identified six important elements for the preservation of a residual hydrocarbon column: timing, type of hydrocarbon preserved, reservoir quality, amount of water washing, amount of bacterial action and temperature.

## **2.2 Identification and Quantification of Paleo Residual Gas**

### *2.2.1 Identification*

Due to the various impacts on exploration success and consistent field performance predictions, the presence of residual gas must be identified reliably. Two key aspects must be proven for identifying residual gas: Water has to appear as the continuous phase and gas has to be present (Woods et al., 2012). This sub-chapter is dedicated to the various possibilities to identify residual gas.

It is now well established to use seismic interpretation as a strong tool for an early reservoir assessment. Even hydrocarbon accumulations can be identified with great precision. Nevertheless when identifying gas, it is not possible to distinguish between live or residual gas columns as soon as the gas saturation  $S_g$  exceeds a certain magnitude. Woods, et al. (2012) found that declarations of live or residual gas fail at a  $S_g$  of 10 percent. Other researchers however, have identified lower saturations as already problematic: Domenico (1974) describes 5 percent  $S_g$  as a challenging saturation.

Taggart (2019) found that paleo residual gas is mainly encountered in fields facing various degrees of overpressure, as this can be an indication for structural movement, e.g. burial or tilting, compare also with 2.1.2.

Woods, et al. (2012) identified paleo residual gas by inspecting density logs, neutron logs and resistivity plots. He compared the separation for residual gas as around 6 to 12 pu in clean sandstone, whereas in comparison fully water saturated cores would have only around 3 to 6 pu. While present gas saturations lead to overestimation of formation porosity by neutron logs and cause higher separation in the density-neutron crossover, resistivity logs are not affected and produce valid porosity estimates. Accordingly, the authors named a noticeable effect of anti-correlation between density and resistivity plot in the residual gas zone.

Additionally, Woods, et al. (2012) introduced methods to identify residual gas zones by examine the pressure behavior:

To prove water as the continuous phase, formation pressure gradients need to align with the present water properties. These gradients can be achieved e.g. by performing well tests.

Not only relative pressures provide insight in the continuous phase, also pressure build-up analysis can be informative. When performing a proper pressure build-up analysis, the total compressibility of the system gives insight whether gas is present or not. When the rock properties are known through core analysis, increased total compressibility while matching the build-up allows to estimate near wellbore gas saturation (Woods et al., 2012).

Woods, et al. (2012) described the application of Pickett plots to identify residual gas zones. In Pickett plots, resistivity measurements are plotted against porosity measurement on a double logarithmic plot. A straight line with negative slope plots on the Pickett plot when water saturation is constant. With the assumption of a fully water-saturated sandstone, the water resistivity can be computed from this line. Due to neglecting the presence of hydrocarbons in a residual gas zone, the application of the Pickett plot will lead to an overestimation of water resistivity. The presence of the hydrocarbons in the fluid column cause a higher than actual water resistivity which indicates lower than actual formation water salinities. Hence the inferred salinity from Pickett plots do not align with recovered samples or regional salinities trends, this is a strong evidence for residual gas (Woods et al., 2012).

The Nuclear Magnetic Resonance (NMR) tool responds to protons, i. e. formation hydrogen, in the pore space. Hence the resonance is related to hydrocarbon index.

After logging, a distribution of T2 decay amplitudes versus time at each sample depth is presented and processed to give the total porosity within different ranges of T2. Gas presence reduces the NMR porosity. Accordingly, a deviation between NMR total porosity and density is a strong indicator of gas saturations (Woods et al., 2012).

In view of all that has been mentioned in this sub-sub-chapter, one may suppose only a thorough combination of tools and data sources enables to prove residual gas columns.

### 2.2.2 *Quantification*

Since paleo residual gas can contribute substantially to the field's recovery, it is necessary to quantify residual volumes in place. There is a large number of published studies that present several possibilities on how to access the residual gas volumetrically, namely using log or core analysis.

Surveys such as that conducted by Woods, et al. (2012) have shown that residual gas saturations can be quantified using log analysis and applying e. g. Archie's model. An uncertainty of around 10 percent is asserted to this method. However, the same method is more reliably applicable if water-based mud was used. In that case, the near wellbore saturation ( $S_{xo}$ ) equals the water saturation in the unflushed zone.  $S_{xo}$  is determined with Archie's model by usage of near wellbore resistivity  $R_{xo}$  and mud filtrate resistivity  $R_{mf}$ .

Mulyadi (2002) has listed methods to measure residual gas saturations in core experiments: spontaneous imbibition and forced displacement methods. In her study, Mulyadi (2002) identifies advantages and disadvantages with each technique and determines the forced displacement to be the most representative test. It can provide both endpoints and relative permeability data at ambient and reservoir conditions for imbibition and drainage.

Mulyadi's (2002) summary of the measurement methods is complemented by Woods, et al. (2012), who have assessed the uncertainty associated with each method. To determine the effect of permeability, various permeability ranges have been applied. The lowest  $S_{gr}$  values have been created by the centrifuge method, whereas the counter-current imbibition provides the highest  $S_{gr}$  values. Furthermore, the co-current imbibition generates  $S_{gr}$  values in between these extremes.

Kumar, et al. (2010) highlight the opportunity of using digital core analysis not only to image the fluid distributions in the core but also to test different recovery mechanisms and quantify their impact on the residual fluids.

**2.3 Drainage and Imbibition: Paleo Residual Gas (Re)Mobilization**

Next to quantification of the net residual volumes in place, one must investigate how much of this volume can be remobilized under which conditions. On micro-scale, i.e. pore level, the relative permeability curves follow the different processes of the hysteresis cycle as illustrated in Figure 2.3-1. The four steps, i. e. initial conditions, primary drainage, imbibition and secondary drainage, are described in detail in the following sub-sub-chapters 2.3.1 to 2.3.3.

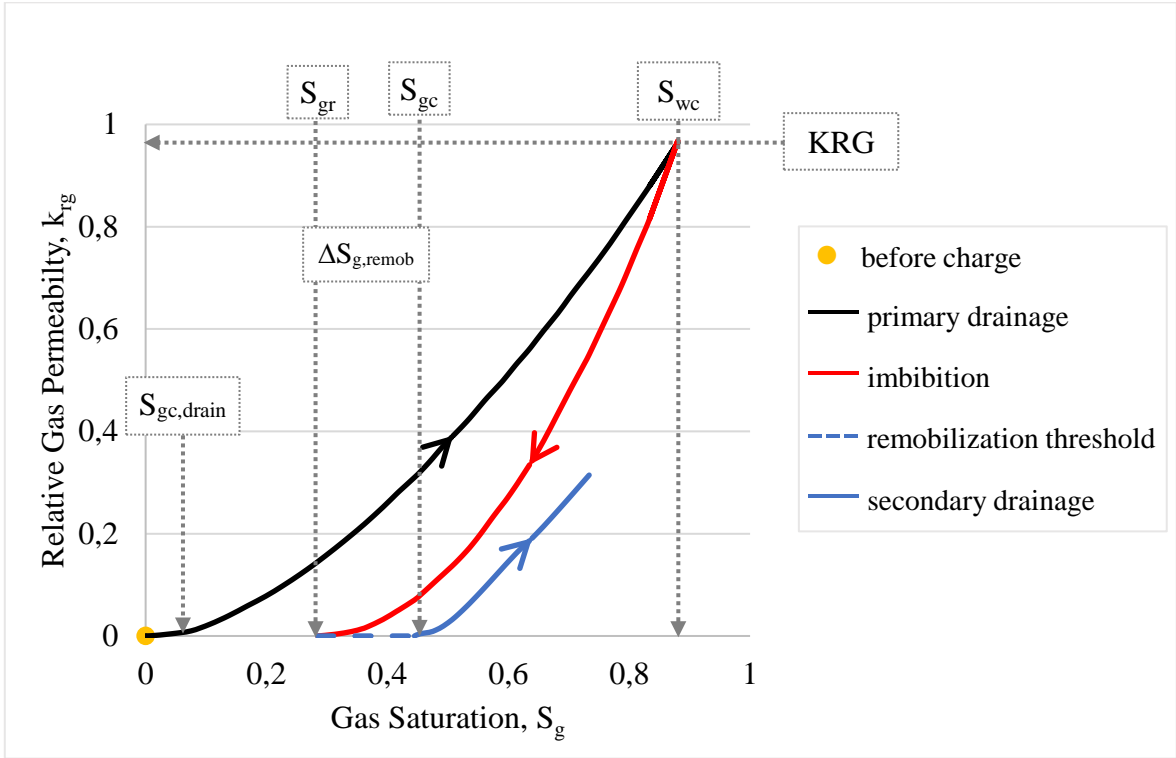


Figure 2.3-1: Hysteresis cycle before charge to primary drainage to imbibition over remobilization threshold to secondary drainage, saturation intervals indicated with dotted arrows, modified after Babadimas (2017).

### 2.3.1 Before Charge to Primary Drainage

Before hydrocarbon charge, the reservoir is fully water saturated. The complete reservoir contains only water. Hydrocarbon charge has not occurred yet (Babadimas, 2017).

Hence,

$$S_g(t = 0) = 1 - S_w = 0 \quad (2.3-1)$$

Given equation (2.3-1),

$$k_{rg}(t = 0) = 0 \quad (2.3-2)$$

follows naturally, refer also to Figure 2.3-1.

Water-gas systems in sandstones are commonly known as water-wet, hence the wetting fluid in the system is water. As the charge begins, gas is migrating out of the source rock into the reservoir rock. The displacement of a wetting fluid (here: water) by a non-wetting fluid (here: gas) is referred to as drainage. Obviously, this process involves the decrease in the saturation of the wetting phase. The specific process here is called primary drainage. Primary drainage describes the first change in equilibrated conditions when gas is entering the pore space and draining out the water initially in place (Babadimas, 2017).

During this step, different characteristic saturation points are reached: First of all, a critical drainage gas saturation  $S_{gc,drain}$  has to be reached, such that the gas is mobile to penetrate the reservoir. Moreover, the system will stabilize at the historical maximum gas saturation  $S_{g,max}$  or connate water saturation  $S_{wc}$  respectively (Babadimas, 2017) as described in (2.3-3), refer also to Figure 2.3-1.

$$S_{wc} = 1 - S_{g,max} \quad (2.3-3)$$

In the present thesis, primary drainage processes are linked to gas charge processes. To describe gas saturation after hydrocarbon charge, drainage  $P_c$  curves are applied during initialization.

### 2.3.2 Imbibition

The displacement of a non-wetting fluid by a wetting fluid is referred to as imbibition. The term is commonly used to describe an increase in the wetting-phase saturation. The wetting phase saturation increases due to water encroachment caused by e.g. aquifer inflow.

During the displacement of one immiscible fluid by another, a saturation of zero of the displaced fluid cannot be obtained. The flow of the displaced gas phase will terminate at the saturation at which it becomes discontinuous. This saturation is defined as residual gas saturation  $S_{gr}$  (Adams, 2003).

The residual gas saturation  $S_{gr}$  is established as gas trapped behind the encroaching waterfront in the continuous water phase (Babadimas, 2017), compare with 2.1.1 and refer also to Figure 2.3-1. How much gas will be trapped in the water phase, can be assessed by different trapping models, which are described in sub-chapter 2.5.

Imbibition curves are used to model gas withdrawal starting from continuous gas phases, i. e. the gas saturation is above its critical saturation. In case of post-charge water influx, imbibition  $P_c$  curves are used for initializing models. In the presence of residual gas saturations, saturation-height functions should be governed by the application of imbibition  $P_c$  curves instead of drainage  $P_c$  curves (Adams, 2003). Endpoints determine the initial saturation distribution during initialization (Kleppe & Andersen, 2019).

### 2.3.3 Secondary Drainage

Under changing of the present conditions, during e.g. pressure depletion, the disconnected bubble clusters expand and reconnect in the water phase to remobilize (Babadimas, 2017). To reconnect the discontinuous gas phase and re-enable flow of the displaced fluid, a certain minimum saturation must be reached. This saturation is referred to as critical gas saturation  $S_{gc}$ . Residual and critical saturations of a fluid are not equal, since residual saturation is measured in the direction of decreasing saturation, whereas critical saturation is measured in the direction of growing saturation (Ahmed, 2006).

A saturation threshold before remobilization is the reason why during secondary drainage the application of the primary drainage gives incorrect results (Babadimas, 2017). The difference between  $S_{gc}$  and the  $S_{gr}$  is denoted as remobilization threshold  $\Delta S_{g,remob}$  and can be calculated as

$$\Delta S_{g,remob} = S_{gc} - S_{gr} \quad (2.3-4)$$

With overcoming the saturation threshold and reaching the critical gas saturation, the gas becomes mobile again and starts into secondary drainage. The wetting phase saturation decreases with ongoing secondary drainage, refer to Figure 2.3-1.

The secondary drainage process refers generally to the decrease from an – usually high – water saturation in the presence of immobile gas saturation and are associated to gas expansion by pressure depletion and remobilization within the scope of the thesis.

This is necessary to mention, since the cause for the gas saturation increase influences the remobilization behavior of the gas phase considerably. The remobilization threshold is neglectable when gas injection causes the saturation increase. The residual gas saturations become mobile immediately (Babadimas, 2017; Fishlock et al., 1988).

## 2.4 Reservoir Engineering Fundamentals

### 2.4.1 Mobility Ratio

The mobility ratio  $M$  of two fluids is the quotient of the relative mobility  $\lambda_{rj}$  of each phase (quotient of relative permeability  $k_{rj}$  and viscosity  $\mu_j$ ) (Lake, et al., 2014).

$$M = \frac{\lambda_{r,1}}{\lambda_{r,2}} = \frac{k_{r1}}{\mu_1} \frac{\mu_2}{k_{r2}} \quad (2.4-1)$$

### 2.4.2 Wettability

The concept of wettability is fundamental for the most important mechanisms of immiscible displacement, i.e. drainage and imbibition. Wettability is the adherence preference of a rock towards a fluid as a measure of the contact angle  $\Theta$  and generally classified into three types: water-wet, oil-wet and mixed-wet. For the purpose of the present thesis the focus is set on water-wet systems, since water-gas systems in sandstones are primarily classified as water-wet (Dake, 1983).

Figure 2.4-1 illustrates a non-wetting and a wetting fluid in contact with a rock surface. The contact angle  $\Theta$  is the angle measured through water and is less than  $90^\circ$  in case of a water-wet reservoir rock. (Dake, 1983).

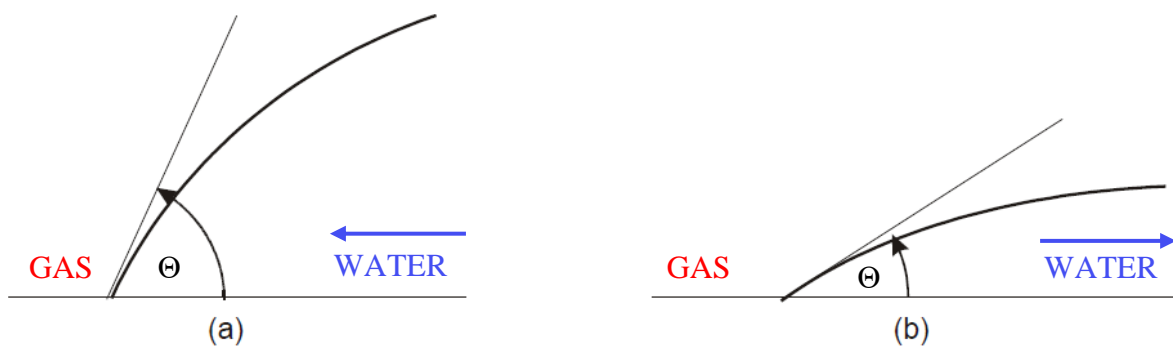


Figure 2.4-1: Contact angle hysteresis in water-wet reservoir: (a) imbibition; (b) drainage, modified after Dake (1983).

Dake describes an increased contact angle when the wetting phase is advancing over the rock face than when retreating. Figure 2.4-1 demonstrates this difference in contact angle, which is a hysteresis effect between the processes of drainage and imbibition (Dake, 1983).

### 2.4.3 Capillary Pressure

Capillary pressure  $P_c$  is known as the pressure difference between a fluid interface, where the pressure on the concave side exceeds the pressure on the convex side. Capillary pressures are essential for fluid in place initialization and will determine the saturation distributions in the transition zone. The computation of the capillary pressure is provided by the Laplace equation (2.4-2) (Dake, 1983).

$$P_{cgw}(S_w) = p_g - p_w = \sigma \left( \frac{1}{r_1} + \frac{1}{r_2} \right) \quad (2.4-2)$$

where:

$P_c$ : capillary pressure

$\sigma$ : interfacial tension

$r_1, r_2$ : principal radii of curvature at any point on the interface

The radii  $r_1$  and  $r_2$  expressed in equation (2.4-2) are visualized in Figure 2.4-2. The figure demonstrates an increasing  $S_w$  with increasing radius. Considering equation (2.4-2), this relation indicates an inverse relation between  $S_w$  and  $P_c$  (Dake, 1983).

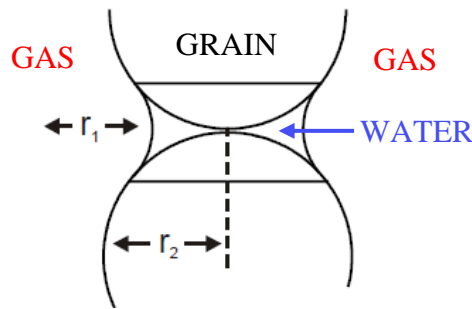


Figure 2.4-2: Water entrapment in water-wet reservoir between grains: increasing  $S_w$  with increasing radius, modified after Dake (1983).

This inverse relationship is called capillary pressure curve and visualized in Figure 2.4-3. The difference in the imbibition and the drainage plot is related to the contact angle hysteresis as described in the previous sub-sub-chapter 2.4.2.  $S_{wc}$  denotes the connate water saturation,  $S_{gr}$  the residual gas saturation. This saturation cannot be reduced further, regardless of the imposed capillary pressure (Dake, 1983).

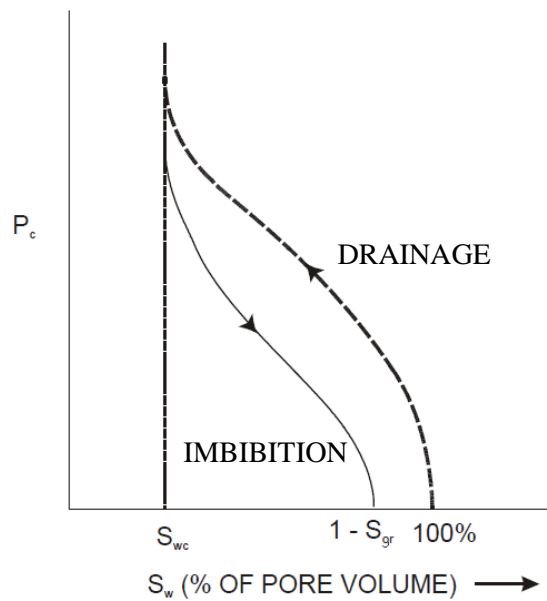


Figure 2.4-3: Capillary pressure function, modified after Dake (1983).

At the free water level, the phase pressure of gas and water are equal. Considering equation (2.4-2) the capillary pressure becomes zero. In a water-wet system, this leads to having a GWC above the FWL under primary drainage conditions and below FWL under imbibition conditions. Let  $\gamma_{g,w}$  denote fluid specific gravities and  $p_{GWC}$  denote the reference pressure in the GWC. Assuming a constant equilibrium state, gas (water) potential  $\psi$  become (Kleppe & Andersen, 2019)

gas: (2.4-3)

$$\psi_g = p_g - \gamma_g d$$

water:

$$\psi_w = p_w - \gamma_w d$$



The fluid phase pressure above and below GWC in block j can be computed as

*gas:* (2.4-4)

$$p_{jg} = p_{GWC} - \gamma_g (d_{GWC} - d_j)$$

*water:*

$$p_{jw} = p_{GWC} - \gamma_w (d_{GWC} - d_j)$$

As shown in equation (2.4-2), the hydrostatic pressure difference is in equilibrium with the capillary pressure, which will finally determine the saturation (Kleppe & Andersen, 2019).

The Skjaeveland correlation for strongly water-wet systems is applied during the thesis. The authors based the general capillary pressure correlation on the simple power-law form of Brooks and Corey and re-wrote the classical expression for a water-wet core, see equation (2.4-5).  $C_w$  denotes the entry pressure, and  $1/a_w$  the pore size distribution index (Skjaeveland, et al., 1998). These parameters will differ between drainage and imbibition processes.

$$P_c = \frac{C_w}{\left(\frac{S_w - S_{wr}}{1 - S_{wr}}\right)^{a_w}} \quad (2.4-5)$$

Using Leverett J-function provides a widely used scaling technique for capillary pressures. Non-uniform permeability or porosity distributions are disregarded when using only capillary pressures and cause an incorrect uniform fluid distribution. Leverett J-functions are used to correlate capillary pressures to these rock properties. J-function J is related to capillary pressure  $P_c$  as follows

$$P_c(S) = J(S) \sigma \left(\frac{\phi}{k}\right)^{1/2} \quad (2.4-6)$$

where k is horizontal permeability (default ECLIPSE),  $\phi$  is porosity and  $\sigma$  is the gas-water surface tension (Kleppe & Andersen, 2019).

#### 2.4.4 Relative Permeability

Any time during two-phase flow, the relative permeability of each phase as a function of a saturation is the ratio of effective permeability over the absolute permeability (Ahmed, 2006), see equation (2.4-7).

$$k_{rl} = \frac{k_l}{k} \quad (2.4-7)$$

In the present thesis, modified Brooks-Corey correlations are used to compute relative permeability curves. The relative permeabilities are computed depending on the maximum relative permeability (KRW, KRG), the critical saturations of gas and water and the Corey exponents for water and gas,  $N_w$  and  $N_g$  respectively, see equation (2.4-8) and (2.4-9) (PetroWiki, 2020a).

$$k_{rw} = KRW * \left( \frac{S_w - S_{wc}}{1 - S_{wc} - S_{gc}} \right)^{N_w} \quad (2.4-8)$$

$$k_{rg} = KRG * \left( \frac{S_g - S_{gc}}{1 - S_{wc} - S_{gc}} \right)^{N_g} \quad (2.4-9)$$

Endpoint relative permeability scaling is used to compensate for non-uniform relative permeability distributions. Saturation tables are provided for specified saturation regions. Endpoint scaling can affect the shape of the relative permeability functions, their mobile saturation intervals and can shift the function by a multiplication factor. Endpoints determine the initial saturation distribution during initialization (Kleppe & Andersen, 2019).

The wetting characteristics of the two phases cause a specific phase distribution in the pore spaces. This leads to specific wetting and non-wetting phase relative permeabilities. In the same manner as for capillary pressure, the hysteresis of the wetting angle causes different measures of relative permeability. This results in different drainage and imbibition relative permeability curves, which has already been introduced and discussed in detail in sub-chapter 2.3. The mobility of the non-wetting phase during imbibition is lower than during drainage at the same water saturation. This mobility loss appears inverse for the wetting phase: the mobility of the wetting phase increases during imbibition and decreases during drainage (Ahmed, 2006).

#### 2.4.5 Black-Oil Model

There are six main assumptions made for a Black-Oil model (Kleppe & Andersen, 2019):

- Three phases: water, oil, gas
- Three components: water, oil gas
- The water component exists in water phase only
- The oil component exists in oil phase only
- The gas component exists in both oil and gas phase. i.e. the oil phase consists of the oil component and part of the gas component
- Constant temperature

The Black-Oil mass balance equations (MBE) for a dry gas case are presented in (2.4-10). Since the oil phase can be neglected in dry gas runs, the relevant Black-Oil model assumptions reduce to:

- Two phases: water, gas
- Two components: water, gas
- The water component exists in water phase only
- The gas component exists in gas phase only
- Constant temperature

Water:

$$\nabla * \left[ \frac{[k]k_{rw}}{\mu_w B_w} (\nabla p_w - g \rho_w \nabla d) \right] + Q_w = \frac{\partial}{\partial t} \left( \phi \frac{S_w}{B_w} \right) \quad (2.4-10)$$

Gas:

$$\nabla * \left[ \frac{[k]k_{rg}}{\mu_g B_g} (\nabla p_g - g \rho_g \nabla d) \right] + Q_g = \frac{\partial}{\partial t} \left( \phi \frac{S_g}{g} \right)$$

The following terms are used in the MBEs:

Formation volume factor B, saturation S and the vertical distance d for a reference level. The source term Q becomes positive in case of injection or aquifer influx and negative in terms of production. The gas formation volume factor B<sub>g</sub> is affected by the gas compressibility and defined as

$$B_g = \frac{V_{RC}}{V_{SC}} = \frac{z_{RC} T_{RC} p_{SC}}{z_{SC} T_{SC} p_{RC}} \quad (2.4-11)$$

where V denotes volume, T denotes temperature, z denotes gas compressibility factor and indices RC (SC) denotes reservoir conditions (standard conditions) (Lee & Wattenbarger, 1996).

#### 2.4.6 Darcy's Law

With k as absolute permeability of the system and μ the viscosity, the Darcy velocity v can be defined with using the pressure gradient  $-\frac{\partial p}{\partial x}$ . The relation shown in equation (2.4-12) is called *Darcy's Law*.

$$v = -\frac{k}{\mu} \frac{\partial p}{\partial x} \quad (2.4-12)$$

Gravity forces can contribute to the flow in case there is an angle between the vertical axis and the flow direction. With  $\vec{g} = (g_x, g_y, g_z)$  as gravitational acceleration and ρ as fluid density, the three-dimensional flow equation of Darcy's law becomes:

$$\begin{aligned} v_x &= -\frac{k_x}{\mu} \left( \frac{\partial p}{\partial x} - \rho g_x \right) \\ v_y &= -\frac{k_y}{\mu} \left( \frac{\partial p}{\partial y} - \rho g_y \right) \\ v_z &= -\frac{k_z}{\mu} \left( \frac{\partial p}{\partial z} - \rho g_z \right) \end{aligned} \quad (2.4-13)$$

The equations in (2.4-13) can be simplified assuming one-dimensional flow in z-direction and when the z-axis is parallel to the vertical direction (x- and y-axis form the horizontal plane). In this case, g becomes the absolute value of the gravity acceleration:

$$v_z = -\frac{k_z}{\mu} \left( \frac{\partial p}{\partial z} - \rho g \right) \quad (2.4-14)$$

The transport equations for gas (g) and water (w) in porous media are given by

*Water:* (2.4-15)

$$\frac{\partial}{\partial t} (\rho_w \varphi S_w) = -\frac{\partial}{\partial z} (\rho_w v_w)$$

*Gas:*

$$\frac{\partial}{\partial t} (\rho_g \varphi S_g) = -\frac{\partial}{\partial z} (\rho_g v_g)$$

Considering two-phase flow, Darcy's flow equation for water and gas restructures to equation (2.4-16). Only vertical flow is present, yet this flow is affected by gravitational forces.

*water:* (2.4-16)

$$v_w = -\frac{kk_{rw}}{\mu_w} \left( \frac{\partial}{\partial z} p_w - \rho_w g \right)$$

*gas:*

$$v_g = -\frac{kk_{rg}}{\mu_g} \left( \frac{\partial}{\partial z} p_g - \rho_g g \right)$$

Volume conservation constraints the saturation parameters.

$$S_w + S_g = 1 \quad (2.4-17)$$

Through the capillary pressure formulation (equation (2.4-2)) the pressure parameters are constraint under the assumption of phase pressure equilibrium.

$$P_c = p_g - p_w \quad (2.4-18)$$

#### 2.4.7 Fetkovich Aquifer Model

In sub-sub-chapter 2.1.2 the important influence of aquifer influx on paleo residual saturations and the fluid-fill status of the field has been discussed. For this reason, it is crucial for a reliable analysis to choose an aquifer model which reproduces the aquifer behavior of the field best.

For this study, the Fetkovich (1971) aquifer model was chosen. The advantages of the Fetkovich model is not only that it is simple to understand. The approach has a number of attractive features: When varying the different parameter the aquifer performance depends on, a wide range of aquifer behaviors can be modeled.

The Fetkovich aquifer model is described by a simplified approach based on a material balance relationship and a pseudo steady-state productivity index between the cumulative influx and the aquifer pressure. Under the assumption of uniform reservoir pressure in the connecting grid blocks, the average influx rate  $\overline{Q_{ai}}$  from aquifer to connecting grid block i over the time interval  $\Delta t$  becomes (Schlumberger, 2016):

$$\overline{Q_{ai}} = a_i J (p_a - p_i + \rho g(d_i - d_a)) \left( \frac{1 - e^{(-\Delta t/T_c)}}{\Delta t/T_c} \right) \quad (2.4-19)$$

with parameters

$a_i$  – area fraction for connection to grid block  $i$ ,

$J$  – productivity index

$p_a$  – pressure in aquifer at time  $t$ ,

$p_i$  – water pressure in connecting grid block  $i$ ,

$\rho$  – water density in the aquifer,

$d_i$  – depth of grid block  $i$  and

$d_a$  – datum depth of the aquifer.

The aquifer time constant  $T_c$  is defined as

$$T_c = \frac{c_t V_{w0}}{J} \quad (2.4-20)$$

and consists of the total compressibility of the aquifer  $c_t$ , the initial water volume of the aquifer  $V_{w0}$  and the productivity index  $J$  (Schlumberger, 2016).

The range of aquifer behavior that the Fetkovich model can mimic, may be summarized with the following two extreme cases. If the product of total compressibility and initial water volume of the aquifer becomes large, consequently the aquifer time constant becomes large. The aquifer will then approach a steady-state aquifer where the pressure on the external boundary will not change with time. The opposite case, a relatively small aquifer time constant, can be achieved by choosing a large productivity index. Then the aquifer approaches a ‘pot’ aquifer behavior, which has closed boundary conditions. The pressure in the aquifer will then be in relative equilibrium with the reservoir throughout all time steps (Schlumberger, 2016).

## 2.5 Gas Trapping Models

### 2.5.1 Land

Land (1968) has introduced a widely applied trapping model. Land’s trapping model is based on published data of water-wet sandstone cores and gives a correlation between the residual gas saturation after water inflow and the initial gas saturation  $S_{gi}$ , see equation (2.5-1). He found, that the residual gas saturation  $S_{gr}$  increases with increasing initial gas saturation  $S_{gi}$ .

$$S_{gr} = \frac{S_{gi,max}}{1 + C S_{gi,max}} \quad (2.5-1)$$

The constant  $C$ , Land’s trapping constant, is shown in equation (2.5-2), where maximum residual gas saturation related to the imbibition curve is  $S_{gr,max}$  and the maximum gas saturation (historically) is  $S_{gi,max}$ .

$$C = \frac{1}{S_{gr,max}} - \frac{1}{S_{gi,max}} \quad (2.5-2)$$

Land is also providing an expression to obtain the remainder of the mobile gas saturation (flowing gas saturation  $S_{gf}$ ) after  $S_g$  has been reduced from  $S_{gi}$  to  $S_g$ :

$$S_{gf} = \frac{1}{2} * \left[ (S_g - S_{gr}) + \sqrt{(S_g - S_{gr})^2 - \frac{4}{C} (S_g - S_{gr})} \right] \quad (2.5-3)$$

### 2.5.2 Jerauld

Jerauld (1997) modified Land's trapping model using a zero-slope generalization to better match the trends he has observed (lower residual gas saturations in samples with higher microporosity).

$$S_{gr} = \frac{S_{gi}}{1 + \left( \frac{1}{S_{gr}^{max}} - 1 \right) * (S_{gi})^{\left( \frac{1}{1 - S_{gr}^{max}} \right)}} \quad (2.5-4)$$

### 2.5.3 Mulyadi

Mulyadi (2002) provides a trapping correlation based on steady-state displacement tests. Mulyadi's trapping correlation is shown in equation (2.5-5). Unlike Land's model, Mulyadi's model has a parabolic shape as a function of  $S_{gi}$ .

$$S_{gr} = -7,4828 * S_{gi}^2 + 12,21 * S_{gi} - 4,7343 \quad (2.5-5)$$

The correlation was build based on four core samples with a vast variation in rock properties, e.g. permeability variations from 0,1 mD to 3515 mD.

### 2.5.4 Parameters Influencing the Trapped Gas Saturation

Diagram 2.5-1 shows the effect of the rock type on the shape of the initial residual gas phase saturation curves. The residual gas saturation decreases with decreasing shale volume (cleanness), decreasing cementation (higher porosity  $\Phi$ ) and increasing sorting and grain size. Conversely, Hamon et al. (2001) reported no significant relationship between cementation factor and trapped gas saturation. Similarly, Jerauld (1997) found that lower porosity and poorer sorting lead to increase trapped gas levels.

The type of clay does not influence the amount of  $S_{gr}$ , but increasing clay amounts cause decreasing trapped gas saturation (Hamon, et al., 2001). This aligns with the observations of Jerauld (1997) where lower residual gas saturations appears in samples with higher microporosity, which also suggests microporosity is not gas trapping.

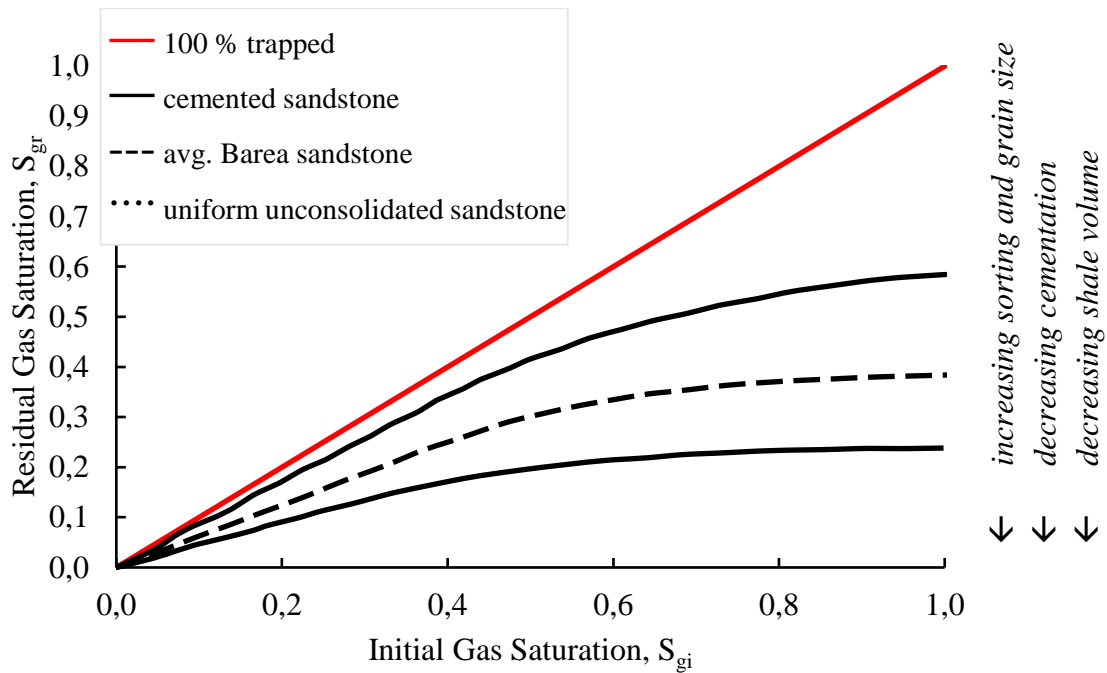


Diagram 2.5-1: Typical initial residual non-wetting-phase (gas) saturations curves, after Lake et al. (2014) and Holtz (2002).

Mulyadi (2002) provided correlations based on steady-state displacement tests. The clearest (parabolic) correlation was found between  $S_{gr}$  and water permeability  $k_w$ . The weakest correlation was found between  $S_{gr}$  and porosity (linear increasing). Other correlations occurred between  $S_{gr}$  and air permeability (linear decreasing) as well as  $S_{gr}$  and initial water saturation  $S_{wi}$  (parabolic).

Hamon et al. (2001) argues for three major trends of  $S_{gr}$  versus porosity depending on the porosity magnitude itself. In low and medium porosity range (i.e. less than 14 percent), whereas for most sandstones  $S_{gr}$  increases with porosity increases, Fontainebleau sandstones show decreasing  $S_{gr}$ . In high porosity range (i.e. more than 14 percent), the two described trends merge around a  $S_{gr}$  of 25 to 35 percent.

#### 2.5.5 Remark

In Diagram 2.5-2 a comparison of the three previously discussed correlation is presented. Since Jerauld's model is based on Land's model, they show roughly the same shape. Jerauld's model seems to be a representation of Land's model with a Land's trapping constant of 3. Nevertheless, one can clearly see the stronger curvature. The two correlations represent the saturation behavior given in Diagram 2.5-1.

However, Mulyadi's model does not align with the other two correlations nor represent the saturation behavior given in Diagram 2.5-1. A possible explanation is that the strong hyperbolic shape is a result of the small sample size the correlation is built on. Possibly, her findings are not reproducible due to extrapolation over such a wide permeability range.

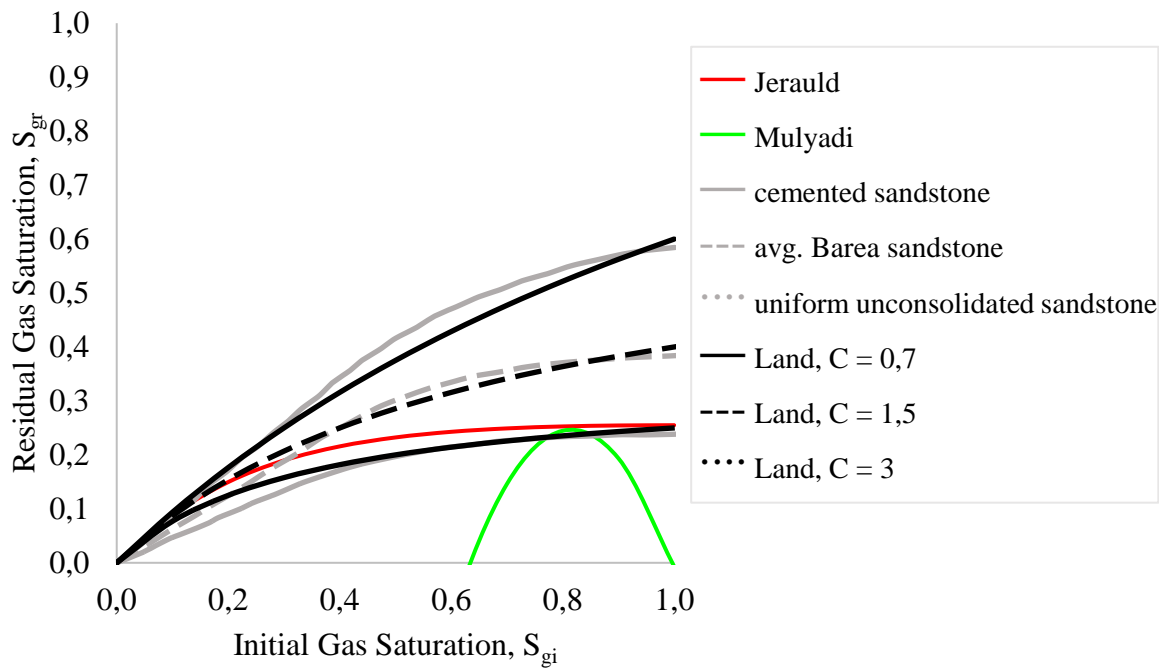


Diagram 2.5-2: Comparison of Land's trapping model equ. (2.5-1) with Jerauld's trapping model equ. (2.5-4) and Mulyadi's trapping model equ. (2.5-5); grey curves of Diagram 2.5-1.

## 2.6 Hysteresis Models

Land's trapping model, see sub-chapter 2.5.1, allows a relation of relative permeability towards saturation and has been so far the foundation for several relative permeability models that cover hysteresis (Killough, 1976). Land (1968) stated, that relative permeability is not only dependent on saturation itself but also on saturation history.

### 2.6.1 Killough

Killough (1976) developed a widely accepted relative permeability hysteresis model. The calculation of the amount of the residual non-wetting phase is based on an adaption of Land's (1968) trapping model. Killough's model is history-dependent and considers the effect of trapped gas on capillary pressures and relative permeabilities.

Experimental data often provides only relative permeability endpoints of the imbibition and drainage curve. In the absence of further experimental data, intermediate values can then be determined by interpolation between these experimental endpoints with this model. In this hysteresis model relative permeabilities can vary between imbibition and drainage curves by applying so called 'scanning' curves (illustrated as black dashed line in Figure 2.6-1).



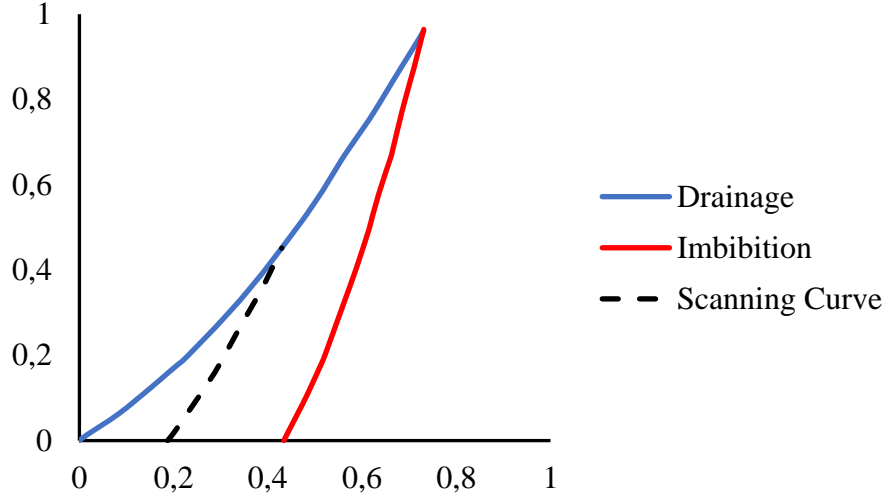


Figure 2.6-1: Non-wetting phase hysteretic relative permeability characteristics, including scanning curve (dashed black) modified after Killough (1976).

Equation (2.6-1) shows the computation of the gas relative permeability with respect to a specific gas saturation on a scanning curve.

$$k_{rg}^{imb}(S_g) = \frac{k_{rg}^{imb}(S_{g,norm}) * k_{rg}^{drain}(S_{gi})}{k_{rg}^{drain}(S_{gi,max})} \quad (2.6-1)$$

The hereby applied normalized saturation  $S_{g,norm}$  is given in equation (2.6-2).

$$S_{g,norm} = S_g + \frac{(S_g - S_{gr,max}) * (S_{gr,max} - S_g)}{(S_{gi} - S_{gr,max})} \quad (2.6-2)$$

### 2.6.2 Carlson

Carlson (1981) has introduced a relative permeability hysteresis model with a simple geometrical interpretation: He found that any scanning curve can be shifted parallel to a given imbibition curve. Carlson's model is as well based on Land's trapping model (i. e. equation (2.5-2)). All necessary input parameters are the drainage curve in combination with  $S_{gi,max}$  and a minimum saturation of another point from the correspondent imbibition curve together with equation (2.5-1).

### 2.6.3 Hustad's ODD3P hysteresis model

Hustad & Browning (2009) developed a coupled three-phase model for capillary pressure and relative permeability, also known as ODD3P method (abbr. for Odd Hustad's three phase method) based on an earlier publication from Hustad (2002). The method was developed to study the process of pressure depletion after waterflooding (or water encroachment) and is able to reproduce secondary drainage flow behavior. Input data (i.e.  $k_r$  and  $P_c$  values) must be history dependent. The direction of the phase saturation hereby determines the hysteresis process, see Table 2.6-1, which gives the primary, secondary and the tertiary hysteresis function. These replace the well-established termination of drainage and imbibition functions.

Table 2.6-1: ODD3P hysteresis cycles (Babadimas, 2017; Hustad & Browning, 2009).

<b>Hysteresis</b>	<b>Water Saturation</b>	<b>Gas Saturation</b>
Primary	Decreasing	Increasing
Secondary	Increasing	Decreasing
Tertiary	Decreasing	Increasing

The different hysteresis functions are assigned as follows: The primary hysteresis will be applied for the time interval of the reservoir after initial conditions, when hydrocarbon-charge takes place and causes the water saturation to decrease. At the time the primary saturation function is not retraced anymore, a hysteresis loop is entered. During decrease and increase of the fluid saturations, the hysteresis behavior is modeled by applying two sets of hysteresis saturation functions (Babadimas, 2017).

Under the assumption in equation (2.6-3) and by combining two-phase  $k_r$ , three-phase  $k_r$  are calculated, see equation (2.6-4) for the general expression.

$$\begin{aligned} i, j, k &= \text{oil, gas, water} \\ i &\neq j \neq k \end{aligned} \quad (2.6-3)$$

$$k_{ri} = \frac{S_j}{S_j + S_k} * k_{rij} + \frac{S_k}{S_k + S_j} * k_{rik} \quad (2.6-4)$$

Accordingly, the gas relative permeability is calculated in equation (2.6-5). This expression simplifies drastically, in a two-phase system of gas and water only: The  $k_{rg}$  is then simplified to the relative permeability to gas in a gas-water system (2.6-6) (Babadimas, 2017).

$$k_{rg} = \frac{S_o}{S_o + S_w} * k_{rgo} + \frac{S_w}{S_w + S_o} * k_{rgw} \quad (2.6-5)$$

$$k_{rg} = k_{rgw} \quad ; \quad S_o = 0 \quad (2.6-6)$$

Respectively, the water relative permeability is computed in equation (2.6-7). This expression simplifies similarly in a two-phase system of gas and water only: The  $k_{rw}$  is then simplified to the relative permeability to water in a gas-water system (2.6-8) (Babadimas, 2017).

$$k_{rw} = \frac{S_o}{S_o + S_g} * k_{rwo} + \frac{S_g}{S_g + S_o} * k_{rwg} \quad (2.6-7)$$

$$k_{rw} = k_{rwg} \quad ; \quad S_o = 0 \quad (2.6-8)$$

#### 2.6.4 Remark

In sub-chapter 2.3 an important feature of gas remobilization has been introduced: the remobilization threshold. This threshold causes the secondary drainage curve during depletion to be located below the imbibition curve.

Babadimas (2017) claims, that some of the previously discussed relative permeability hysteresis models are not able to display this property: While the models by Killough (1976) and Carlson (1981) are unable to model the correct location of the secondary drainage curve, Hustad & Browning (2009) model is able to implement this characteristic.

That is why Babadimas (2017) concluded that the model of Hustad & Browning (2009) should be preferred over the standard formalisms to correctly assess the recovery of the residual hydrocarbons in place. The model is already implemented in the usual commercial simulators, however just applicable in the compositional mode and not in the Black-Oil model.

## 2.7 Residual Gas Studies

### 2.7.1 Experimental Studies

There is a relatively small body of experimental studies that is concerned with depletion and investigating the remobilization of trapped gas (Cable et al., 2004; Cense et al., 2016; Firoozabadi et al. 1987; Fishlock et al., 1988).

Cense et al., (2016) discussed pitfalls of special core analysis for gas fields and described uncertainties associated to these experiments and how to reduce them.

One challenge has been identified according to the evaluation of the gas in place (GIP). Figure 2.7-1 provides an overview of paleo contact data from logs and calculations. Water saturation values from log data are plotted against water saturation values calculated by a Leverett J-function. The left plot shows the deviation (orange crosses) from the drainage J-function for data observed above the anticipated FWL. Deviation between imbibition and drainage curve is significantly decreased above this depth (right plot).

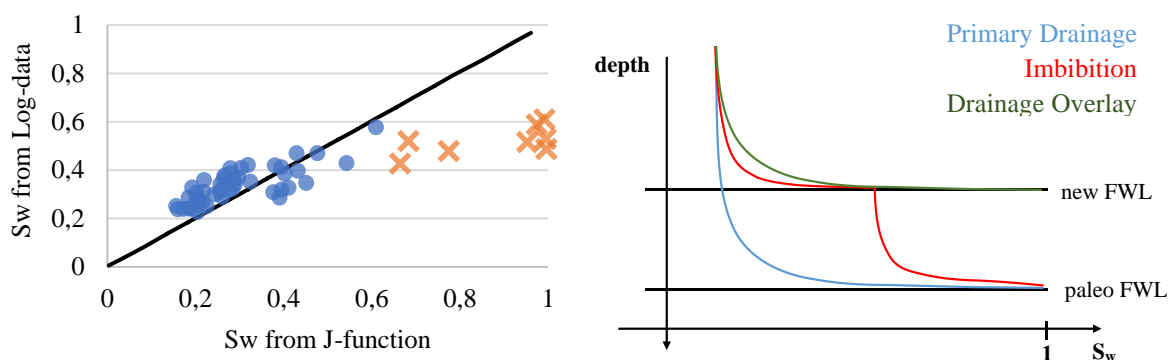


Figure 2.7-1: Paleo contact detected from deviation of saturation behavior in transition zone. Left:  $S_w$  from logs versus  $S_w$  by J-function, fitting values (blue dots) and deviating values (orange crosses). Right: primary drainage (blue), imbibition (red), drainage overlay (green), from Cense et al., (2016).

On the contrary to the example provided here (favorable permeability), this can lead in low permeability reservoirs to a stronger transition zone. Accordingly, the authors concluded, using drainage instead of an imbibition curve in extended reservoirs can have huge effects on recovery prediction.

Cense et al., (2016) further recommend applying low rates for coreflooding to  $S_{gr}$ . This will guarantee a more reliable representation of aquifer encroaching rates. This will also respect fluid equilibration times prior experiments to assure sufficient gas distribution in the core as well as limit differential pressure and injection volumes (2PV) during these flooding. It is not necessary to inject significantly more since the residual gas saturation at breakthrough is considered to represent the reservoir residual gas saturation reliably. The authors also advised to quality-check any measured  $S_{gr}$  with volumetric methods or literature data. The usual  $S_{gr}$  range is hereby 20 to 40 percent. Uncertainties can lead to errors around 3 percent of original GIP.

Cable et al., (2004) conducted a laboratory study with the objective to study the recovery potential of trapped gas using core samples from the target flow zone established in reservoir conditions. Both conducted depletion experiments faced gas remobilization after a saturation increase of 0,3.

Fishlock et al., (1988) performed a laboratory study with the objective to study the remobilization of trapped gas and its saturation in sandstone core samples. The authors found notable differences regarding the event causing the remobilization (depletion versus gas injection). Whilst the depletion  $k_{rw}$  curve of the secondary drainage curve equals the curve obtained by gas injection, differs the depletion  $k_{rg}$  curve significantly from the secondary drainage curve obtained by gas injection.

Firoozabadi et al. (1987) conducted a laboratory study with the objective to measure residual and critical gas saturation in sandstones. The authors concluded,  $S_{gi}$  increases with  $S_{wi}$ . They encountered a  $S_{gr}$  of 30 percent and  $S_{gc}$  of 40 percent respectively. The application of a numerical simulation to history match the depletion test showed stronger sensitivity of the system to variations of  $S_{gr}$  than variations of water relative permeability or capillary pressure curves. They achieved a final match by varying the remobilization threshold and identified postponement of residual gas migration from the water invaded region to the gas zone as an important mechanism to be matched by  $S_{gc}$ .

### 2.7.2 *Simulation Studies*

Babadimas (2017) concluded after a vast literature study, residual gas saturations are not only slowing down the aquifer influx but are also likely to provide pressure support and incremental recovery by gas remobilization. He differs similarly to Fishlock et al., (1988) between the origins of gas saturation increase. Gas injection causes immediate mobilization, gas expansion requires a saturation increase of 2 to 14 percent regarding his literature study. Babadimas advises to use the hysteresis model of Hustad instead of the standard formalisms of Killough and Carlson, see sub-chapter 2.6. Consistent with the findings of Firoozabadi et al. (1987), a

sensitivity of the production behavior towards  $S_{gc}$  was encountered during the simulation study. Gas production will be smaller and water production higher when correctly applying secondary drainage curves.

Undeland's (2012) study had the objective to understand the physics of residual gas during pressure depletion, including the effect on potential incremental volumes and the driving mechanism for residual gas remobilization. Undeland underlined the importance of the charging history of a field to understand the location of residual gas in the reservoir. Residual gas saturations of 0,21 up to 0,41 have been applied in the field study. Regardless the discussion of literature regarding remobilization threshold, she assumed zero remobilization threshold and achieved a residual gas production of 19 percent. The author found, that an introduction of a remobilization threshold of 5 percent would lead to a decrease of residual gas production of only 2 percent.

A broader perspective has been adopted by Taggart (2019), who discussed evidence for paleo residual gas and how to incorporate it into simple reservoir simulation models. In contrast to the previous studies, Taggart argues that modelling of the reservoir charging history is not necessary, as paleo gas can be implemented in the dynamic model without including hysteresis of neither  $k_r$  nor  $P_c$ . The author concludes that paleo column thickness can be set by density differences from PVT and the level of negative capillary pressure. In line with the previous studies, he reports contribution to the field reserves.

Boya Ferrero et al., (2018) conducted full hysteresis simulation studies based on the fluid-fill cycle of a clastic low porosity field to assess its field potential and water risk. The authors described the problem of water loading of wells by cusping through high permeability layers. They concluded, that especially these high permeability layers tend to experience earlier water breakthrough induced by stronger depletion due to a more favorable production environment. They stated, this problem might be mitigated by correct well placement and parallel production from gas and water intervals.

### 2.7.3 Analogues

Babadimas (2017) carried out a vast literature study on residual and paleo residual gas analogues (see Table 2.7-1). The waterflood induced  $S_{gr}$  values gathered are ranging from 0,15 to 0,47. Gas saturation remobilization threshold varies between 0,027 and 0,14.

To investigate correlations between residual gas saturation and critical gas saturation towards permeability, the data from see Table 2.7-1 is plotted in Diagram 2.7-1. It is not possible to identify any trends of  $S_{gr}$  and  $S_{gc}$  being a function of permeability. Observations suggest that there may be a link between permeability and remobilization threshold. There is a vague trend visible, of remobilization threshold increasing with increasing permeability. The small sample size below permeabilities of 1000 mD does not allow for further conclusions.

Table 2.7-1: Analogues: gas saturation threshold for remobilization, modified and extended after Babadimas (2017)

Source	Rock Type	k [mD]	S <sub>gr</sub> [-]	S <sub>gc</sub> [-]	ΔS <sub>g,remob</sub> [-]
Cable et al., (2004)	Reservoir Rocks	3,2	0,47	0,50	0,03
	High Clay	3,2	0,41	0,44	0,03
Egermann et al. (2010)	UGS 1	1200	0,25	0,287	0,037
	UGS 2	1500	0,21	0,254	0,044
	UGS 3	500	0,30	0,334	0,034
	UGS 4	1700	0,25	0,28	0,03
	UGS 5	700	0,15	0,198	0,048
	UGS 6	1000	0,19	0,217	0,027
Firoozabadi et al. (1987)	Core A	1915	0,29	0,377	0,082
	Core B	1445	0,31	0,41	0,099
	Core C	1792	0,28	0,411	0,131
Fishlock et al., (1988)	Sandstone	1280	0,35	0,49	0,14
	Low Clay	240	0,39	0,46	0,07
Undeland (2012)	Case 1	500-1000	0,21	0,26	0,05
	Case 2		0,30	0,35	0,05
	Case 3		0,41	0,46	0,05

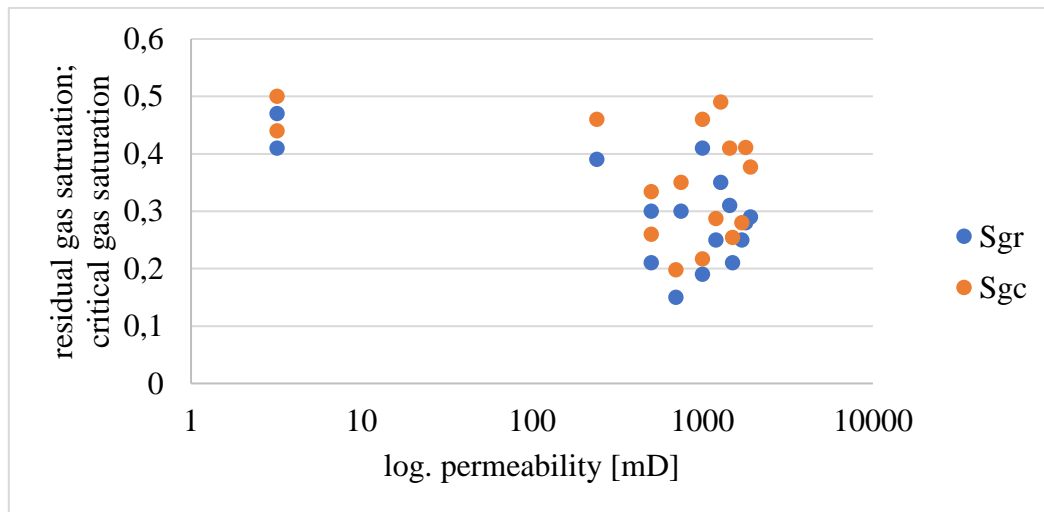


Diagram 2.7-1: No trends visible: residual gas saturation and critical gas saturation versus log. permeability from Table 2.7-1.

### 3 GAS FIELD CASE STUDY

#### 3.1 Overview

The gas impact and recovery potential of paleo residual gas is investigated in a field case. Therefore, an overview of the field is given in this chapter and the relevant properties are discussed. The field is a gas field on the Norwegian Continental Shelf and consists of two separate structures: an East structure and a West structure. The East structure is located in a water depth of 344 m. The West structure is located 3,5 km west of the East structure in a water depth of 400 m.

The following chapter is dedicated to all relevant field-specific details for the assessment, covering its exploration history, the geological, petrophysical key facts as well as reservoir engineering specific parameters and the recent development status.

##### 3.1.1 Exploration History

In 1984, an exploration well (well A) was drilled down-flank by Conoco Norway Inc. into the East structure targeting the Middle Jurassic sands of the Fangst Group, see well location(s) in Figure 3.1-1. A DST carried out in this well produced mainly formation water and minorly gas from upper Garn Fm. and was declared dry (DEA Norge AS, 2016a).

After re-processing a 3D seismic data survey, a discovery well (well B) was drilled 3,7 km southwest of well A in 2010, see Figure 3.1-1. Well B proved commercial volumes in Garn and Ile Fm. in East segment (DEA Norge AS, 2016a). Two years later in 2012, the second discovery well (well C) was drilled, this time in the West segment. Well C added significant commercial hydrocarbons to the license.

The reservoir rocks of both main discoveries consist of Jurassic sandstones of the Garn and Ile Fm., belonging to the Fangst Group (DEA Norge AS, 2016a).

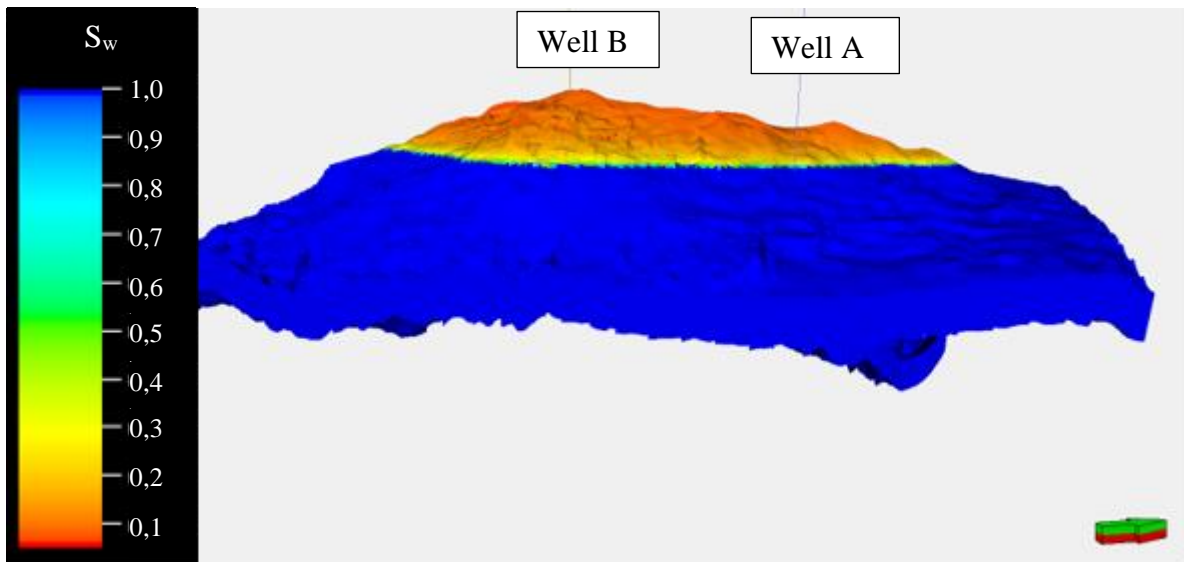


Figure 3.1-1: Well location of wells A and C in the East structure.

### *3.1.2 Static Reservoir Description*

The production license in the central part of the Norwegian Sea. In the Triassic, the geological environment of the Norwegian Sea was a continental plain transferring to a shallow-marine embayment, inundated by marine floodings. As a consequence, repeated progradation of sands occurred into a Jurassic tidally influenced embayment or strait (DEA Norge AS, 2016a).

Garn Fm. and Ile Fm. represent two different lithologies. Whereas the sandstone of Garn Fm. is massive and clean with permeabilities in the range of 1 to 1000 mD, the Ile shows poorer properties. Ile Fm. sandstones are characterized by interlayered silt-sand sequences with minor thin shale layers. They rarely provide permeabilities higher than 1 mD (DEA Norge AS, 2016a). Special in the Garn Fm. are two high permeability layers (upper and lower high permeability layer), whose impact on water impact will be investigated during the study.

The reservoir has been buried to depths of 4100 to 4300 mTVDSS. The burial diagenesis has affected the rocks significantly but showed different impact for the two formations.

Petrographic and fluid inclusion studies of Garn Fm. indicate lower diagenetic reduction in reservoir properties than expected at these depths. The lower diagenetic reduction is caused by the presence of residual heavy oil associated with an early paleo-oil fill of the reservoir, see sub-chapter 3.1.3. The reservoir properties in well A do not have the same diagenetic preservation. Hence, one encounters different diagenetic regimes above and below the current FWL (DEA Norge AS, 2016a).

### *3.1.3 Hydrocarbon Charge*

The importance of the charging history for the formation of paleo gas columns has already been discussed in sub-sub-chapter 2.1.2. Hence, it is necessary to elaborate on the understanding of the hydrocarbon charge itself and the geological processes after hydrocarbon charge. However, the fluid-fill history of the field is not yet clear. Encountered gas saturations below the FWL are a strong indication that the field is currently in an imbibition state.

According to the PDO the source rock of the field is the Spekk Fm. The gas encountered in the present-day accumulation in Garn Fm. (Upper Jurassic) fit to been originated the Spekk Fm (DEA Norge AS, 2016a).

### *3.1.4 Dynamic Reservoir Description*

As described in 3.1.2, the field consists of two isolated structures, containing relatively lean gas. The common datum is at 4242 mTVDSS , the initial reservoir temperature 159 °C and initial reservoir pressure 635 bar and 722 in East and West respectively (DEA Norge AS, 2016a).



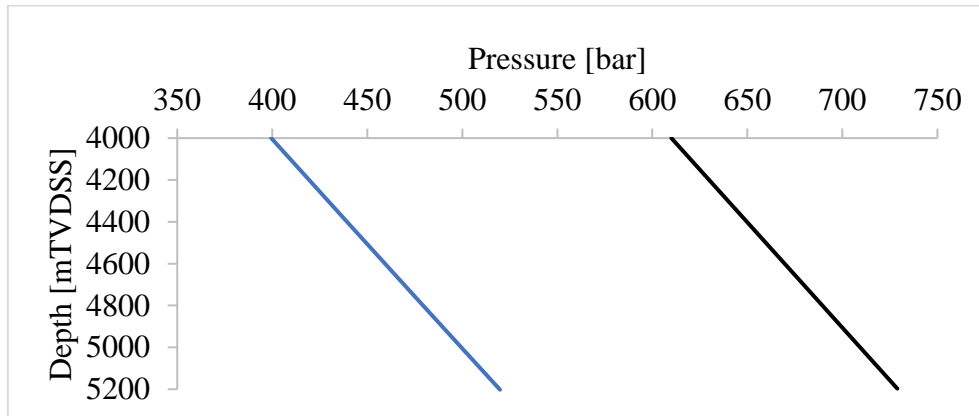


*Diagram 3.1-1: Hydrostatic pressure (blue) and reservoir pressure (black) of the East structure versus depth: visible overpressurization (DEA Norge AS, 2016a).*

While Garn Fm. has good connectivity and excellent flow properties for gas, Not and Ile Fm. show very poor reservoir quality and bear less than 8 percent of the gas initially in place. Furthermore, the earlier mentioned high-permeability layers should contribute to commercial production rates (DEA Norge AS, 2016a).

The main drainage strategy is planned as pressure depletion: two near-vertical production wells on each structure are placed structurally high and distantly from the aquifer. The production is limited to Garn Fm. to avoid potential water inflow. Additionally, gas from Ile and Not Fms. is going to bleed into Garn Fm., where these formations are juxtaposed by faults. Nevertheless, the recovery in Ile and Not Fms. is expected to be low (DEA Norge AS, 2016a).

According to the post-PDO reference case, an average field recovery factor (RF) 71.7 percent is expected after 12,5 years (DEA Norge AS, 2016a).

The production plateau rate will be maintained for 2 years. In sum, 17,95 BSm<sup>3</sup> gas are technically recoverable reserves. In average, a pressure depletion of more than 500 bar is expected, assuming an average abandonment pressure in Garn of circa 120 bar. The field contains rather dry gas condensate. Hence, the associated condensate production is of relatively low importance (DEA Norge AS, 2016a).

### 3.1.5 Aquifer Behavior

The dynamic production performance will be dominated by gas expansion. Minor effects are expected to be contributed by water expansion and pore-volume reduction. And despite some water in the gas leg during pressure depletion, no free water production from the weak aquifer is expected (DEA Norge AS, 2016a). The mobilization of the water in the paleo residual gas leg will be assessed in a conceptual simulation study.

This interpretation of a limited aquifer originates from the following reasoning: The two structures show different degrees of overpressure differing by hundred bars. This deviation is a

strong indicator for a limited aquifer. The aquifer provides small water influx by edge-drive from the east. Furthermore, the aquifer connected to the field has relatively poor flow properties due to diagenetic influences as described in 3.1.2 (DEA Norge AS, 2016a).

### 3.1.6 Gas Composition

The gas consists majorly of methane (89 mole percent) as shown in Table 3.1-1. Therefore, liquid drop-out is anticipated to be limited and immobile.

*Table 3.1-1: Rounded reservoir fluid composition of the East structure (DEA Norge AS, 2016b).*

	<b>Mole</b>
<b>N<sub>2</sub></b>	0,3 %
<b>CO<sub>2</sub></b>	5,4 %
<b>C<sub>1</sub></b>	88,5 %
<b>C<sub>2</sub></b>	3,8 %
<b>C<sub>3</sub></b>	0,9 %
<b>C<sub>4</sub> – C<sub>6</sub></b>	0,5
<b>C<sub>7+</sub></b>	0,6 %

## 3.2 Paleo Residual Gas in the field

Simulations do not contain any assessment of residual gas so far. The models (including the PDO model) assume only free gas saturations. This sub-chapter aims to provide the boundary conditions for a possible volume assessment of residual gas. For this purpose, the charging history of the field and the log readings of well A are evaluated with respect to paleo residual gas evidence.

### 3.2.1 Charging History

The charging history has already been discussed in sub-chapter 3.1.3. There are two possible scenarios which could account for the development of paleo residual gas saturations. One scenario describes the possibility of a leaking seal, the other scenario suggests a spill towards the East. Combining the scenarios with the findings in sub-sub-chapter 2.3.2 about the importance of the charging history for the formation of paleo gas columns, the presence of paleo gas columns is possible.

### 3.2.2 Residual Gas Column

As described in sub-chapter 3.1.1, well A is located down-flank into the East structure. The DST produced mainly formation water and minorly gas from upper Garn Fm.

Sub-sub-chapter 2.2.2 discussed the possibilities to quantify residual volumes. To access the thickness of the residual gas column special attention must be paid to the determination of porosity and water saturation. PetroWiki, 2020, emphasizes the relative importance of water saturation and porosity in calculating the original gas in place (OGIP). Considering a 20 percent bulk volume (BV) porosity reservoir, a change in  $S_w$  of 10 percent pore volume (PV) has the same impact as a change in porosity of 2 percent BV.

The well A is in poor conditions, the caliper log see Figure 3.2-1 shows large deviation, hence large breakouts. The quality of the borehole strongly effects the porosity calculation, nevertheless the calculation results were quality-checked against core porosity.

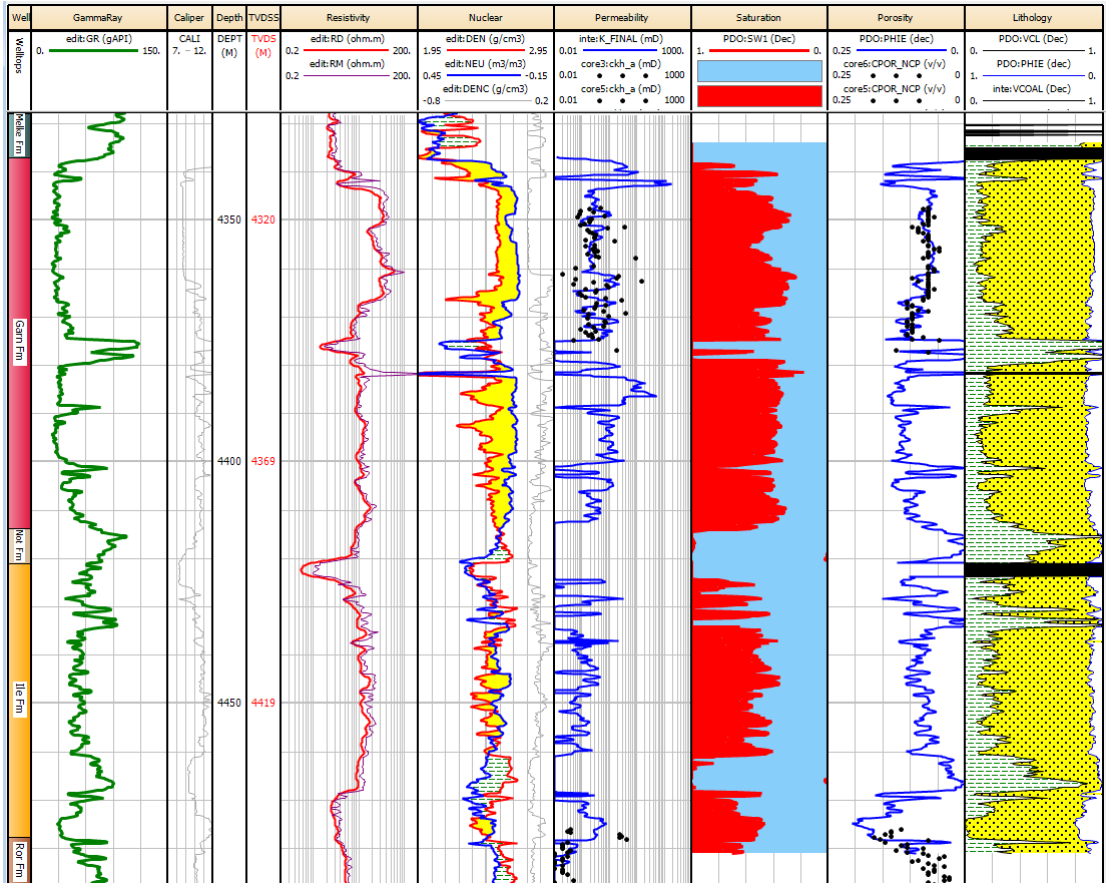


Figure 3.2-1: Log data of well A showing paleo residual gas saturations (DEA Norge AS, 2019).

When taking into account the low average water saturation in Garn and Ile Fm. in Table 3.2-1, the decision for carrying out a DST at the time drilling becomes reasonable: the average gas saturation ( $1 - S_w$ ) is considerably high especially in Garn Fm, hence performing a DST was a considerable option.

Table 3.2-1: Average properties of well A (DEA Norge AS, 2019).

Zone	Top – Base [mTVDSS]	NTG [m/m]	Avg. $\Phi$ [vol/vol]	Avg. $S_w$ [vol/vol]	Avg. $S_g$ [vol/vol]
Garn Fm.	4307 – 4383	0,87	0,09	0,44	0,56
Ile Fm.	4390 – 4447	0,75	0,01	0,57	0,43

Visually inspecting the resistivity log in Figure 3.2-1 one can conclude a gas-bearing zone in the complete Garn Fm. Because of the DST, where this gas stayed primarily immobile, the gas-bearing zone can be identified as residual. The gas saturations vary between 0,42 and 0,6.

The average resistivity in the resistivity log in Figure 3.2-1 is determined around approximately 20 ohm\*m. The resistivity level is constantly high throughout the Garn Formation and shows no decrease due to water-bearing zones.

Ile Fm. shows equal behavior. The average resistivity is measured around approximately 20 ohm\*m. In Ile Fm. from 4435 mTVDSS downwards there is a drop in resistivity visible. Yet this drop seems not to be consistent over the lower Ile Fm. One can see an increase in the interval after some meter depth. The overall resistivity reading in this area is too high to justify the assumption of a fully water saturated zone.

Considering these findings, different cases were constructed. The cases mainly differ regarding their Gas-Down-To (GDT) scenarios (DEA Norge AS, 2019) as summarized in Table 3.2-2.

- Scenario I assumes a GDT to 4383 m and a paleo column height of 83 m from GWC at 4300 m. In this case, the residual gas bearing formation of interest is the Garn Fm. The residual gas column extension is limited by the assumption of a sealing Not Fm.
- Scenario II assumes a GDT to 4429 m, which is 46 m higher paleo column height compared to the first scenario and sums up to 129 m paleo column. In this case, the residual gas bearing formations of interest are the Garn and the Ile Fm. The residual gas column extension is limited by a resistivity drop, compare with log in Figure 3.2-1.
- Scenario III assumes a GDT to 4447 m, which has the highest paleo column height compared within the scenarios and sums up to 147 m paleo column. In this case, the residual gas bearing formations of interest are the Garn and the Ile Fm. The residual gas column extension is limited by the bottom of Ile Fm.

All three scenarios shall be implemented within the scope of the simulations performed within the scope of the thesis.

*Table 3.2-2: Gas-Down-To scenarios inferred from well logs (DEA Norge AS, 2016a).*

<b>Scenarios</b>	<b>GDT [mTVDSS]</b>	<b>residual gas- bearing formations</b>	<b>Not Fm. communication</b>	<b>residual gas column extension</b>
I	4383	Garn Fm.	sealing	
II	4429	Garn Fm., Ile Fm.	not sealing	limited above resistivity drop
III	4447	Garn Fm., Ile Fm.	not sealing	down to bottom of Ile Fm.

## 4 ONE-DIMENSIONAL CORE MODEL

The following chapter describes the development of the one-dimensional core model in Eclipse. The objective is to history match the imbibition saturation functions from the previously mentioned SCAL report (Weatherford, 2013). The history matched imbibition relative permeability and imbibition capillary pressure curves are necessary for conceptual model. The focus is further set on creating reasonable secondary drainage curves, which obey the remobilization threshold. Therefore the imbibition core model will be restarted under different well control mechanisms with secondary drainage saturation functions.

### 4.1 Data Origin

The input data for the core model was planned to originate from two different SCAL studies: Low rate water flooding (Weatherford, 2013) and depletion experiments (Stratum, 2020). Each study has been performed on different core samples. The low rate water flooding has been conducted on cores from well B, whereas the depletion experiments have been conducted on cores from well C.

Unfortunately, the results of the depletion experiments were delayed strongly during the thesis and could therefore not be implemented except one value.

All cores used in this study originate from the Garn Fm. For choosing the most representative core, the deepest core was chosen to implement the core model. Another focus was set on choosing cores from the low rate water flooding (Weatherford, 2013) study that have comparable properties as the cores from the new study. Taking into account the experimental schedule of the depletion experiments, the core properties of the core earliest in the schedule were chosen to be matched. An overview of the chosen cores is provided in Table 4.1-1. The most significant differences of the cores are linked to the core size. The core from the recent study (depletion experiments) has twice the length compared to the core length of the previous study (low rate water flooding).

*Table 4.1-1: Comparison of cores (Weatherford, 2013) and (Stratum, 2020).*

<b>Property</b>		<b>Core B</b>	<b>Core C</b>
Study		Low rate water flooding	Depletion experiments
Well		B	C
Depth	[m]	4272,27	4275,60
Core length	[cm]	6,07	12,87
Avg. diameter	[cm]	3,76	3,79
Bulk volume	[ml]	67,4	144,96
Pore volume	[ml]	8,49	19,50
Porosity	-	0,126	0,135
Klinkenberg corrected gas permeability	[mD]	11,4	14,02

The small size of the dataset in the SCAL report from 2013 meant that it was not possible to use only reported properties to build the core model. Whenever a lack was encountered of

necessary data to reproduce the experimental behavior, data from the post-PDO reference case of the field was used if possible. At some points, no data at all was available and parameters were used as history matching parameters within engineering reasoning.

## 4.2 Model Assumptions

As described in sub-chapter 3.1.6, the gas in the East structure is most likely very limited to liquid drop-out. Furthermore, the gas is consisting majorly of methane, it is not necessary to apply a compositional model. Hence, for the upcoming models a dry gas model will be assumed. Accordingly, a Black-Oil model (see sub-sub-chapter 2.4.5) instead of a compositional model will be applied. The Black-Oil model offers a valid representation using a dry gas model. This will allow for an overall simpler model which is beneficial facing limited amount of input data available.

In the core model, the grid is one-dimensional and directed vertically (z-axis is parallel to the vertical direction). One-dimensional grid models are usually used for laboratory experiments instead of field studies (Kleppe & Andersen, 2019). The grid dimensions are set to 1x1x51. Furthermore, the cross-section of the rectangular grid was corrected by a pore volume multiplier to achieve the cross-section of the spherical core. Due to the small dimensions of the experimental core and the resulting small flow rates, the lab unit system was chosen. Pressures are reported in atmosphere, volumes in cm<sup>3</sup> and lengths in cm.

### 4.2.1 Imbibition

The laboratory data used in this part of the thesis is performed on a core that is initially saturated with connate water saturation and maximum gas saturation. The transport equations for this case have been derived in sub-sub-chapter 2.4.6. Let L denote the total length of the core along the z-axis (due to vertical direction of the core). The “water tank” is introduced in sub-sub-chapter 4.2.1. The initial water saturation for the core and the water tank follows as

$$\begin{aligned} S_w(z, t = 0) &= S_{wc} \quad ; \quad (0 < z < L) \\ S_w(z, t = 0) &= 1 \quad ; \quad (z = 0) \end{aligned} \quad (4.2-1)$$

The relation between the connate water saturation and relative permeability has been introduced in equation (2.4-8). The in the report so called ‘system pressure’ is  $P_i$  (Weatherford, 2013).

$$P(z, t = 0) = P_i \quad ; \quad (0 < z < L) \quad (4.2-2)$$

The initial fluid distribution in the core model is achieved by enumeration. The initial water saturation is  $S_{wc} 0,133$  as reported by Weatherford. At the inlet the initial water saturation is set to unity, see also Figure 4.2-1, to mimic a water-exposed inlet. The initial pressure is set to 98,69 atm, and a ‘backpressure’ (modeled during imbibition – water flooding – as producer well control with constant BHP) is set to 98,69 atm to satisfy the reported concept of a ‘system pressure’. The initial conditions are summarized in Table 4.2-1.

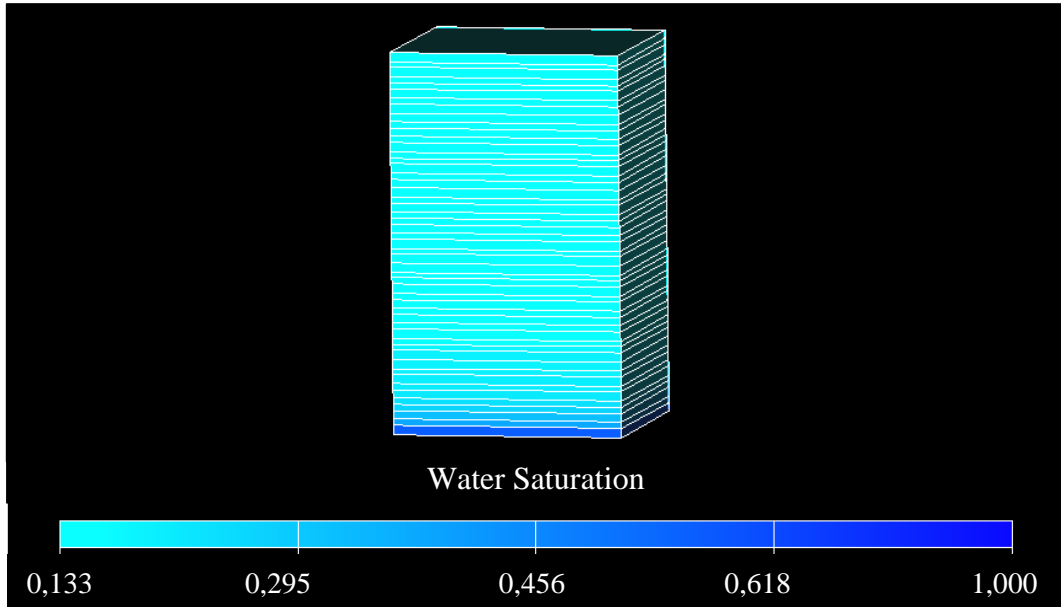


Figure 4.2-1: One-dimensional core simulation model with initial water saturation.

The boundary conditions of the experiments have not been reported in the laboratory report of Weatherford (2013). They were elaborated during modelling the processes. The inlet at  $z = 0$  is the water-exposed end face (created by “water tank”), the outlet at  $z = L$ . The history-matched boundary conditions can be described as

$$q_w(z = 0, t) = q \quad (4.2-3)$$

at the inlet, which is a constant flow boundary. At the outlet a zero capillary pressure is assumed, the phase pressures of gas and water are equal.  $P_B$  denotes backpressure.

$$\begin{aligned} P_c(z = L, t) &= 0 \\ P(z = L, t) &= P_B \end{aligned} \quad (4.2-4)$$

To mimic the boundary conditions for the inlet experimental setup, an injector was connected to the inlet cell of the grid. A producer was connected to the outlet cell. As discussed by Lenormand, et al. (2017), an important point is to achieve an equilibrium of the core with the fluids at the beginning of the simulation. For the purpose of creating a water-exposed inlet, a “water tank” was developed. This “water tank” has the same properties as the rest of the grid except the initial water saturation, which is set to unity.

During imbibition – water flooding – the residual gas saturation was determined by constant low rate liquid injection with a pump flow rate of  $4 \text{ Scm}^3/\text{h}$  (modeled during imbibition as injector well control with constant rate). The analysis was performed at ambient temperature conditions. The boundary conditions are summarized in Table 4.2-1.

Table 4.2-1: Initial conditions and boundary conditions of imbibition – low rate water flooding – study (Weatherford, 2013).

Grid dimensions			1x1x51
$S_{wc}$	[-]	0,133	
$P_i$	[atm]	98,69	
$q$	[Scm <sup>3</sup> /h]	4	inlet
$P_B$	[atm]	98,69	outlet

#### 4.2.2 Depletion

The imbibition model is restarted to change to secondary drainage saturation functions to properly model the depletion process. The transport equations for this case have been derived in sub-sub-chapter 2.4.6. The initial conditions of the depletion run differ from the initial conditions of the imbibition run. During imbibition,  $S_{gr}$  is established in the core, which accordingly is the initial gas saturation in this restarted run. The “water tank” at  $z = 0$  has already been introduced in sub-sub-chapter 4.2.1

$$\begin{aligned} S_w(z, t = 0) &= S_{gr} \quad ; \quad (0 < z < L) \\ S_w(z, t = 0) &= 1 \quad ; \quad (z = 0) \end{aligned} \quad (4.2-5)$$

The pressure during the imbibition process is controlled by the applied backpressure (see equation (4.2-4)). In the restarted run, the initial pressure starts from the pressure level of the last time step of the imbibition run.

$$P(z, t = 0) = P_{restart} \quad ; \quad (0 < z < L) \quad (4.2-6)$$

The initial water saturation is  $S_{gr}$  0,297 as reported by Weatherford. The initial pressure of the restart run is 98,69 atm. The initial conditions are summarized in Table 4.2-2.

The boundary conditions of the depletion run differ from the boundary conditions of the imbibition run. After restarting the imbibition model from its last time step, the well control mechanisms change. At the inlet, the injector is shut-in, which creates a no flow boundary. At the outlet, the producer is controlled by a reservoir fluid volume rate target. The reservoir fluid volume rate target determines the volume of the fluids ( $q_w$  and  $q_g$ ) produced when measured at the average hydrocarbon pressure in the field. Note that referring to earlier definitions (see sub-sub-chapter 2.4.5),  $q$  is positive for injection and negative for production.

$$q_t(z = L, t) = -q_{core} \quad ; \quad (q_{core} > 0) \quad (4.2-7)$$

$$\begin{aligned} q_w(z = 0, t) &= 0 \\ q_g(z = 0, t) &= 0 \end{aligned}$$

The boundary conditions are summarized in Table 4.2-2. The reservoir fluid volume rate target applied on the producer is set to 2 Rcm<sup>3</sup>/h. Furthermore, a well target pressure constraint is introduced which is set to 19,74 atm (roughly 80 % pressure decline as the production scenario planned for the East structure).



Table 4.2-2: Initial conditions and boundary conditions of secondary drainage – depletion – study.

$S_{gr}$	[ - ]	0,297	
$P_{restart}$	[atm]	98,69	
$q_t$	[Scm <sup>3</sup> /h]	0	inlet
$q_{core}$	[Rcm <sup>3</sup> /h]	2	outlet
$P_{target}$	[atm]	19,74	outlet

### 4.3 Creation of the Saturation Functions for the History Match

As described earlier, the main objective of the core model is to determine reliable saturation functions for the conceptual model. In the following, the procedure of obtaining the relative permeability curves as well as the capillary pressure curves are discussed.

The first step in this process is to create and history match the imbibition capillary pressure and relative permeability. When a sufficient match is reached, the imbibition model is restarted with generated secondary drainage functions to model the depletion process. Primary objective is here the compliance of the remobilization threshold.

It is necessary to implement a hysteresis model already in the imbibition modelling for being able to restart the model to perform secondary drainage studies with hysteresis. The keyword with the biggest relevance is the EHYSTR keyword. It is used to define hysteresis parameter and define the applicable hysteresis model. The capillary pressure hysteresis is always calculated using Killough's model. For the relative permeability hysteresis, the hysteresis model can be chosen by the user between Killough (sub-sub-chapter 2.6.1) and Carlson (sub-sub-chapter 2.6.2) hysteresis models. For this model, Killough's hysteresis for relative permeability was chosen.

#### 4.3.1 Saturation Endpoints

The saturation endpoints provided by the SCAL report from Weatherford are summarized in Table 4.3-1. The saturation endpoints have been introduced during sub-chapter 2.3 and most of them visualized in Figure 2.3-1, the maximum permeabilities further in sub-sub-chapter 2.4.4.

Note, that  $S_{wc} = S_{wcrit}$ . This implies, that there is no threshold between imbibition and secondary drainage of the water phase. The water phase is continuous and mobile over both processes.

Note also, that the previously discussed remobilization threshold for the secondary drainage is 0,021. This value is less than the lowest analogue values encountered as described in 2.7.3. Henceforth, it can be considered as a very optimistic approach.

Table 4.3-1: Saturation endpoints from SCAL report (Weatherford, 2013).

	<b>Imbibition</b> (water flooding)	<b>Secondary drainage</b> (depletion)
Critical gas saturation, $S_{gc}$	0,297	0,318
Residual gas saturation, $S_{gr}$	0,297	
Critical water saturation, $S_{wcrit}$	0,1331	
Connate water saturation, $S_{wc}$	0,133	
Maximum gas relative permeability, KRG	1	
Maximum water relative permeability, KRW	0,307	

#### 4.3.2 Relative Permeability

By curve fitting via modified Brooks Corey correlations (see sub-sub-chapter 2.4.4), all available data regarding the relative permeability for primary drainage and imbibition simulations was taken into account:

- The SCAL report from 2013 stated Corey exponents for water during primary drainage between 2,3 and 4,8 and during imbibition 4 (Weatherford, 2013).
- Running the experimental data in the core flow simulator Sendra (PRORES AS) gave an initial estimate of Corey exponents for gas during imbibition from 1,7 to 4,2. This supplementary data was provided by the supervisor Pål Østebø Andersen and merely used as a starting point for manual history matching.
- Furthermore, the imbibition relative permeabilities have been curve-fitted to the post-PDO reference case relative permeability of the field.
- In particular, the analysis of secondary drainage curves was problematic, since due to the delay of the Stratum experiments, no data was available. Secondary drainage Corey exponents were modified in order to obey the expected positioning towards the imbibition curves.

The final Corey exponents for primary drainage, imbibition and secondary drainage are summarized in Table 4.3-2 and visualized in Diagram 4.3-1.

Table 4.3-2: Curve-fitted and history matched Corey exponents.

	SCAL report	core flow simulator Sendra	<b>History matched</b> <b>/ curve-fitted</b>
Primary drainage	$N_w$ 2,3 - 4,8		3,7
	$N_g$		4,5
Imbibition	$N_w$ 4		4
	$N_g$	1,7 – 4,2	3,5
Secondary drainage	$N_w$		2
	$N_g$		5

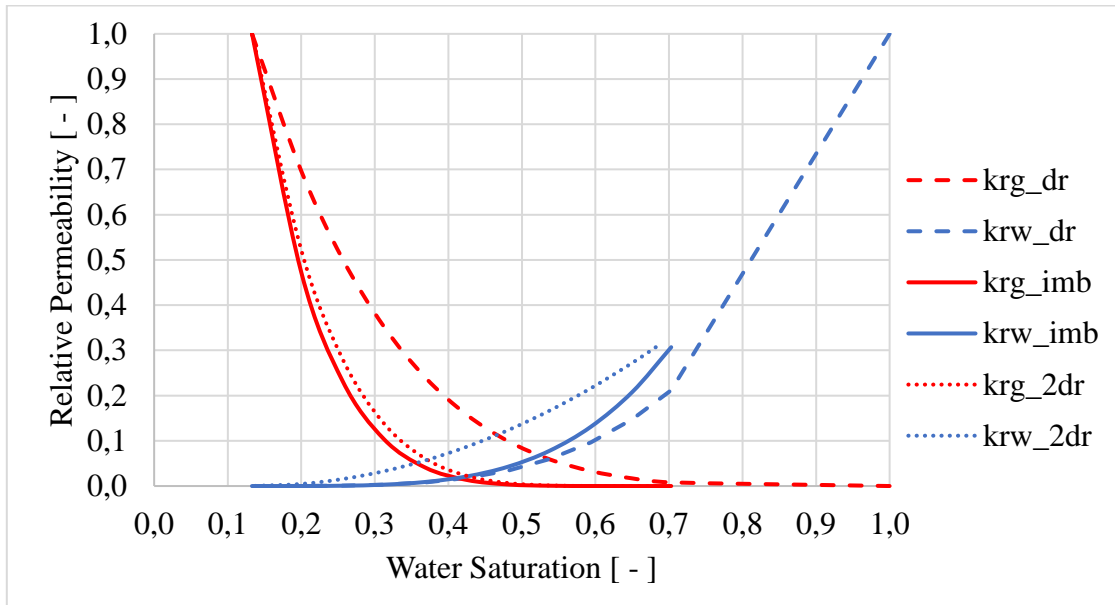


*Diagram 4.3-1: Curve-fitted and history matched Corey relative permeabilities: primary drainage (dashed), imbibition (solid) and secondary drainage (dotted) for water (blue) and gas (red).*

#### 4.3.3 Capillary Pressure

The SCAL report provides primary drainage capillary pressure curves for each core (Weatherford, 2013). Imbibition capillary pressure curves were created on basis of the reported drainage curves by shifting the drainage curve downwards within the residual gas and connate water saturation boundaries.

As for the relative permeability curves, the model was run in the core flow simulator Sendra (PRORES AS) to verify the modified imbibition curve. This supplementary data was provided by the supervisor Pål Østebø Andersen. Sendra provides the entry pressure and the pore size distribution index which are input parameters to the strongly water-wet Skjaeveland correlation, see sub-sub-chapter 2.4.3. The imbibition capillary pressure curve generated with the Sendra values and the Skjaeveland correlation were reproducing the modified imbibition capillary pressure curve to a great extent and approved the use of the modified curve.

There are certain problems with creating secondary drainage capillary pressure curves to capture the hysteresis effects discussed in sub-chapter 2.3 when no data is available. To avoid the usage of curves, that cannot be history-matched nor quality checked in another way, capillary pressure hysteresis assumed to be neglectable as a side effect in this study. The strongly water-wet sandstones will be exposed to very small wettability alteration and shows further a very short transition zone. Hence, it is reasonable to ignore contact angle hysteresis due to small size of the dataset. Accordingly, imbibition and secondary drainage capillary pressure curves will be assumed to be identical (Undeland, 2012).

The final capillary pressure curves for primary drainage, imbibition and secondary drainage are visualized in Diagram 4.3-2.

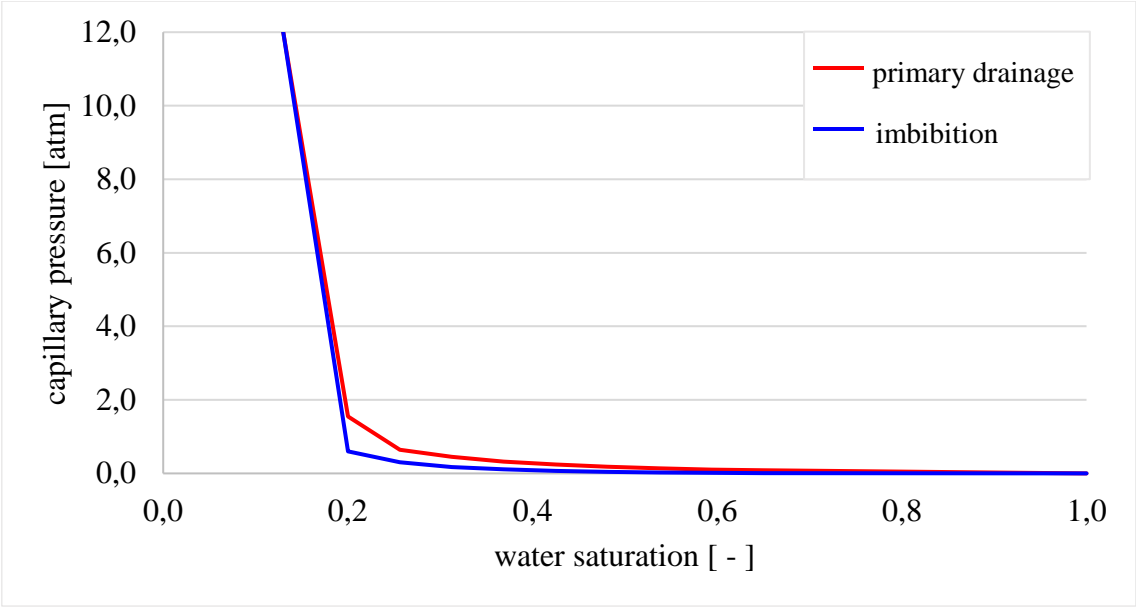


*Diagram 4.3-2: Curve-fitted and history matched capillary pressure curves. Secondary drainage not visible as it is assumed to be equal to imbibition curve.*

## 5 TWO-DIMENSIONAL CONCEPTUAL MODEL

The impact of paleo residual gas on water influx and recovery potential shall be investigated by a two-dimensional conceptual model.

A conceptual model was chosen because of the reduced computational time associated, and due to its simplicity compared to a full field model (FFM). Additionally, dealing with a green field limits the available data.

The objective of the conceptual model is to develop an initialization concept of the paleo residual gas column and give an understanding of the gas and water production behavior during depletion depending on the different scenarios.

### 5.1 Data Origin

Most of the data included in the conceptual model originates from a combination of the post-PDO reference case properties with the history-matched saturation functions of the one-dimensional core model. Where history-matched data is absent, analogue data from the systematic literature review of depletion is used to support engineering reasoning.

#### 5.1.1 Grid Specifications

The conceptual model consists of a two-dimensional, west-east cross-sectional model following the grid of the post-PDO reference case around well D with simplified geology.

The grid was build using corner point geometry to allow flexible grid building. When using corner point geometry, each corner of a grid block is located individually along specified coordinate directions and its depths specified from a reference level (Kleppe & Andersen, 2019).

The grid dimensions were chosen to be 31x1x73, which sums up to a total number of grid cells of 2263. The main features of the field have been included, e.g. the tilted layering of it with a dipping angle of averagely 14 degree toward the east.

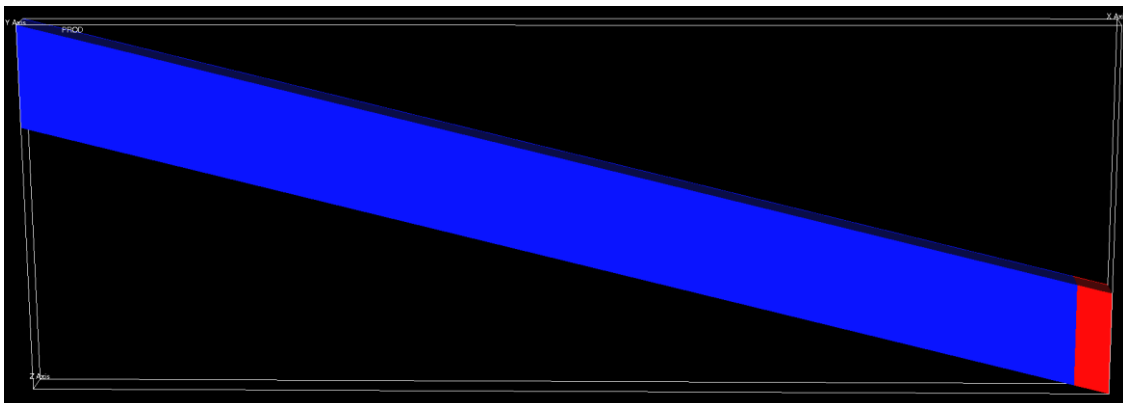


*Figure 5.1-1: Two-dimensional conceptual model with attached aquifer model (red).*

### 5.1.2 Properties

The porosity in the conceptual model is assumed to be uniformly distributed with a value of 0,077. This value is an average porosity estimate, which originates from the post-PDO reference case.

Fundamentally, also for the permeability of the conceptual model a uniform distribution is assumed with 5,2 mD in x- and y-direction and half of that for the z-permeability, i. e. 2,6 mD. Besides the uniform distribution of the permeability two further permeability scenarios are introduced. The well logs indicate the presence of two high permeability layer, both present in the upper part of the field in the Garn Fm. In the grid of this model, k-layer 5 and 6 are assigned to the upper high permeability layer and k-layer 30 and 31 to the lower high permeability layer. Their expansion is assumed to be over the complete i-array. The upper high permeability layer got a permeability assigned of 500 mD in x- and y direction and the lower a tenth of it, i. e. 50 mD. As for the uniform distribution, the z-permeabilities were set to half of the x- and y-permeabilities: 250 mD and 25 mD respectively.

The actual presence of the high permeability layers is uncertain and therefore the following scenarios have been invented, see Figure 5.1-2:

- scenario I: absence of both upper and lower high permeability layer
- scenario II: presence of only upper high permeability layer
- scenario III: presence of both upper and lower high permeability layer

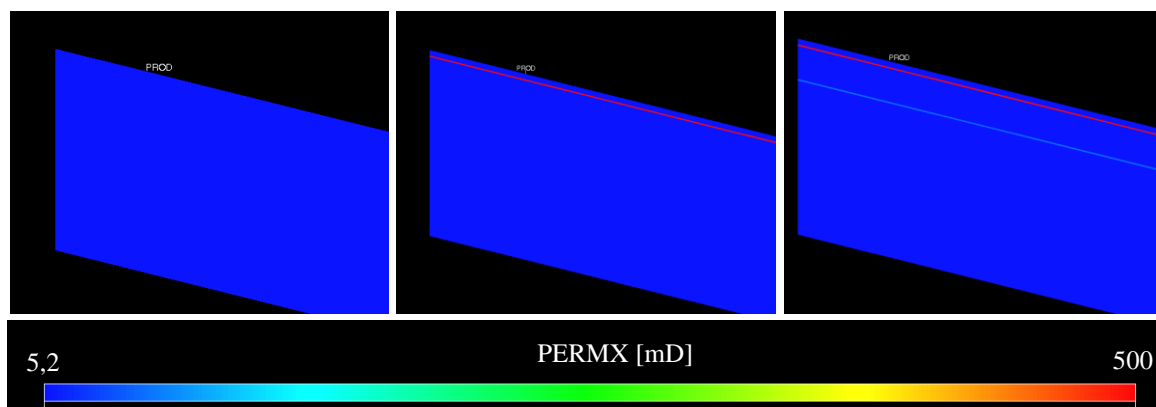


Figure 5.1-2: High permeability layer scenarios I to III from left to right.

The influence of the different scenarios on the water influx and recovery potential are going to be examined during the sensitivity analysis.

To scale the capillary pressure curves applied in the core model to the new porosity value and the non-uniform permeability distribution, a Leverett J-function was introduced, see sub-sub-chapter 2.4.3. The Leverett J-function was created using the core porosity and permeability. A fluid surface tension from 72 dynes/cm was constantly applied.

Table 5.1-1: Properties of conceptual model.

Grid dimension		31x1x73		
Top Depth	[m]	4272,27		
Pore Volume	[m <sup>3</sup> ]	7 053 449		
Porosity	[ - ]	0,077		
Permeability	X, Y	[mD]	5,2	
	Z	[mD]	2,6	
	<i>upper high k layer</i>	X, Y	[mD]	500
		Z	[mD]	50
	<i>lower high k layer</i>	X, Y	[mD]	250
		Z	[mD]	25
Surface tension applied in J-function	[dynes/cm]	72		

### 5.1.3 Wells

The producer is located structurally high, following the placement of well D of the field. The well is constantly perforated down to layer 32, which is one layer deeper than the lower high permeability streak will be placed in the upcoming sensitivity scenarios.

The producer is controlled by gas rate with a target rate of 1E5 Sm<sup>3</sup>/day. When falling off plateau, the control mechanism changes to a minimum BHP target of 140 bar, which aims to fit the planned abandonment pressure of averagely 120 bar of the field. For simplicity vertical lift curves were neglected, which is reasonable because the focus lays in reservoir flow mechanism.

## 5.2 Initialization and Saturation Regions

### 5.2.1 Initialization

To get a reliable foundation for the simulation, the paleo gas columns have to be initialized correctly below the free water level. The approach used has been indicated by Babadimas (2017) and Taggart (2019) but it was unsure, if initialization was possible with the applied Killough hysteresis model. While Babadimas used Hustad's model, neglected Taggart the usage of hysteresis completely in his study.

The authors proposed to initialize paleo gas columns below the free water level using negative capillary pressures. The level of negative capillary pressure is determined as follows in equation (5.2-1). It is the product of the density difference between the fluids in the column, the gravity and the column height of the paleo column  $d_{paleo}$ . This equation originates from equation (2.4-4), which has been introduced in earlier.

$$P_c = (B_g \rho_w - B_w \rho_w) * g * d_{paleo} \quad (5.2-1)$$

From chapter 2.3.2 it is known, that in case of post-charge water influx, imbibition  $P_c$  curves are used for initializing models and that the saturations below the present free water level are determined by saturation endpoints.

Diagram 5.2-1 shows the different capillary pressure level calculated for the three different paleo column height scenarios, here as example with an initial gas saturation in the paleo column of 0,5. The y-axis is crosses zero at the initial gas saturation in the paleo column  $S_{gi,paleo}$ .

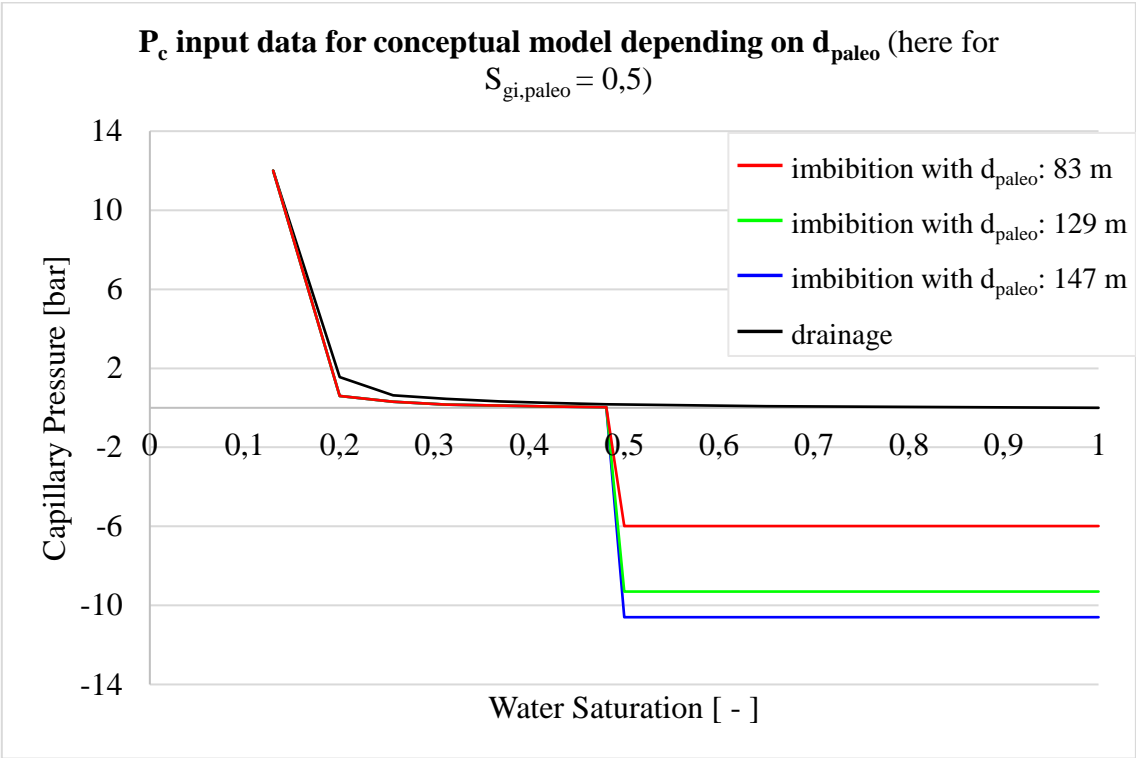


Diagram 5.2-1:  $P_c$  input data for conceptual model, paleo initial gas saturation 0,5.

The rapid transition from zero capillary pressure to negative capillary pressure has also been applied by the above-mentioned authors. Consequently, the transition zone is very short and saturation changes swiftly between the live and the paleo gas column as presented in Figure 5.2-1

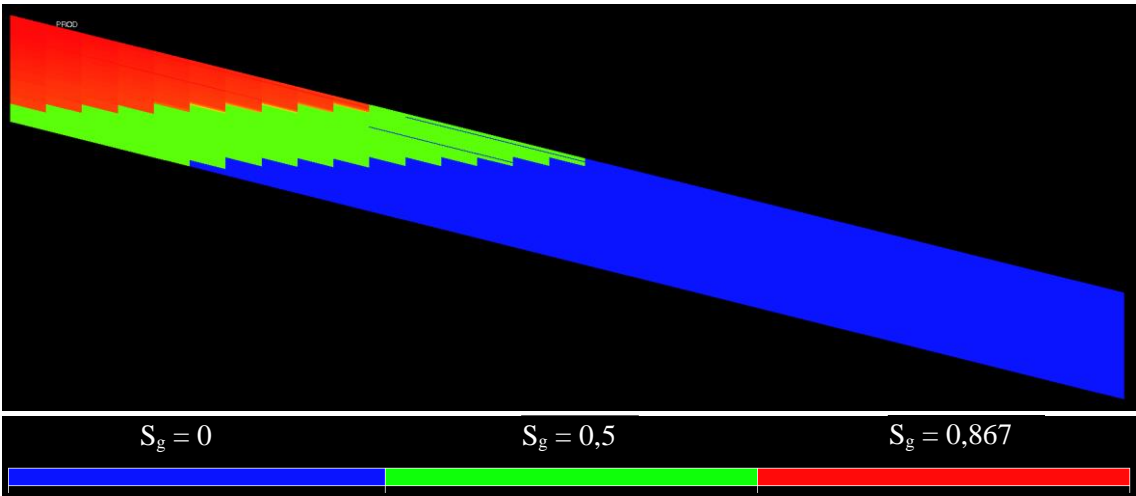


Figure 5.2-1: Example for initial fluid distribution, short transition zone.



### 5.2.2 Saturation Regions

The model is split into three different saturation regions (see Figure 5.2-2) to account for different processes taking place, e. g. imbibition or secondary drainage, and apply the associated saturation functions and endpoints. The saturation endpoints applied in the conceptual model are summarized in Table 4.3-1.

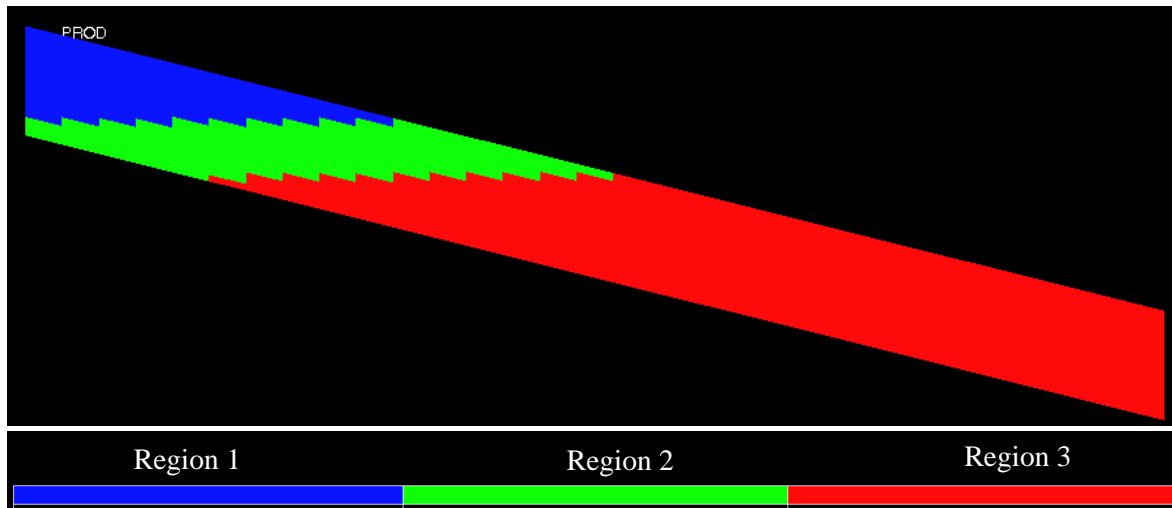


Figure 5.2-2: Saturation regions of conceptual model, exemplified for paleo gas column height of 147 m.

Region 1: The live gas column is treated as imbibition region that extends from the top of the model down to the GWC at 4300 m. In this region, a constant decrease of the gas saturation is expected. Since the saturation evolves linearly without change of direction, it is valid to apply only imbibition curves and hysteresis can be switched off (by setting SATNUM = IMBNUM in REGIONS section). When using imbibition saturation functions, gas is assumed to be present in a continuous phase and can mobilize immediately.

Region 2: The paleo gas column is treated as a secondary drainage zone starting at the GWC at 4300 m. The extension of the paleo gas zone depends on the GDT scenarios introduced in sub-sub-chapter 3.2.2. Further details about the GDT scenarios and the remobilization threshold will be discussed in sub-chapter 5.3.

The gas phase is discontinuous and immobile in the paleo column and needs to experience a saturation increase to reach critical gas saturation as has been introduced in the literature review. Secondary drainage saturation functions are made to account for this behavior. Killough's hysteresis model for relative permeability was applied. Note, that the capillary pressure hysteresis is to some degree neglectable, since the imbibition capillary pressure curve equals the secondary drainage capillary curves as discussed in 4.3.3.

Region 3: The water leg extends from the end of the paleo gas column to the end of the grid, where it is connected to an aquifer model, see sub-chapter 5.4. There is very little gas invasion expected into the water leg and therefore imbibition curves are applicable. Since also in this region the saturation evolves linearly (stays approximately constant) without change of

direction, it is valid to apply only imbibition curves and switch off hysteresis (by setting SATNUM = IMBNUM in REGIONS section).

### 5.2.3 Initial and Critical Saturations

Since the first data point from the new SCAL study from Stratum Reservoir occurred in time, the residual gas saturation of 0,42 of the system was taken from the experiments.

For simplification, the influence of rock quality on  $S_{gr}$  is neglected in this model:  $S_{gr}$  is assumed to be constant in every grid cell, see Table 5.2-1 for overview.

From visual inspection of the well log in chapter 3.2.2 it is known, that the initial saturation of the paleo residual gas column varies between 0,42 and 0,6. This range shall be implemented in the simulation study, assuming three initial paleo gas saturation ( $S_{gi,paleo}$ ) cases: 0,42 – 0,5 – 0,6, see Table 5.2-1 for overview.

As discussed during sub-chapter 2.7, the simplification of disregarding the gas remobilization threshold will result in poor recovery estimates. The most significant parameter of this study is therefore the critical gas saturation.

At the present date, there is no experimental critical gas saturation estimate available for secondary drainage processes in the field. The SCAL experiments aiming to achieve this parameter are still ongoing.

Therefore, the analogue data from the systematic literature review of depletion studies introduced in sub-sub-chapter 2.7.3 is used to estimate reasonable critical gas saturation saturations for the paleo residual gas column. In Diagram 5.2-2 the analogue critical gas saturation values are plotted against residual gas saturation. The distribution of the data points indicates a linear relationship. In the same manner, in Diagram 5.2-3 the analogue remobilization thresholds are plotted against residual gas saturation.

For the three different paleo gas initial saturations cases, three different remobilization thresholds are applied based on the analogue data. The literature indicates gas saturation remobilization threshold varies between 0,027 and 0,14, see sub-sub-chapter 2.7.3. A more conservative approach is chosen starting at 0,05 to cover the indicated range. The following three remobilization thresholds are applied to each paleo gas initial saturation cases: 0,05 – 0,1 – 0,15, see Table 5.2-1 for overview. Plotting the cases in Diagram 5.2-2 shows coincidence with the linear trend.

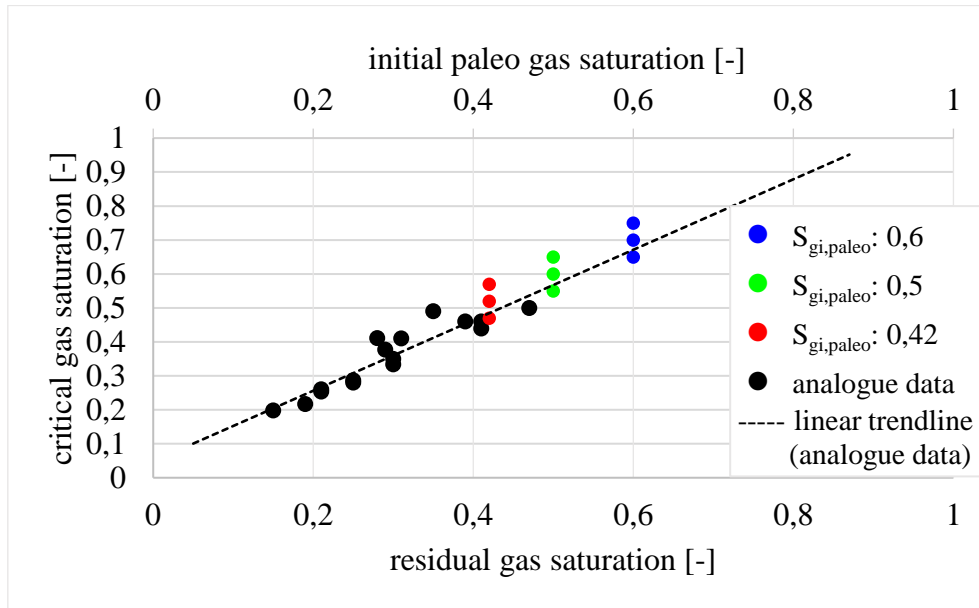


Diagram 5.2-2: Correlation between residual gas saturation and critical gas saturation from Table 2.7-1 (analogues) and sensitivity cases.

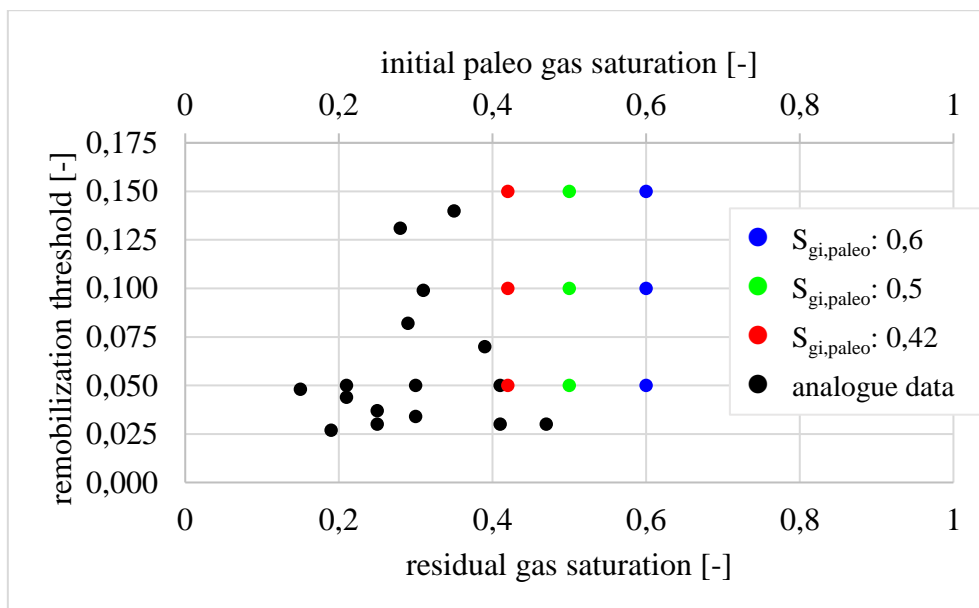


Diagram 5.2-3: Correlation between residual gas saturation and remobilization threshold from Table 2.7-1 (analogues) and sensitivity cases.

The saturation endpoints of the different regions (compare with sub-sub-chapter 5.2.2) applied in the conceptual model are summarized in Table 5.2-1. Endpoints originating from the core model (see Table 4.3-1) are highlighted with an asterix.

Note, that  $S_{wc} = S_{wcrit}$ . This implies, that there is no threshold between imbibition and secondary drainage of the water phase. The water phase is continuous and mobile over both processes.

Note the residual gas saturations throughout the paleo column cause a reduction in water mobility. Whereas the maximum water relative permeability is 1 in the aquifer, the water relative permeability in the paleo column is reduced to 0,307.

Table 5.2-1: Saturation endpoints applied in the conceptual model.

Mechanism	Region 1:	Region 2:			Region 3:
	Live Column	Paleo Column			Water Leg
	Imbibition	Secondary drainage			Imbibition
Initial gas saturation	0,867*	0,42	0,5	0,6	-
Critical gas saturation, $S_{gc}$ (dependent on remobilization threshold)	0,42	0,42	0,5	0,6	-
		0,47	0,55	0,65	
		0,52	0,6	0,7	
		0,57	0,65	0,75	
Residual gas saturation, $S_{gr}$	0,42	0,42			0
Critical water saturation, $S_{wcrit}$		0,1331*			
Connate water saturation, $S_{wc}$		0,133*			
Maximum gas relative permeability, KRG		1*			
Maximum water relative permeability, KRW	0,307*	0,307*			1

\*endpoints originating from the core model, compare with Table 4.3 1

### 5.3 Paleo Column Height

The extension of the paleo residual column is subject to uncertainty as discussed in the different GDT scenarios in sub-sub-chapter 3.2.2. That is why three different scenarios of the column extension build the starting point of each sensitivity analysis, see Table 5.3-1. The GWC is assumed to be at 4300 mTVDSS, see Figure 5.3-1.

- Scenario I: GDT to 4383 m, paleo column height of 83 m, Garn Fm. residual gas bearing formation
- Scenario II: GDT to 4429 m, 129 m paleo column height, Garn and Ile Fm. residual gas bearing formations
- Scenario III: GDT to 4447 m, 147 m paleo column height, Garn and Ile Fm. residual gas bearing formations

Note: Assuming here in scenario I that the Not Fm. is not sealing, is contradicting the original scenario. This disregard is done consciously and only for the purpose of better sensitivity assessment. The case shall be used as an extra sensitivity case to investigate the influence of paleo residual gas column height on various parameters. Sealing off the Not Fm. is a scenario more relevant for a three-dimensional FFM.

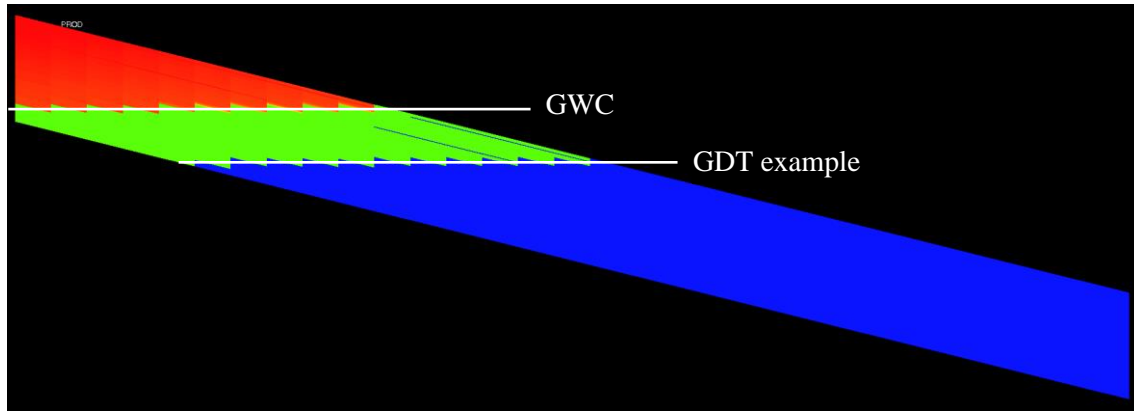


Figure 5.3-1: Example for initial GDT scenario.

Table 5.3-1: Gas-Down-To scenarios for simulation study, GWC assumed to be at 4300 mTVDSS.

Scenarios	GDT [mTVDSS]	Paleo column height [m]
GWC	4300	-
I	4383	83
II	4429	129
III	4447	147

## 5.4 Aquifer

Sub-sub-chapter 3.1.5 identified the aquifer connected to the East structure already as weak. Schlumberger (2016) names the Fetkovich aquifer model as good choice for limited aquifers. In small aquifers, the pseudo-steady state condition will be reached quickly. That means, that the propagation of the pressure depletion will reach the aquifer boundaries fast and spreads uniformly.

The main mechanisms controlling the aquifer productivity are aquifer flux due to pore-volume reduction, which is controlled by the total compressibility of the aquifer and water expansion by pressure depletion highly dependent on the initial water volume in the aquifer.

Criteria for selecting the aquifer parameter were as follows (summary in Table 5.4-1):

In the post-PDO reference case, the pore volume aquifer is three times the pore volume of the gas leg, see equation (5.4-1). The pore volume of the gas leg in the conceptual model is 2,36 E6 Sm<sup>3</sup>. Accordingly, the initial water volume  $V_{w0}$  was set to 7,1 E6 Sm<sup>3</sup>.

$$V_{w0} = 3 * PV_{gas\ leg} \quad (5.4-1)$$

$$V_{w0} = 3 * 2,36\ E6\ Sm^3 = 7,1\ E6\ Sm^3$$

The total compressibility  $c_t$  was taken over directly from the post-PDO reference case and set to 3 E-5 1/bar (DEA Norge AS, 2016b).

The productivity index J was set to 250 Sm<sup>3</sup>/day/bar, which complies with 0,25 percent of the gas production rate, see sub-chapter 5.1.3.

*Table 5.4-1: Aquifer parameters for weak aquifer behavior.*

<b>Parameter</b>		<b>Weak aquifer</b>
$V_{w0}$	$\text{Sm}^3$	7,1 E6
$c_t$	1/bar	3 E-5
J	$\text{Sm}^3/\text{day}/\text{bar}$	250

The aquifer is connected to all gas bearing layers in the east of the grid to represent edge-drive, see Figure 5.1-1.

Note: Since very little gas is displaced into the aquifer, which is trapped immediately due to the low saturations, there is no need for drainage curves in the aquifer.

## 6 RESULTS AND DISCUSSION

### 6.1 Core Model Simulations

The following sub-chapter summarizes and discusses the findings of the history matching of the core model. By history matching the experimental data, the modified saturation functions were quality checked for the purpose of integrating them reliably into the conceptual model.

#### 6.1.1 Imbibition

The imbibition core model aims to mimic the behavior of the low rate water flooding experiments as described in the previous sub-chapter 4.1.

Diagram 6.1-1, Diagram 6.1-2 and Diagram 6.1-3 present the results obtained by history-matching the experimental data of the SCAL report from 2013 for the cumulative gas production, the gas saturation and the differential pressure over time respectively.

The matches achieved for the cumulative gas production and the gas saturation over time show very little deviation from the historical experimental data. Furthermore, no significant differences were found between the history matched differential pressure over time and the historical experimental data. All characteristic features of the curve are reproduced by the history matched curve.

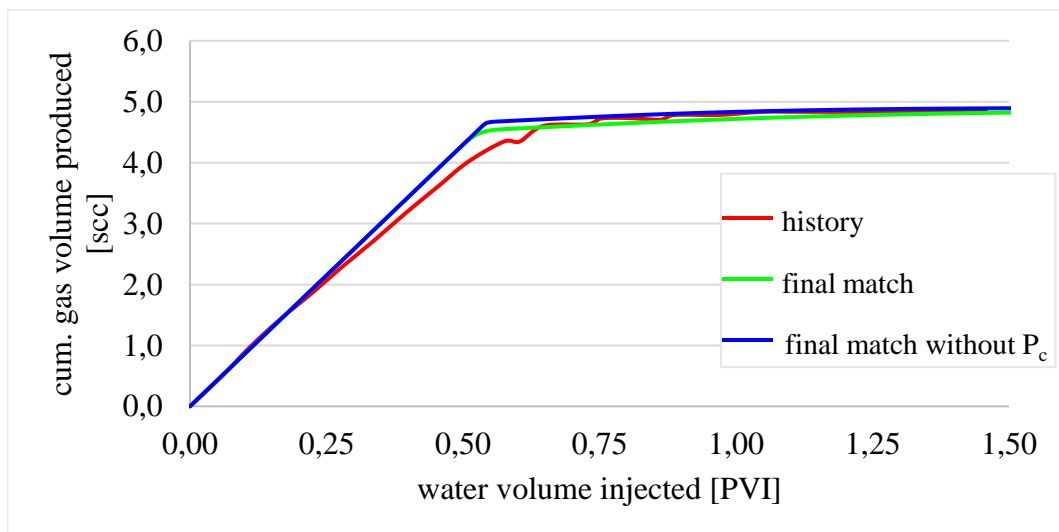


*Diagram 6.1-1: Final match of cumulative gas volume produced over pore volumes injected. All relevant features of the historical curve displayed by match.*

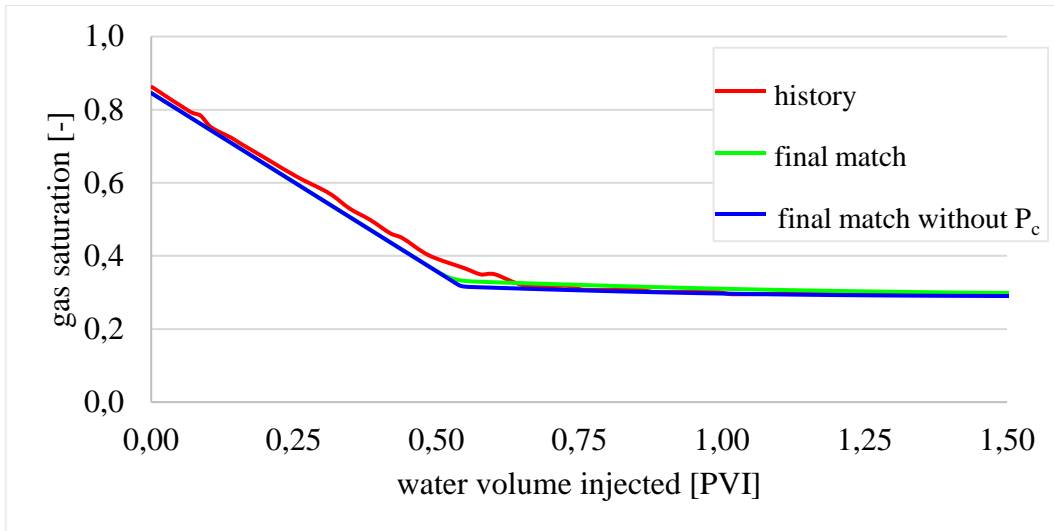


Diagram 6.1-2: Final match of gas saturation over pore volumes injected. All relevant features of the historical curve displayed by match.

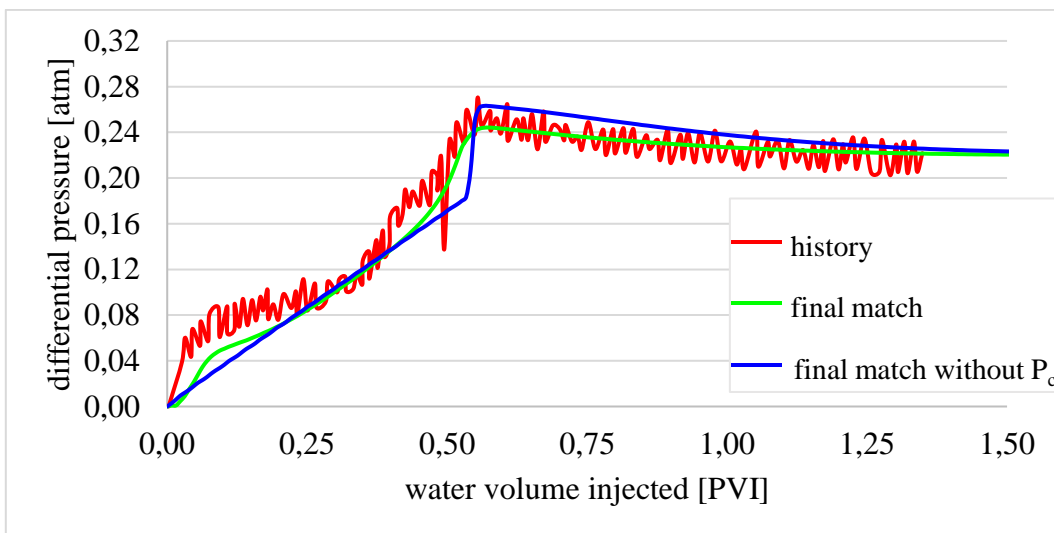


Diagram 6.1-3: Final match of differential pressure over pore volumes injected. All relevant features of the historical curve displayed by match.

Since it has been more challenging to achieve a good match for the differential pressure  $\Delta P$  data, it is worth a more detailed discussion. The main parameters improving the match were the Corey exponents. They influenced the shape of the differential pressure curve significantly.

The differential pressure curve can be subdivided in three zones, see Diagram 6.1-4:

- Zone I: dominated by gas production, pressure build-up until water breakthrough
- Zone II: transition zone dominated by simultaneous gas and water production, pressure peaks at water breakthrough
- Zone III: dominated by water production, pressure levels at constant value, when only water is flowing



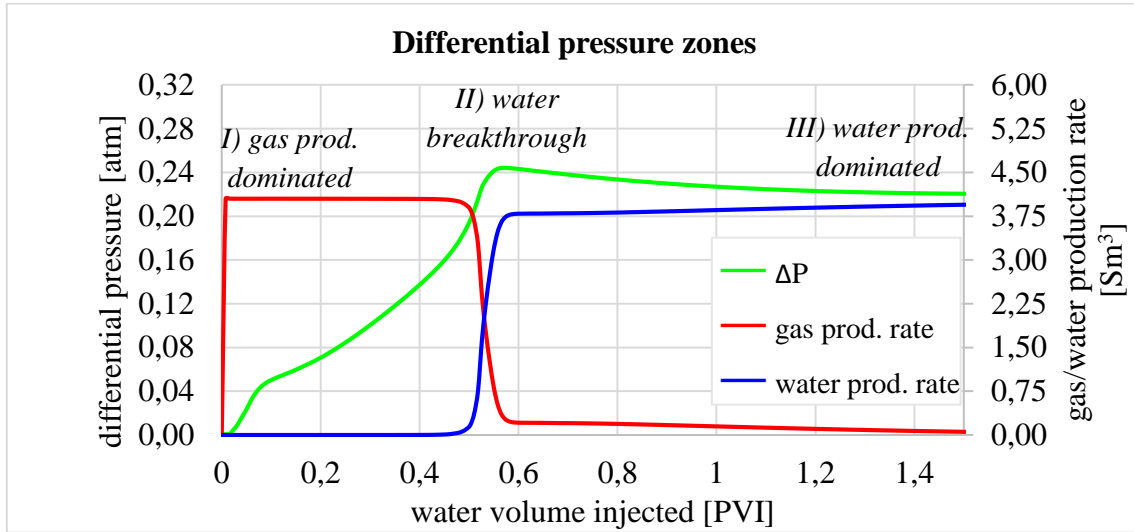


Diagram 6.1-4: Differential pressure can be subdivided into three zones depending on the fluid production.

These zones have implications on the effect changing either the water or the gas Corey exponent will have on the curve. A smaller Corey exponent causes a smaller curvature of the relative permeability curve, compare with sub-sub-chapter 2.4.4. This means, that mobility of the phase will increase faster.

Changing the gas Corey exponent affects mainly the transition zone between gas and water production of the differential pressure curve, see Diagram 6.1-5: smaller  $N_g$  causes smaller  $\Delta P$  peak. Changing the water Corey exponent affects mainly the outer zones of the differential pressure curve dominated by gas or water production respectively, see Diagram 6.1-6: smaller  $N_w$  causes smaller  $\Delta P$  in gas dominated zone and higher  $\Delta P$  in the water dominated zone.

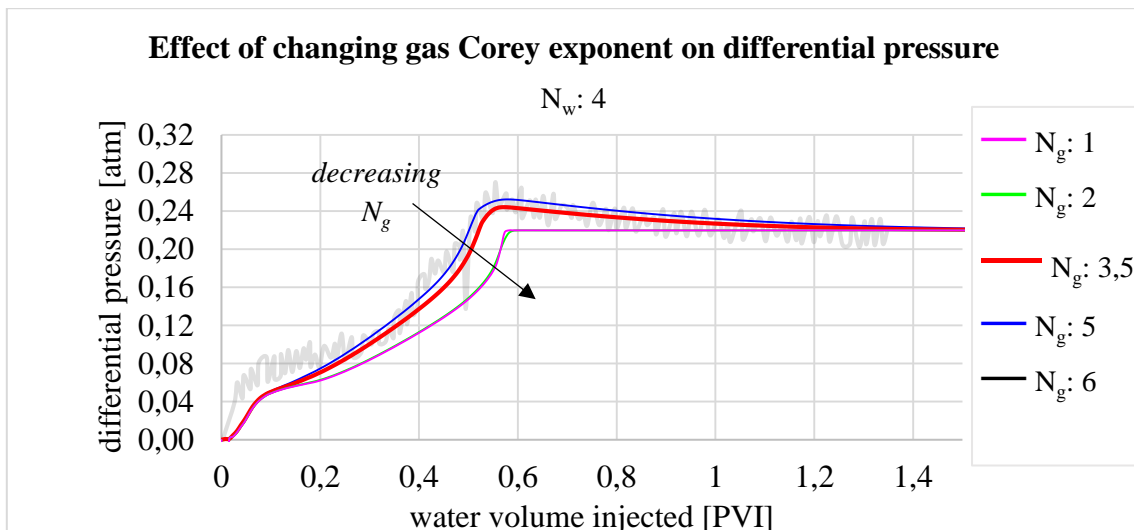
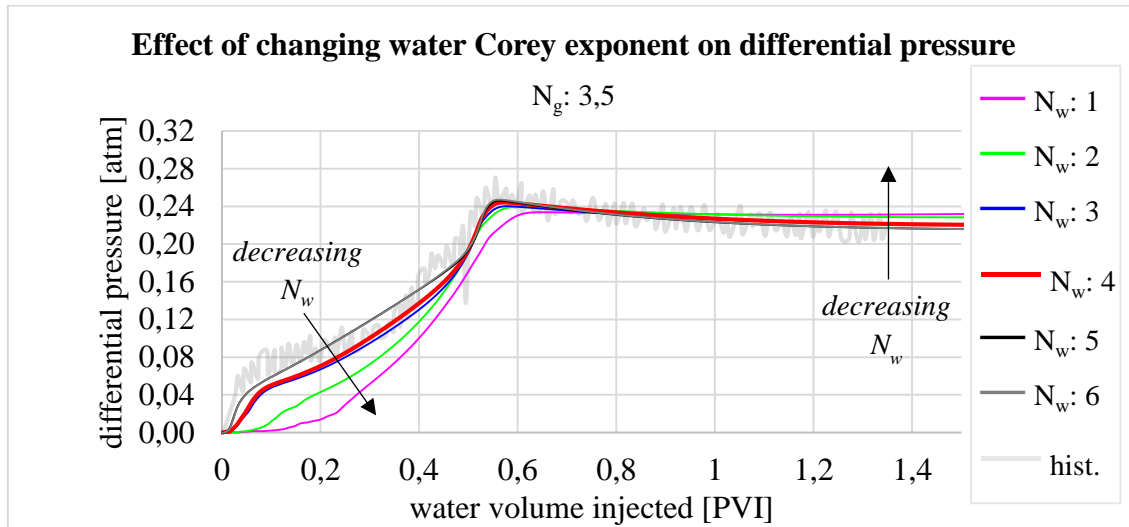


Diagram 6.1-5: Changing the gas Corey exponent affects mainly the transition zone between gas and water production of the differential pressure curve: smaller  $N_g$  causes smaller  $\Delta P$  peak.



*Diagram 6.1-6: Changing the water Corey exponent affects mainly the outer zones of the differential pressure curve dominated by gas or water production resp.: smaller  $N_w$  causes smaller  $\Delta P$  in gas dominated zone and higher  $\Delta P$  in the water dominated zone.*

Next to the final match including capillary pressure curves, also the matching results with applying no capillary pressures are shown in Diagram 6.1-1, Diagram 6.1-2 and Diagram 6.1-3. The small deviation by neglecting the capillary pressure illustrates, that in this water flooding study viscous forces are comparably more significant than capillary forces.

Lake et al., 2014 stated the condition  $P_c \gg \Delta P$  leads to a flow being dominated by capillary pressure (under the assumption of no gravitational forces). Comparing the range of  $\Delta P$  (averagely 0,084 atm before and averagely 0,224 atm after water breakthrough, see Diagram 6.1-3) with the range of  $P_c$  before and after breakthrough (averagely 2,35 atm before and averagely 4,00E-03 atm after water breakthrough, see Diagram 4.3-2) shows:

- Before water breakthrough:  $P_c > \Delta P$
- After water breakthrough:  $P_c < \Delta P$

Accordingly, viscous forces seem to become more important over the time of the water flooding. The viscous forces are dependent on the mobility ratio governing the gas-water system as introduced in equation (2.4-1). The mobility ratio in the present system is strongly dominated by the viscosity difference of the fluids ( $\mu_g \approx 0,02$  cP versus  $\mu_w = 0,23$  cP).

The observation,  $P_c < \Delta P$  after water breakthrough, might justify the assumption of a stronger piston-like displacement over time. The relative permeability of the phase mobilities are attributed to their endpoints because the complimentary phase is at their residual saturation in front of and behind the front (Lake et al., 2014).

Note, that due to the direction of the core in z-direction it is not valid to assume zero gravitational forces. Considering the gravitational term in transport equation (2.4-16) illustrates,

that the density of the fluids might also play a significant role. The gravitational forces are strongly dominated by the density difference of the fluids ( $\rho_g = 0,8 \text{ kg/m}^3$  versus  $\rho_w = 1066 \text{ kg/m}^3$ ).

The capillary pressure provided by the report has an untypical shape for a water-wet curve and behaves more characteristically for a mixed-wet system. Nevertheless, as it was the only capillary pressure curve that was available from laboratory experiments. It will be assumed to be reliable to that extend, that the overall influence on the system is small as shown before.

Overall, the good results of history matching the imbibition curves indicate well-defined saturations functions. Taken together, the saturation curves are verified by the history matching and provide a good foundation for the conceptual model.

6.1.2 Depletion

In particular, the analysis of the secondary drainage saturation functions was crucial, but problematic. In comparison to the imbibition saturation functions, there was no experimental data available to history match the model depletion. The delay of the SCAL experiments parallel to the thesis caused this lack of available data.

Therefore, the main objective of depleting the core model was to familiarize with hysteresis processes as well as to guarantee abundance of the remobilization threshold, i. e. the critical gas saturation. It is important to mention, that gas expands uniformly, which is visualized in Figure 6.1-1 at  $t = 5,089$ .

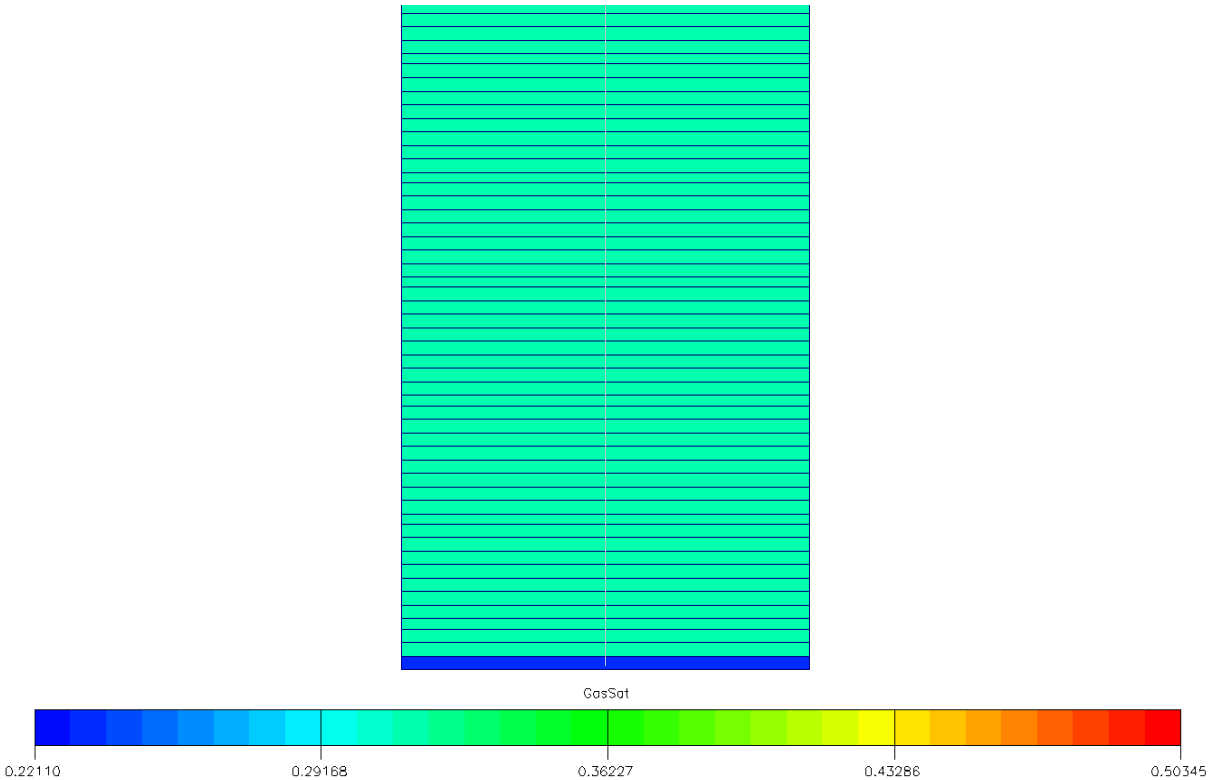


Figure 6.1-1: Uniform gas distribution during expansion in core model at  $t = 5,089$  just before remobilization.

Diagram 6.1-7 shows that the critical saturation of  $S_{gc} = 0,318$  is obeyed by the simulation model. At  $t = 5,089$  hrs, the gas saturation in the core is 0,317 – which is below the critical saturation. At the same time, the gas production is still 0. Hence, the condition for gas to be immobile below critical gas saturation is satisfied.

At  $t = 5,094$  hrs, the gas saturation in the core is 0,319 – which is above the critical saturation. At the same time, the gas production is 0,001  $\text{Sm}^3/\text{hr}$ . Hence, the condition for gas to be mobile again when exceeding the critical gas saturation is satisfied.

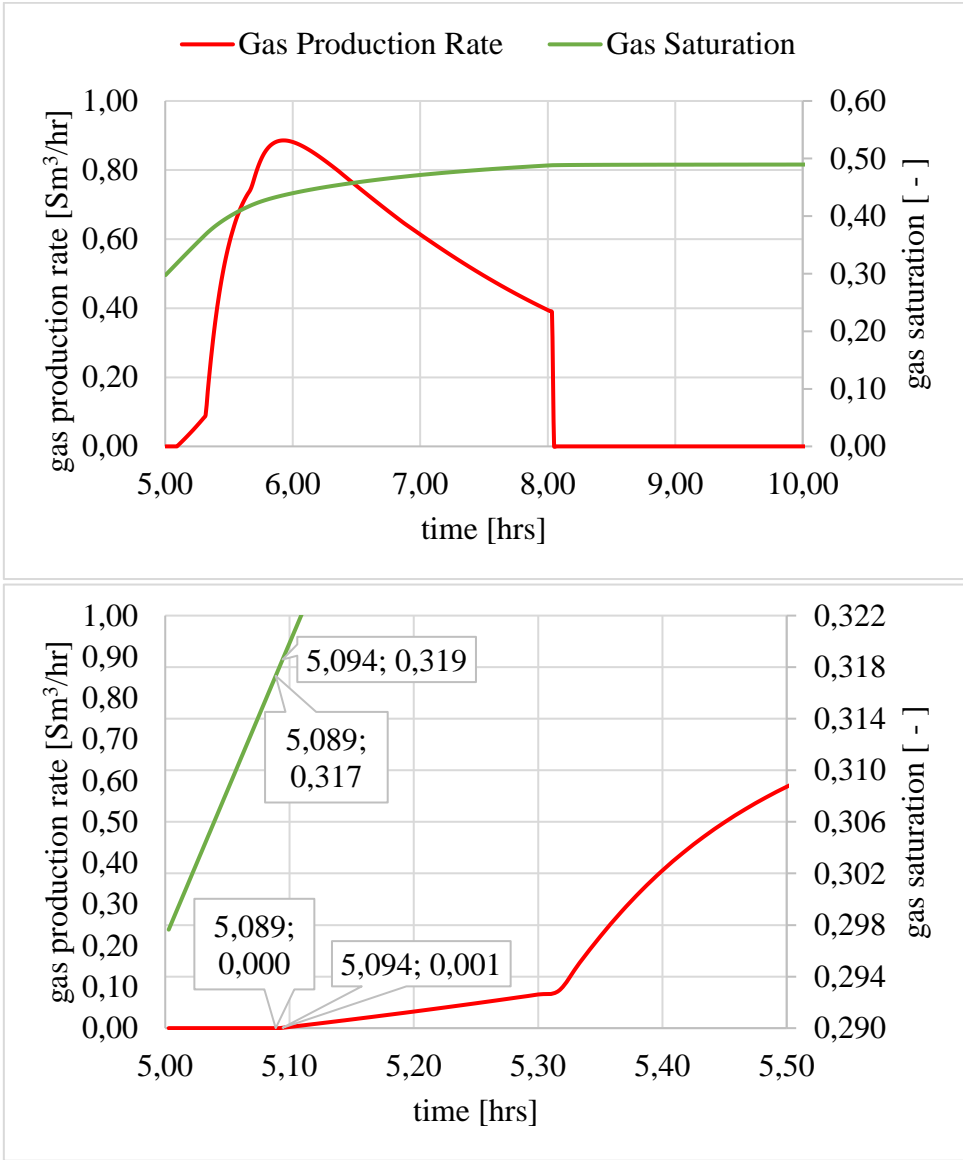


Diagram 6.1-7: Secondary drainage model gas production rate and gas saturation obeying the critical gas saturation  $S_{gc} = 0,318$ ; top: full 5 hours of simulation; bottom: enlarged first 0,5 hours of simulation.

The secondary drainage saturation functions will govern the gas recovery from the paleo residual column in the reservoir simulation. Therefore, it is crucial, that they are as reliable as possible despite the absence of laboratory data.

To quality-check the secondary drainage relative permeability, a sensitivity on the assigned Corey exponents has been run. The gas Corey exponent has been varied between 4 and 6 and the water Corey exponent between 1 and 6 respectively. The variation of either Corey exponent (see Diagram 6.1-8) had no influence on the water or the gas production during depletion within the applied production interval, which is limited by the well target pressure constraint, see Table 4.2 1. This insensitivity indicates that there might be an analytical solution to solve this problem.

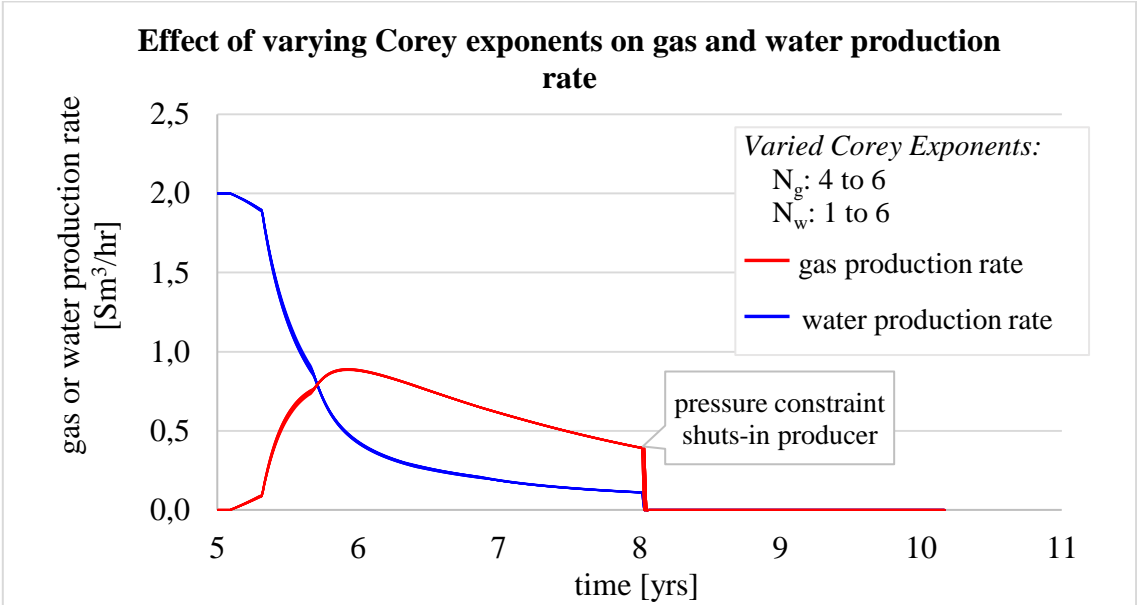


Diagram 6.1-8: No effect of varying either Corey exponent on gas or water production rate over time.

These results reflect those of Cense et al. (2016) who also found that the gas and water Corey exponents (that define the shape of the relative permeability curves) have less influence on the recovery.

However, the sensitive part of the relative permeability function is considered to be the maximum water (gas) relative permeability at residual gas (water) saturation, as illustrated in Diagram 6.1-9. Increasing KRW or decreasing KRG delays water and gas production.

Nevertheless, since these numbers were provided by the experimental SCAL study, they are assumed to be fairly accurate.

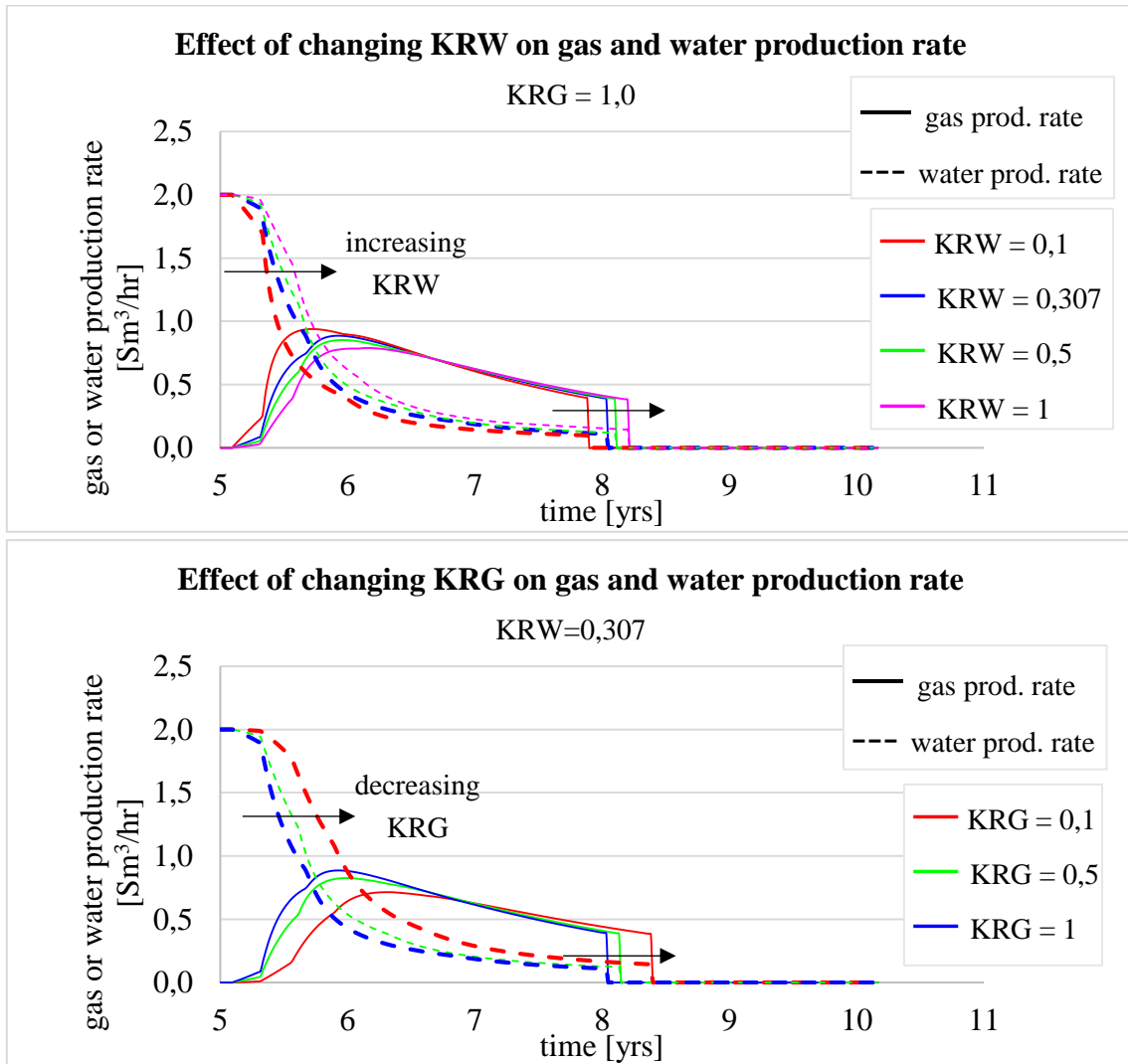


Diagram 6.1-9: Varying maximum relative permeability has influence on gas or water production rate over time: Increasing KRW or decreasing KRG delays water and gas production; top: varying KRW, bottom: varying KRG.

As discussed in sub-sub-chapter 4.3.3 the secondary drainage capillary pressure is assumed to be equal to the imbibition capillary pressure. This assumption follows Undeland (2012) approach and is the most reasonable to avoid over-engineering a secondary drainage capillary pressure.

Overall, the secondary drainage saturation functions have been created as reliable as possible. Since it was shown further, that they obey the remobilization threshold, they provide a good foundation for the conceptual model.

## 6.2 Conceptual Model Simulations

The following sub-chapter summarizes and discusses the findings of the sensitivity study of the conceptual model. The runs performed during this study are summarized in Figure 6.2-1. The runs are based on three different GDT scenarios (different paleo gas column height  $d_{paleo}$  as

developed in sub-chapter 5.3) and compared to a case without paleo gas saturations below FWL. Within the different paleo column height scenarios, the initial gas saturation  $S_{gi,paleo}$  is varied according to the log readings (see sub-sub-chapter 3.2.2) and as introduced in sub-sub-chapter 5.2.3. The gas saturations get different remobilization thresholds  $\Delta S_{g,remob}$  assigned as elaborated in sub-sub-chapter 5.2.3. Due to the uncertainty about the field-specific high permeability layers (see sub-sub-chapter 5.1.2), runs are performed with both high permeability layers, only the upper high permeability layer and no high permeability layer.

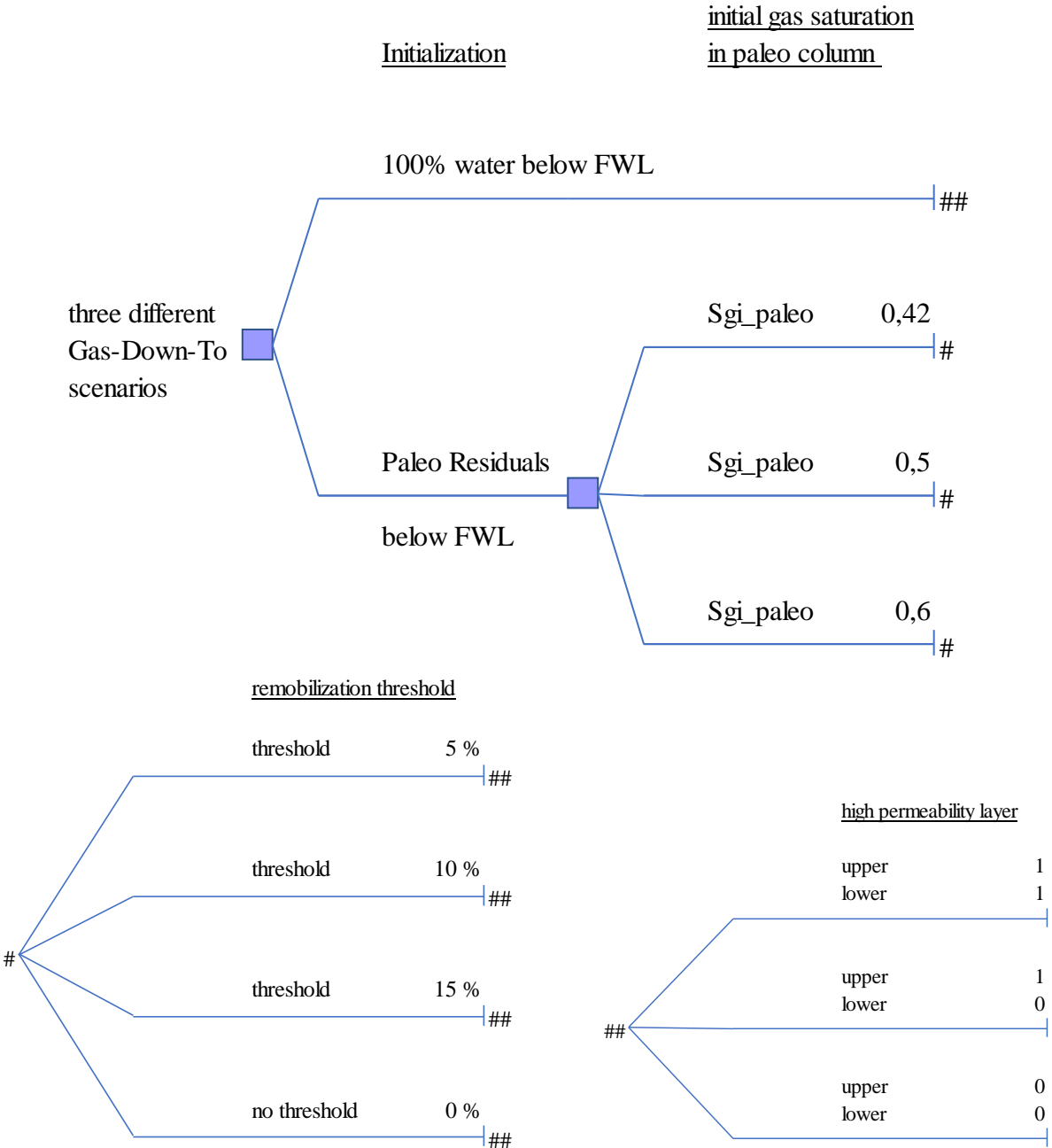


Figure 6.2-1: Fundamental sensitivity runs on conceptual model.

The present conceptual model captures the following field specific features, that are relevant for flow in the reservoir:

- The grid mimics the cross-section around the well D location including the dipping layers of the reservoir and both high permeability layers.
- Saturation functions for both imbibition and secondary drainage are based to a great extent on experimental data of field cores.
- The depth of the GWC stems from the post-PDO reference case.
- The GDT scenarios and the initial gas saturation of the paleo column originate from the log readings of the field.
- The weak, edge-drive aquifer behavior is in accordance with the post-PDO reference case.

Accordingly, the results of the simulation study presented in this sub-chapter may have implications for the field case. Probably, a great number of them will however be generally applicable.

### 6.2.1 Initialization

To get a reliable foundation for the simulation, the paleo gas columns have to be initialized correctly below the free water level. From chapter 2.3.2 it is known, that in case of post-charge water influx, imbibition  $P_c$  curves are used for initializing models and that the saturations below the present free water level are determined by saturation endpoints.

As described in sub-sub-chapter 5.2.2, the model is divided into different saturation regions: The live column saturation functions are imbibition functions and the paleo column saturation functions are secondary drainage functions. To quality-check the successful initialization and the proper application of the hysteresis models, observation cells were chosen in the live column and the paleo column to observe, if the remobilization threshold was obeyed.

Figure 6.2-2 shows the block gas saturation and the block gas production over time from block (2,1,32). Block (2,1,32) is situated in the live column and is therefore exposed to an imbibition process. That means, that the gas phase in this block is supposed to be continuous and remobilizes directly without threshold. The gas production from block (2,32,1) starts immediately with the field production. There is no threshold visible.

Figure 6.2-3 presents the block gas saturation and the block gas production over time from block (7,1,58). Block (7,1,58) is located in the paleo column and is therefore exposed to a secondary drainage process. That means, that the gas phase in this block should be discontinuous and a reconnection of the gas phase must take place before the gas remobilizes. The saturation threshold is varied between 0,05, 0,1 and 0,15 as introduced in sub-sub-chapter 5.2.3. Consistent with the literature, gas remobilizes only after achieving its critical gas saturation as illustrated by black arrows in Figure 6.2-3.

It may be the case therefore that the initialization method applied using Killough's hysteresis model gives a valid representation of the hysteresis state in the different regions, e. g. the remobilization thresholds during secondary drainage processes. This observation may contradict the hypothesis of Babadimas (2017) that the conventional hysteresis model of Killough is not able to do so.



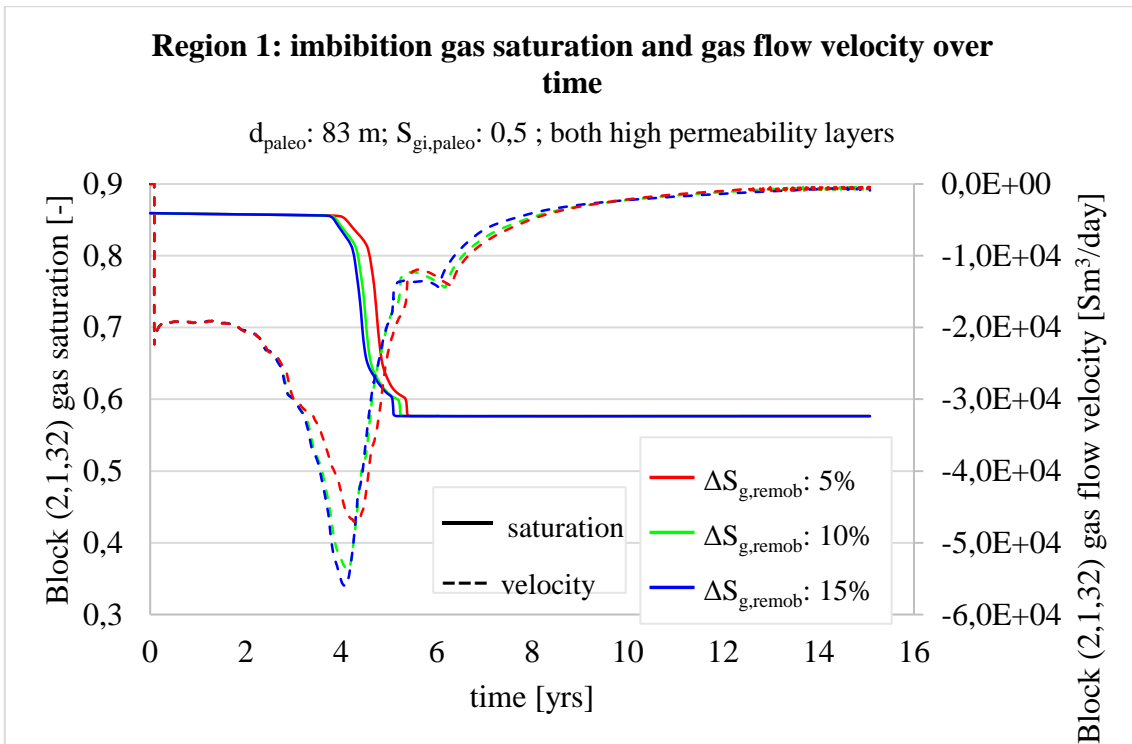


Figure 6.2-2: Observation grid block (2,1,32) in live column: gas production starts immediately without saturation threshold.

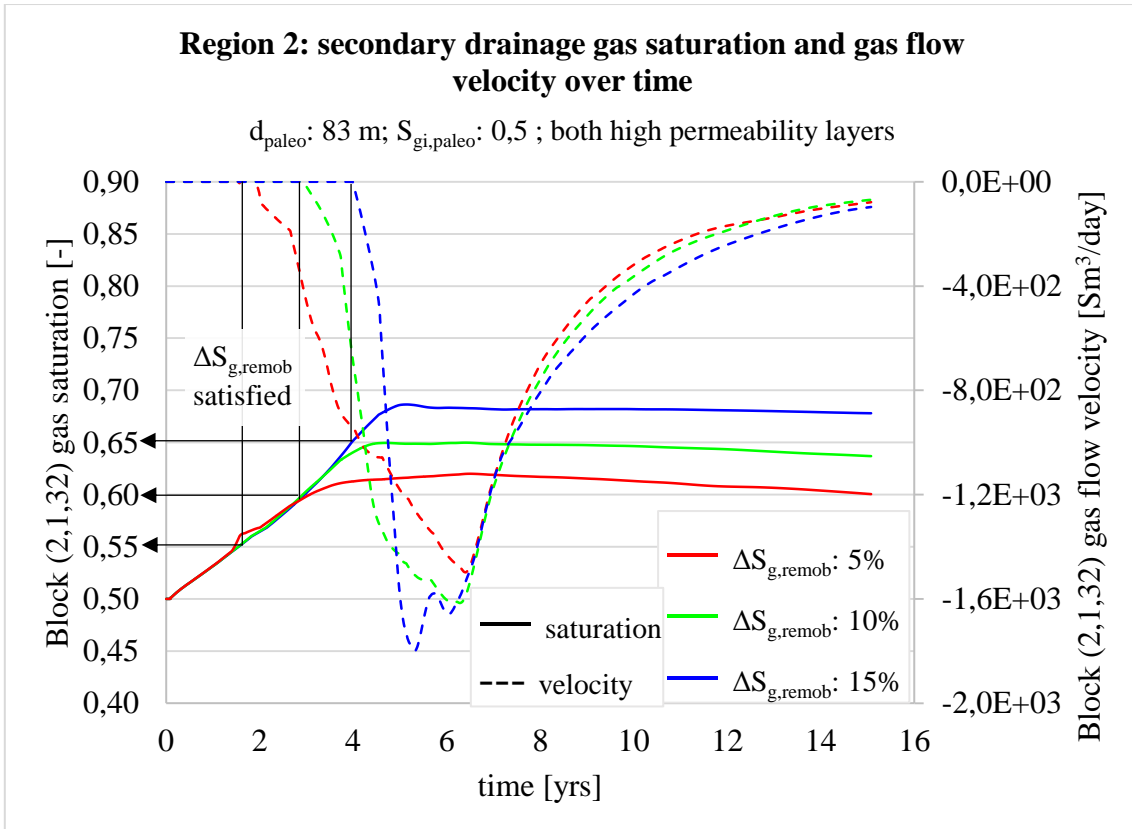


Figure 6.2-3: Observation grid block (7,1,58) in paleo column: gas remobilizes only after achieving its  $S_{gc}$  as illustrated by black arrows.

### 6.2.2 Recovery Potential

In order to assess the influence of paleo residual gas on recovery potential, a sensitivity study was conducted.

Firstly, the effect of column height ( $d_{paleo}$ ) and initial paleo gas saturation ( $S_{gi,paleo}$ ) on cumulative gas production has been assessed. Figure 6.2-4 shows the cumulative gas production over time for different  $d_{paleo}$  and for all remobilization thresholds ( $\Delta S_{g,remob}$ ) with a constant  $S_{gi,paleo}$  of 0,42. In the same manner, Figure 6.2-6 (Figure 6.2-6) illustrates the same behavior for a constant  $S_{gi,paleo}$  of 0,5 (0,6). From the three figures can be seen that:

- the cumulative gas production increases with increasing  $d_{paleo}$ .

This finding was also reported by Taggart (2019).

- the cumulative gas production increases with increasing  $S_{gi,paleo}$ .

In reviewing the literature, no data was found on the association between  $S_{gi,paleo}$  and cumulative gas production.

- the cumulative gas production becomes more sensitive towards the critical gas saturation with increasing  $d_{paleo}$  and with increasing  $S_{gi,paleo}$ .

Also, this correlation was not found in reviewing the literature.

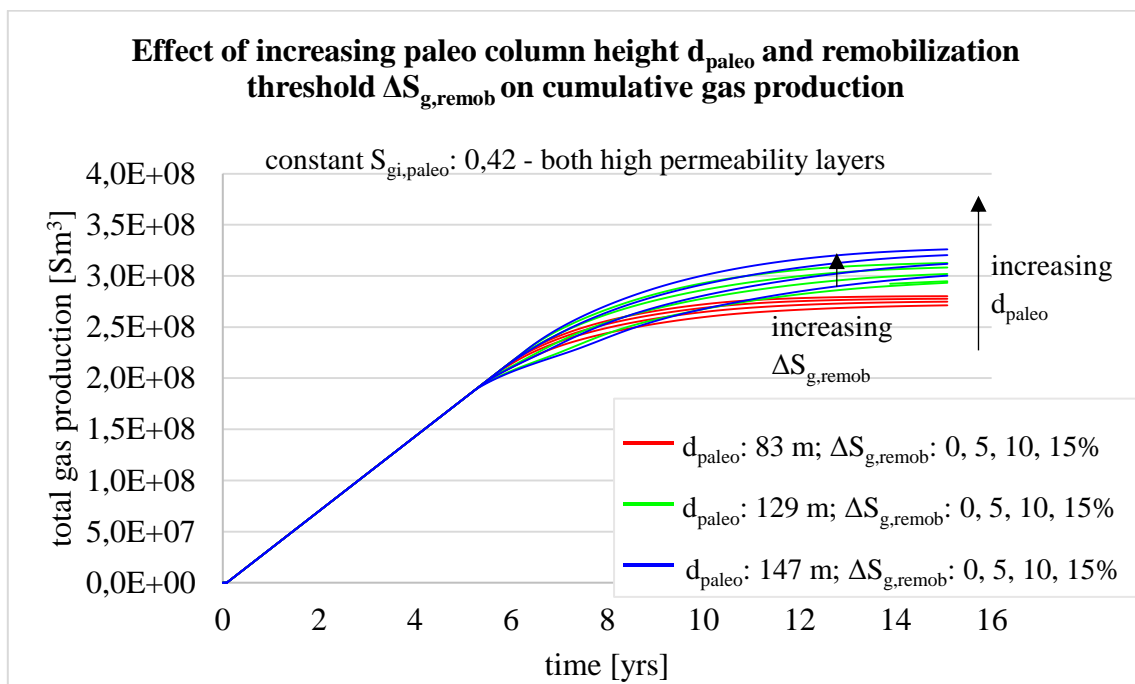


Figure 6.2-4: Cum. gas production vs. time,  $S_{gi,paleo}$  0,42: cum. gas production increases with increasing  $d_{paleo}$ , becomes more sensitive towards  $\Delta S_{g,remob}$  with increasing  $d_{paleo}$  and with increasing  $S_{gi,paleo}$ .

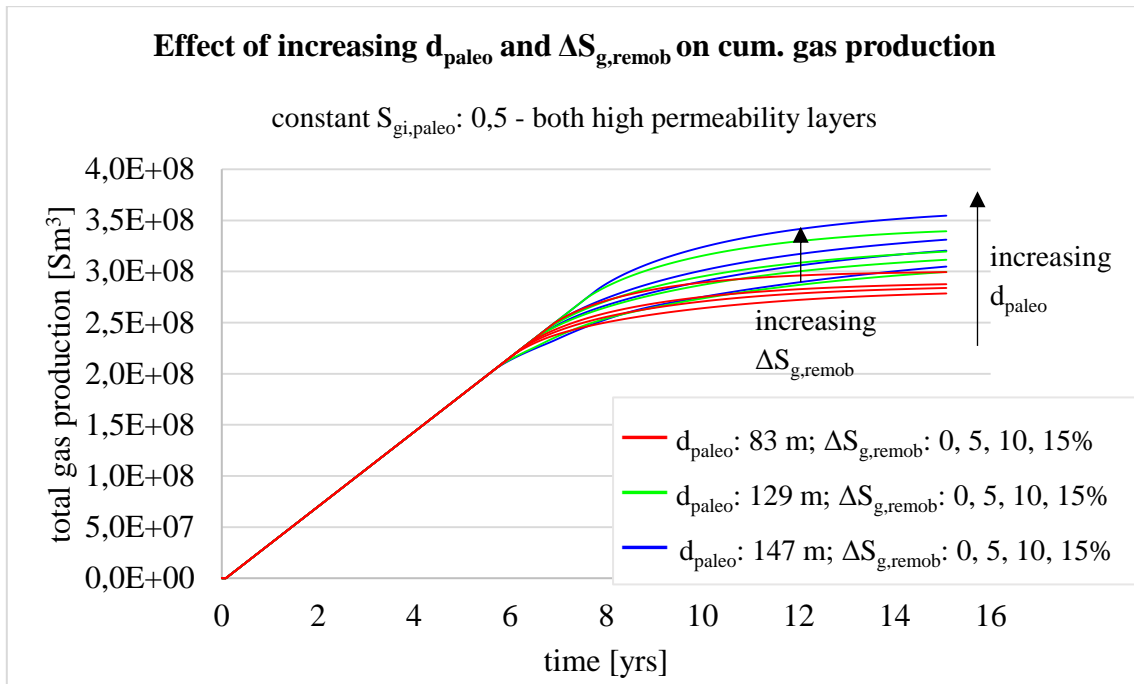


Figure 6.2-5: Cum. gas production vs. time,  $S_{gi,paleo}$  0,5: cum. gas production increases with increasing  $d_{paleo}$ , becomes more sensitive towards  $\Delta S_{g,remob}$  with increasing  $d_{paleo}$  and with increasing  $S_{gi,paleo}$ .

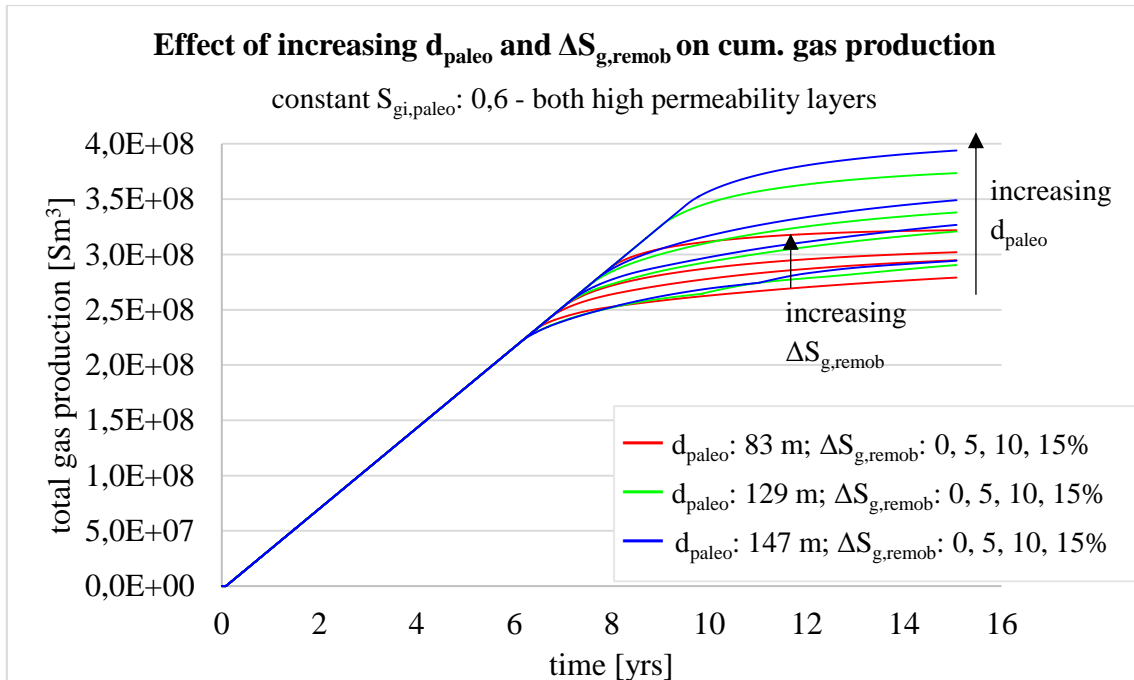


Figure 6.2-6: Cum. gas production vs. time,  $S_{gi,paleo}$  0,6: cum. gas production increases with increasing  $d_{paleo}$ , becomes more sensitive towards  $\Delta S_{g,remob}$  with increasing  $d_{paleo}$  and with increasing  $S_{gi,paleo}$ .

The next question of interest was the correlation between  $\Delta S_{g,remob}$  and plateau production. The result obtained from this analysis are summarized in Figure 6.2-7 with the example of  $S_{gi,paleo}$  of 0,6 at smallest  $d_{paleo}$  (83 m).

It can be seen, that

- a higher  $\Delta S_{g,remob}$  causes an earlier fall off of the production plateau.

The earliest fall off is observed when  $\Delta S_{g,remob}$  of 0,15 is applied. The longest period of plateau production is observed, when no threshold is applied. Nevertheless, in comparison to the case without having a paleo gas column, the plateau is still maintained over a longer period.

The reason for this behavior, is that the total amount of movable saturation is highly dependent on  $\Delta S_{g,remob}$ . The higher  $\Delta S_{g,remob}$  is, the higher is the critical gas saturation and the more gas stays immobile in the pore space. These results are in agreement with Babadimas' (2017) findings which showed modelling secondary drainage with  $\Delta S_{g,remob}$  will reduce trapped gas recovery.

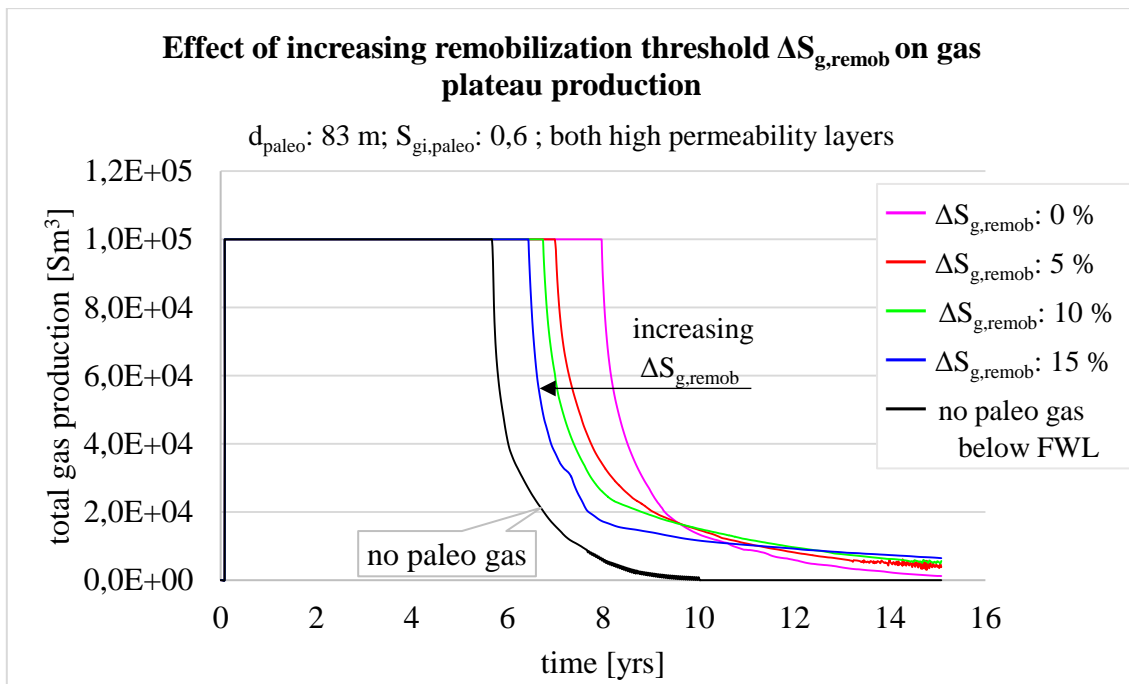


Figure 6.2-7: Gas production rate over time for different  $\Delta S_{g,remob}$ : a higher  $\Delta S_{g,remob}$  causes an earlier fall off of the production plateau.

These findings have implications on the total gas production. To quantify the recovery potential, the end members of the sensitivity study were chosen, representing the most optimistic and the most pessimistic case with regards to gas production.

As optimistic case the case with the highest  $d_{paleo}$  (147 m), the highest  $S_{gi,paleo}$  (0,6) and the lowest  $\Delta S_{g,remob}$  (+0,05) has been identified. Additionally, the optimistic case has been added without taking into account  $\Delta S_{g,remob}$ . As pessimistic case the case with the lowest  $d_{paleo}$  (83 m), the lowest  $S_{gi,paleo}$  (0,42) and the highest  $\Delta S_{g,remob}$  (+0,15) has been chosen.

The results have additionally been compared with the case without paleo gas saturations.

The results of this analysis are provided in Table 6.2-1 showing an increase in total production of minimum 20 percent (total 272 MSm<sup>3</sup>) up to maximum 55 percent (total 350 MSm<sup>3</sup>) compared to having no residual gas column below free water level (total 226 MSm<sup>3</sup>).

Disregarding the  $\Delta S_{g,remob}$  leads to a production increase of 44 MSm<sup>3</sup> from the optimistic case and causes a total incremental production of 74 percent (total 394 MSm<sup>3</sup>) compared to the case without paleo gas. This illustrates how

- disregarding of the  $\Delta S_{g,remob}$  can lead to strongly overestimation of recovery potential.

These result reflects those of Babadimas (2017) who also found that neglecting  $\Delta S_{g,remob}$  will cause overprediction of gas production.

Table 6.2-1: Preliminary recovery potential of paleo residual gas (KRG = 1).

Scenarios	Total gas production [MSm <sup>3</sup> ]	Increment [MSm3]	Increment
No paleo gas	226	-	-
pessimistic	272	46	+20 %
optimistic	350	124	+55 %
<i>No threshold (optimistic)</i>	<i>394</i>	<i>168</i>	<i>+74 %</i>

The present study was further designed to determine the effect of the high permeability layers in the field on the recovery potential facing paleo gas production.

The influence of the high permeability layers on the total gas production is evident in Figure 6.2-8.

- The absence of the high permeability layers for the paleo gas bearing cases with  $\Delta S_{g,remob}$  shows a reduction in the total gas production.

On the opposite, the absence of the high permeability layers has little effect on total gas production for the case without paleo gas and the case with paleo gas but without  $\Delta S_{g,remob}$ .

The process of gas remobilization is highly pressure dependent as discussed in the literature review and the high permeability layers allow for stronger pressure depletion throughout the reservoir. They act as highly prolific zones and enhance gas inflow into the well. What can further be stated, is that the differences in any case between the presence of both or only the upper high permeability layer were insignificant.

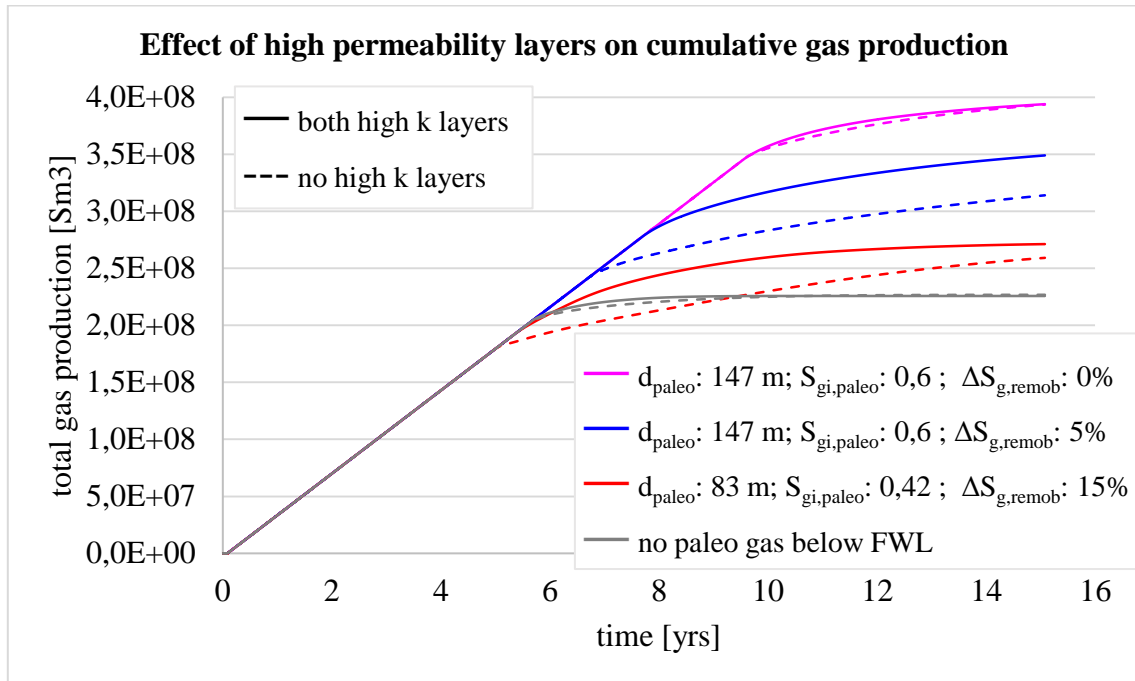


Figure 6.2-8: Cum. gas production vs time, subjected to absence of high permeability layer: absence of the high permeability layers for the paleo gas bearing cases with  $\Delta S_{g,remob}$  shows a reduction in the total gas production.

The levels of paleo gas production observed in this investigation are above expectations. The reason for this high gas production might be a too high gas mobility in the paleo column. The endpoint of the maximum gas permeability (KRG) for the secondary drainage curve was neither history-matched nor extracted from literature. Sensitivity was extended to KRG.

As discussed in sub-sub-chapter 6.1.2, the shape of the relative permeability curve has little influence on the production. Accordingly, only KRG has been reduced for the secondary drainage curve (from 1 to 0,5 and 0,1). The results of this sensitivity are visualized in Figure 6.2-9 and summarized in Table 6.2-2 and Table 6.2-3 respectively.

- A reduction of KRG to 0,5 (0,1) leads to a decrease in the cumulative gas production of 1 % (2%) in the pessimistic case and 2 % (8 %) in the optimistic case.

Undeland (2012) conducted similar sensitivity runs on the maximum gas relative permeability with the result of a 9% lower recovery of paleo residual gas for  $KRG = 0,5$  compared to  $KRG = 1,36$ . Also, in her study the effect of changing KRG was moderate.

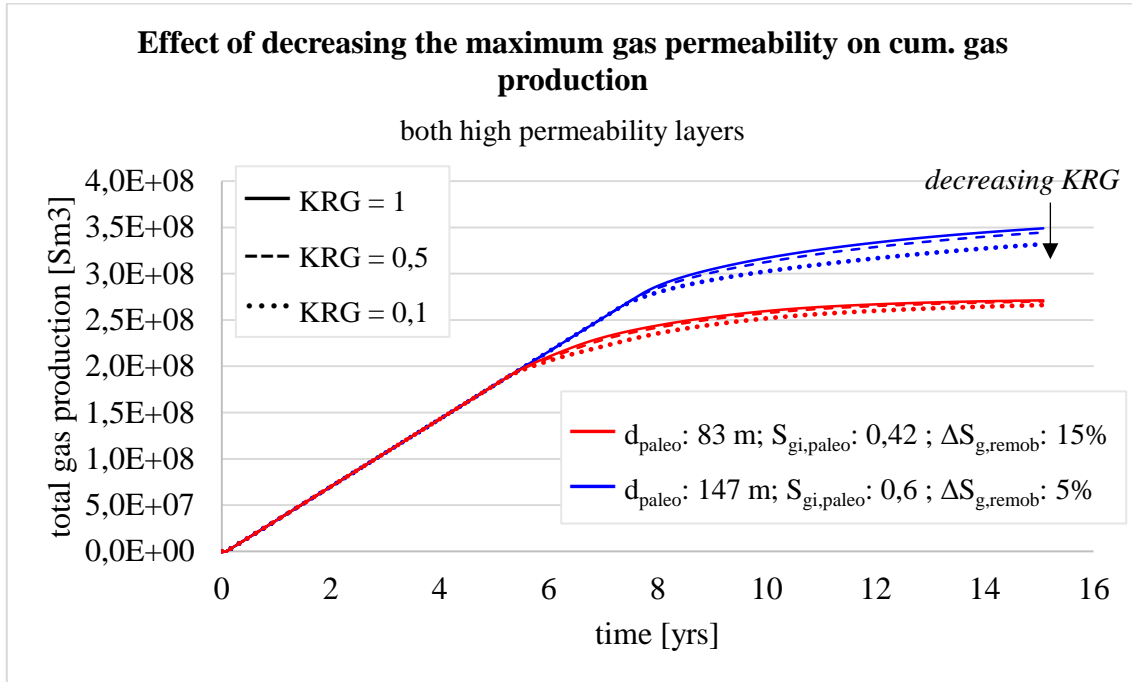


Figure 6.2-9: Cum. gas production vs time related to lower KRG (dashed): reduction of KRG to 0,5 (0,1) leads to a decrease in the cumulative gas production.

Table 6.2-2: Preliminary recovery potential of paleo gas (KRG = 0,5).

Scenarios	Total gas production [MSm <sup>3</sup> ]	Increment [MSm <sup>3</sup> ]	Increment	Reduction* with KRG = 0,5
No paleo gas	226	-	-	-
pessimistic	270	44	+19 %	-1 %
optimistic	345	119	+53 %	-2 %

\*compared to KRG = 1 in Table 6.2-1

Table 6.2-3: Preliminary recovery potential of paleo gas (KRG = 0,1).

Scenarios	Total gas production [MSm <sup>3</sup> ]	Increment [MSm <sup>3</sup> ]	Increment	Reduction* with KRG = 0,1
No paleo gas	226	-	-	-
pessimistic	266	40	+18 %	-2 %
optimistic	332	106	+47 %	-8 %

\*compared to KRG = 1 in Table 6.2-1

### 6.2.3 Water Influx

The first set of analyses of the influence of paleo residual gas saturations on water influx examines the impact on water breakthrough and cumulative water production. During this sensitivity the aquifer behavior was kept constant.

Firstly, the effect of  $d_{\text{paleo}}$  and  $S_{\text{gi,paleo}}$  on cumulative water production has been assessed. Figure 6.2-10 shows the cumulative water production over time for different  $d_{\text{paleo}}$  and for all  $\Delta S_{\text{g,remob}}$  with a constant  $S_{\text{gi,paleo}}$  of 0,42. In the same manner, Figure 6.2-11 (Figure 6.2-12) illustrates the same behavior for a constant  $S_{\text{gi,paleo}}$  of 0,5 (0,6).

From the three figures can be seen that:

- the cumulative water production increases with increasing  $d_{\text{paleo}}$ .

This finding was also reported by Taggart (2019).

- the cumulative water production decreases with increasing  $S_{\text{gi,paleo}}$ .

In reviewing the literature, no data was found on the association between  $S_{\text{gi,paleo}}$  and cumulative water production.

- the cumulative water production becomes more sensitive towards  $\Delta S_{\text{g,remob}}$  with increasing  $d_{\text{paleo}}$  and with decreasing  $S_{\text{gi,paleo}}$ .

Also, this correlation was not found in reviewing the literature.

The figures further show, the total water production depends on the  $\Delta S_{\text{g,remob}}$ . This correlation was not encountered to be discussed in the literature.

- With increasing  $\Delta S_{\text{g,remob}}$  increases the total water production.
- Applying any  $\Delta S_{\text{g,remob}}$  causes earlier water breakthrough than applying no  $d_{\text{paleo}}$   $S_{\text{gi,paleo}}$   $\Delta S_{\text{g,remob}}$ .

The water breakthrough observed seems not to be dependent on the height of  $\Delta S_{\text{g,remob}}$ . What can be said is, that

- a significantly later water breakthrough is observed when no  $\Delta S_{\text{g,remob}}$  is applied.

Contrary to expectations, this first analysis did not find a significant correlation between  $S_{\text{gi,paleo}}$  and water breakthrough.



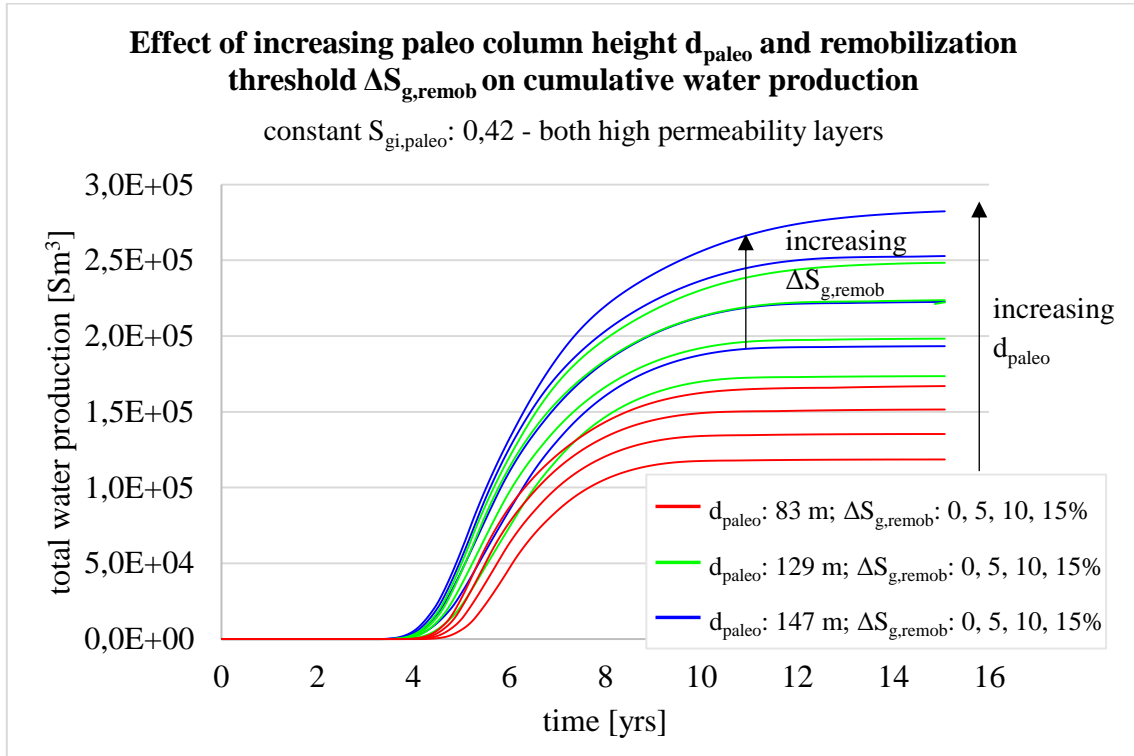


Figure 6.2-10: Cum. water production vs. time for  $S_{gi,paleo}$  0,42: cum. water production increases with increasing  $d_{paleo}$ , becomes more sensitive towards  $\Delta S_{g,remob}$  with increasing  $d_{paleo}$  and with decreasing  $S_{gi,paleo}$ .

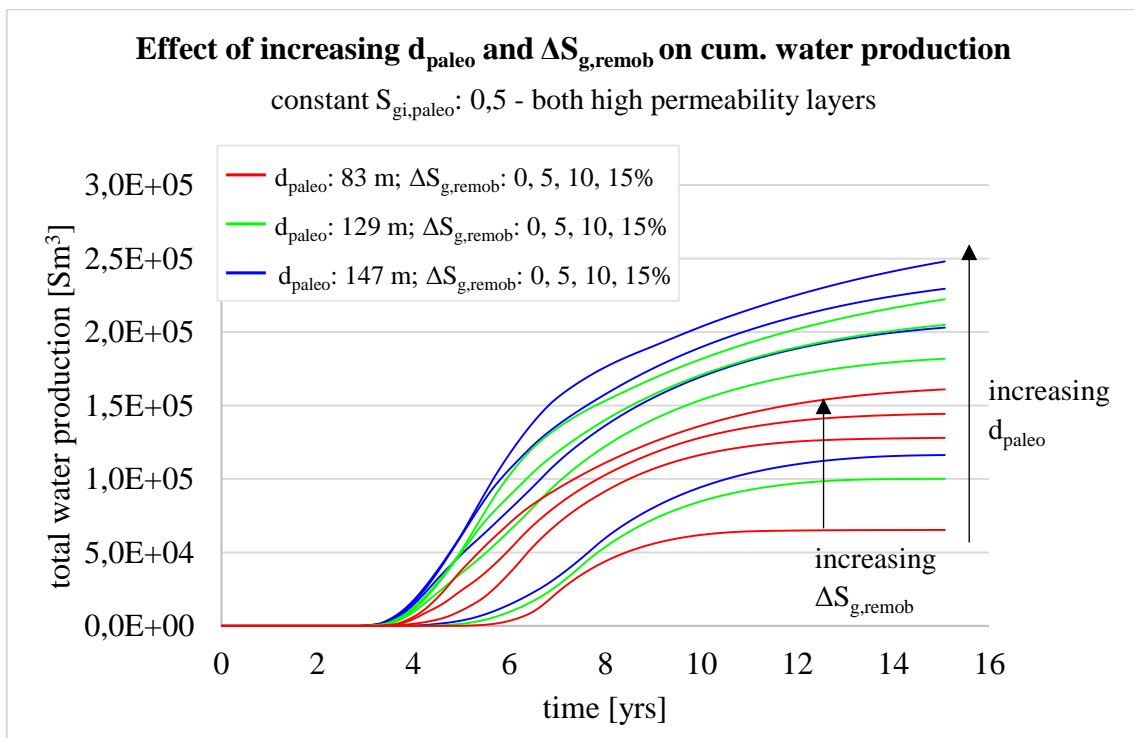


Figure 6.2-11: Cum. water production vs. time for  $S_{gi,paleo}$  0,5: cum. water production increases with increasing  $d_{paleo}$ , becomes more sensitive towards  $\Delta S_{g,remob}$  with increasing  $d_{paleo}$  and with decreasing  $S_{gi,paleo}$ .

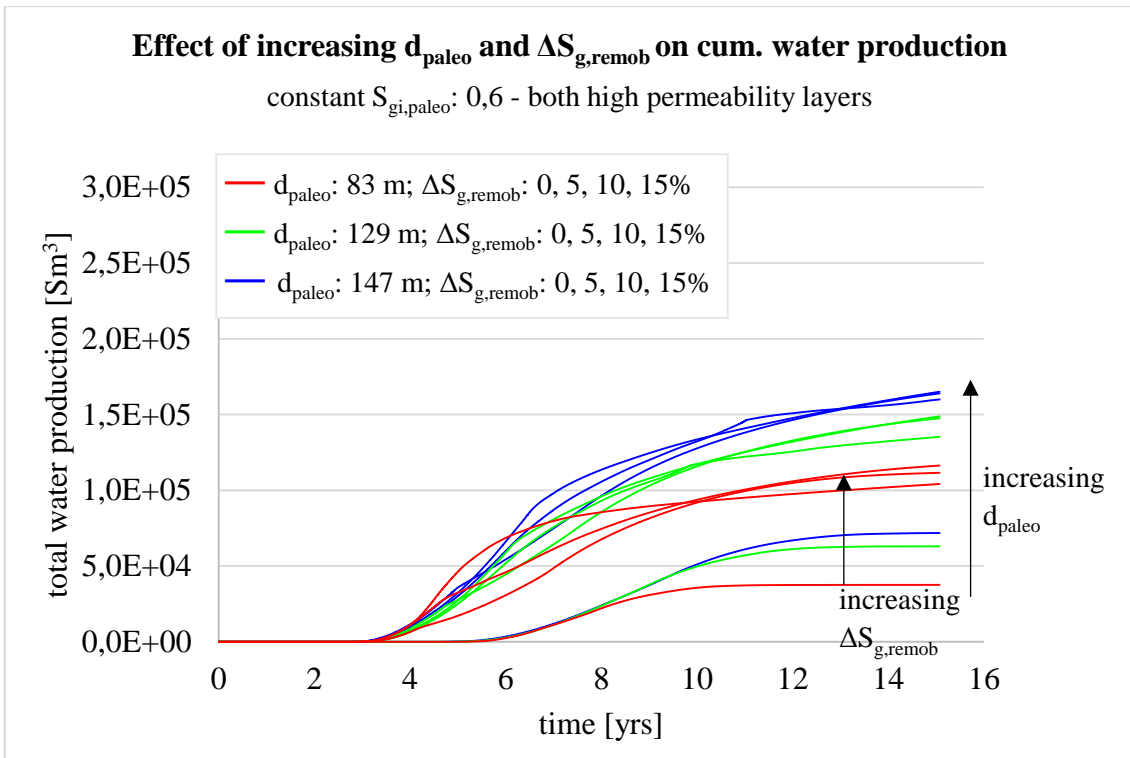


Figure 6.2-12: Cum. water production vs. time for  $S_{gi,paleo}$  0,6: cum. water production increases with increasing  $d_{paleo}$ , becomes more sensitive towards  $\Delta S_{g,remob}$  with increasing  $d_{paleo}$  and with decreasing  $S_{gi,paleo}$ .

The present study was further designed to determine the effect of the high permeability layers in the field on the water influx facing paleo gas production.

Figure 6.2-13 compares the effect of permeability layers on water production over time dependent on for  $d_{paleo}$  and  $\Delta S_{g,remob}$ . In the case of absent high permeability layers occurs a delayed and less pronounced water breakthrough.

It is clearly visible, that the absence of both upper and lower high permeability layer delays the water breakthrough significantly by circa 12 months. How pronounced the water breakthrough is, is further dependent on  $d_{paleo}$  and  $\Delta S_{g,remob}$ . With higher  $d_{paleo}$  and with higher  $\Delta S_{g,remob}$  increases the peak of the water breakthrough.

The presence of the both high permeability layers in comparison to only the upper high permeability layer is insignificant for water breakthrough.

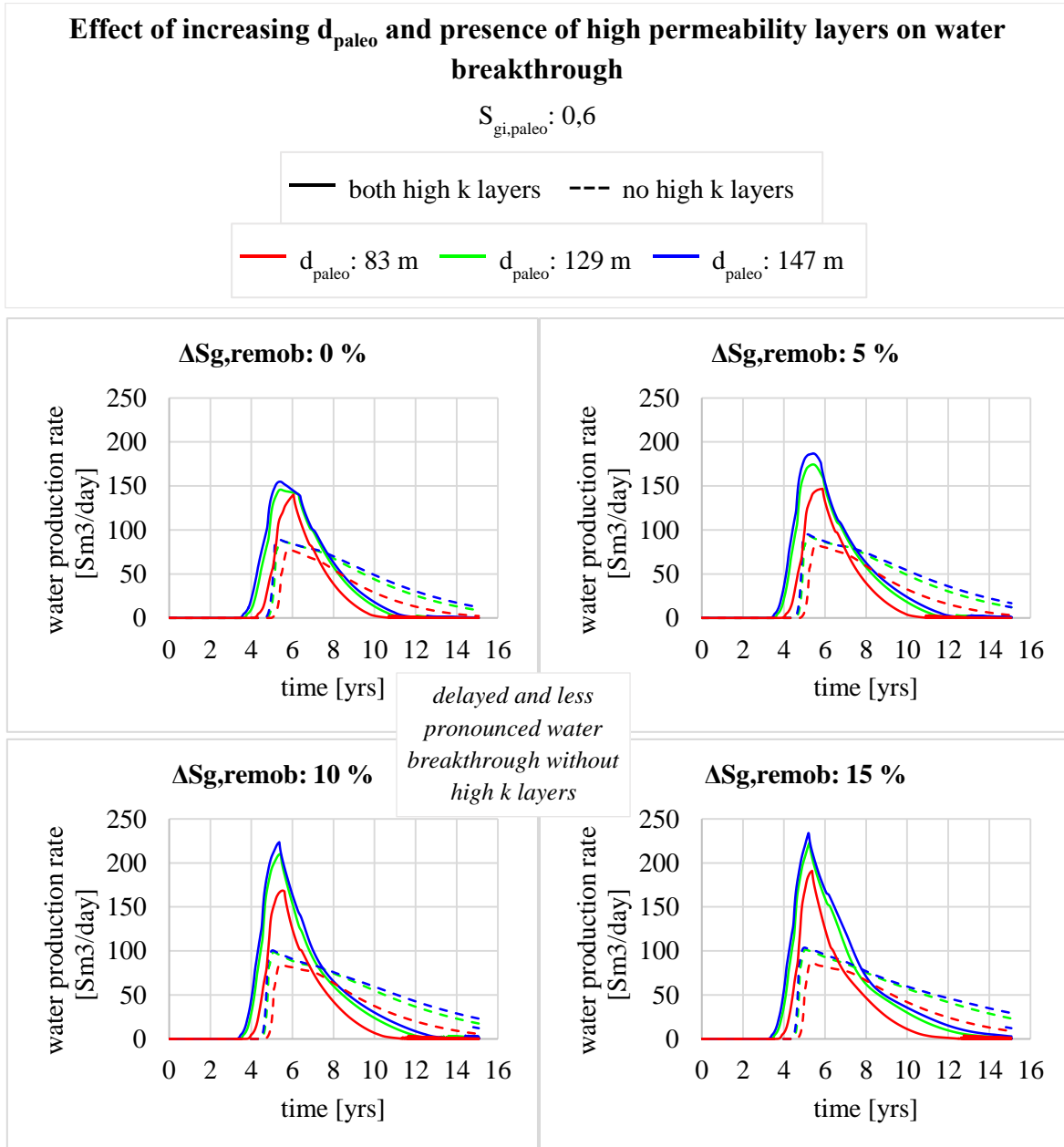


Figure 6.2-13: Water production vs. time with constant  $S_{gi,paleo}$  of 0,42: presence of high permeability layers causes earlier and stronger water breakthrough.

These finding, while preliminary, suggests that

- the horizontal permeability controls the velocity of the water invasion. The high permeability layers seem to act as highly prolific layers for water production.

This finding was also reported by Boya Ferrero et al., (2018).

To quantify the water influx risk in the presence of both high permeability layers, the end members of the sensitivity study were chosen, representing the most optimistic and the most pessimistic case with regards to water production.

As most optimistic case the case with the lowest  $d_{paleo}$  (83 m), the highest  $S_{gi,paleo}$  (0,6) and the lowest  $\Delta S_{g,remob}$  (+0,05) has been identified. Additionally, the same optimistic case has been added without taking into account  $\Delta S_{g,remob}$ .

For most pessimistic case the case with the highest  $d_{paleo}$  (147 m), the lowest  $S_{gi,paleo}$  (0,42) and the highest  $\Delta S_{g,remob}$  (+0,15) has been identified. The results have additionally been compared with the case without paleo gas saturations.

Overall, lowest total water production has been encountered in the cases without  $\Delta S_{g,remob}$ .

The results of this analysis are provided in Table 6.2-4 showing an increase in cumulative water production of minimum 0,09 MSm<sup>3</sup> up to maximum 0,26 MSm<sup>3</sup> compared to having no residual gas column below free water level (total 0,02 MSm<sup>3</sup>). Disregarding  $\Delta S_{g,remob}$  leads to a water production decrease of 0,075 MSm<sup>3</sup> from the optimistic case and causes a total incremental water production of only 0,015 MSm<sup>3</sup> compared to the case without paleo gas.

Table 6.2-4: Water influx due to paleo residual gas.

Scenarios	Total water production [kSm <sup>3</sup> ]	Increment [kSm <sup>3</sup> ]
no paleo gas	21,6	-
optimistic	111,6	90
<i>no threshold (optimistic)</i>	36,6	15
pessimistic	282,4	260,8

Contrary to expectations, this first analysis did not find a significant correlation between  $S_{gi,paleo}$  and water breakthrough. It has been suggested that by Woods, et al. (2012) that higher  $S_{gi,paleo}$  cause higher reduction in water mobility. This does not appear to be the case, even if this behavior is reflected in the endpoints for the maximum water relative permeability in the present study: Whereas the maximum water relative permeability is 1 in the aquifer, the water relative permeability in the paleo column is reduced to 0,307, see sub-sub-chapter 5.2.2.

The encountered issue brings up the question after the origin of the produced water. The produced water can either be expelled from the paleo residual gas leg or originate from the aquifer. Therefore, the aquifer behavior needs to be investigated and aquifer strength is increased in the next steps to understand its influence on the water production.

Comparing Figure 6.2-14 (total aquifer production over time) with Figure 6.2-15 (total water production over time) gives the following insights:

The highest aquifer influx is experienced in the case without paleo gas. However, the cumulative water production for this case is the lowest compared to the other cases. This might indicate, that

- water production in the paleo gas cases is less related to the aquifer influx but might be result of water expulsion due to gas expansion before remobilization.

The water expulsion is determined by different parameters. As can be seen, when comparing the aquifer influx of the cases with constant  $\Delta S_{g,remob}$  and  $S_{gi,paleo}$  but different  $d_{paleo}$ , a smaller  $d_{paleo}$  is connected to higher aquifer influx but lower total water production. This suggests

- more water expulsion is encountered with higher  $d_{paleo}$ .

In reviewing the literature, no data was found on the association between paleo gas columns and the origin of the produced water. Taggart (2019) merely indicates an increased risk of water production, displaced from paleo gas expansion upon pressure depletion.

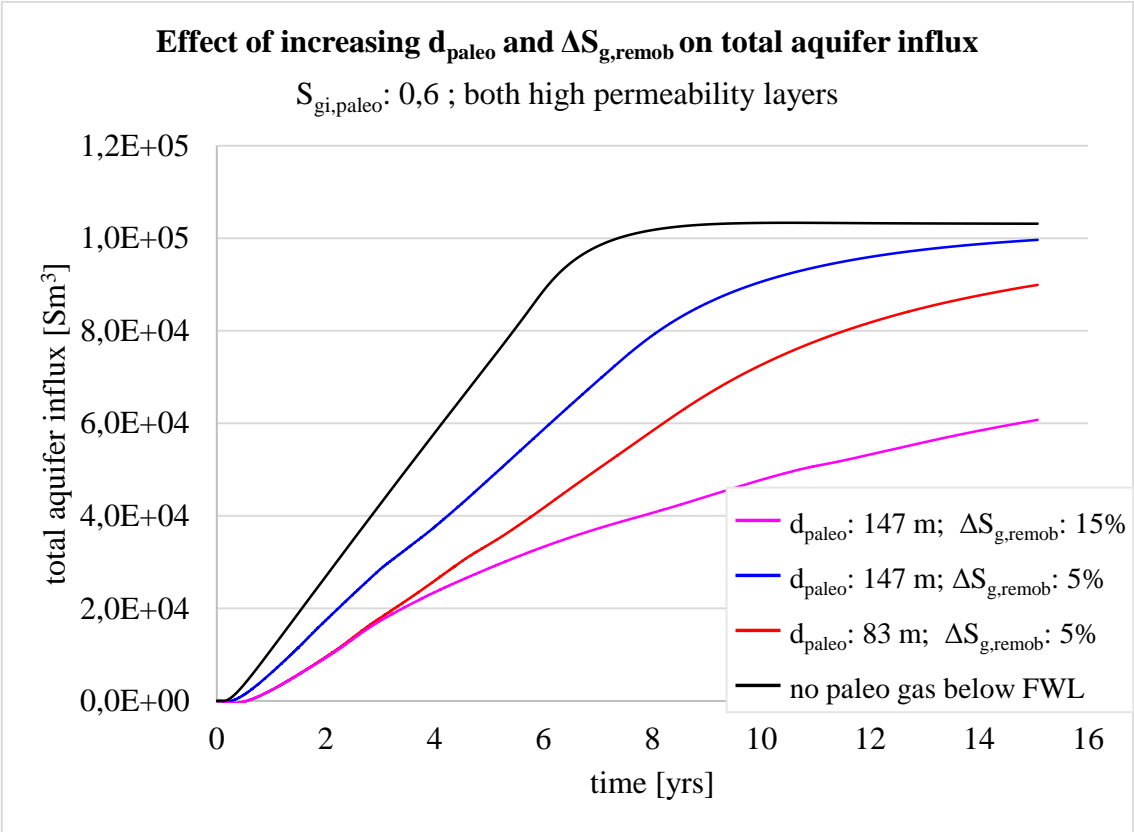


Figure 6.2-14: Total aquifer production vs. time: smaller  $d_{paleo}$  is connected to higher aquifer influx; higher  $\Delta S_{g,remob}$  leads to lower aquifer influx.

An influence factor on total aquifer influx is the  $\Delta S_{g,remob}$ . When comparing the aquifer influx of the cases with constant  $d_{paleo}$  and  $S_{gi,paleo}$  but different  $\Delta S_{g,remob}$ , higher  $\Delta S_{g,remob}$  is connected to lower aquifer influx but equal total water production.

- Higher  $\Delta S_{g,remob}$  leads to higher pressure support in the field (see Figure 6.2-16) due to gas expansion before remobilization and hence lowers the pressure difference in the aquifer, which determines its productivity.

The total water production of the two cases reaches equal levels regardless. It could be argued that the comparable levels are achieved due to balancing between aquifer influx and water expulsion, depending on  $\Delta S_{g,remob}$ .

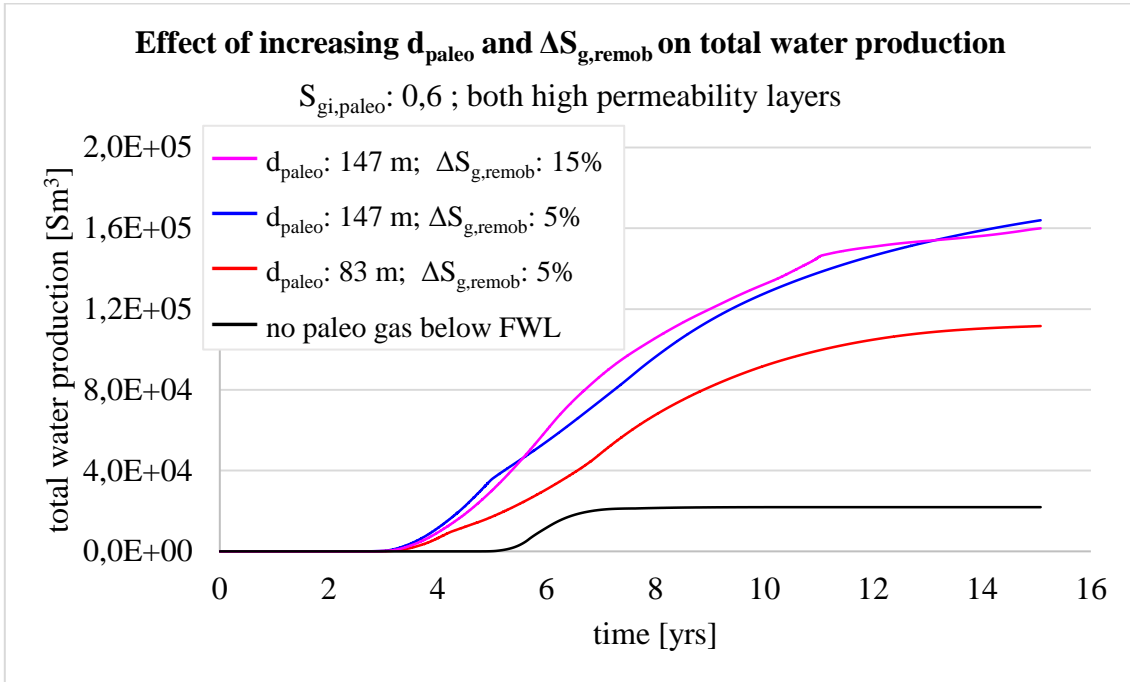


Figure 6.2-15: Total water production vs. time: smaller  $d_{paleo}$  is connected to lower total water production.

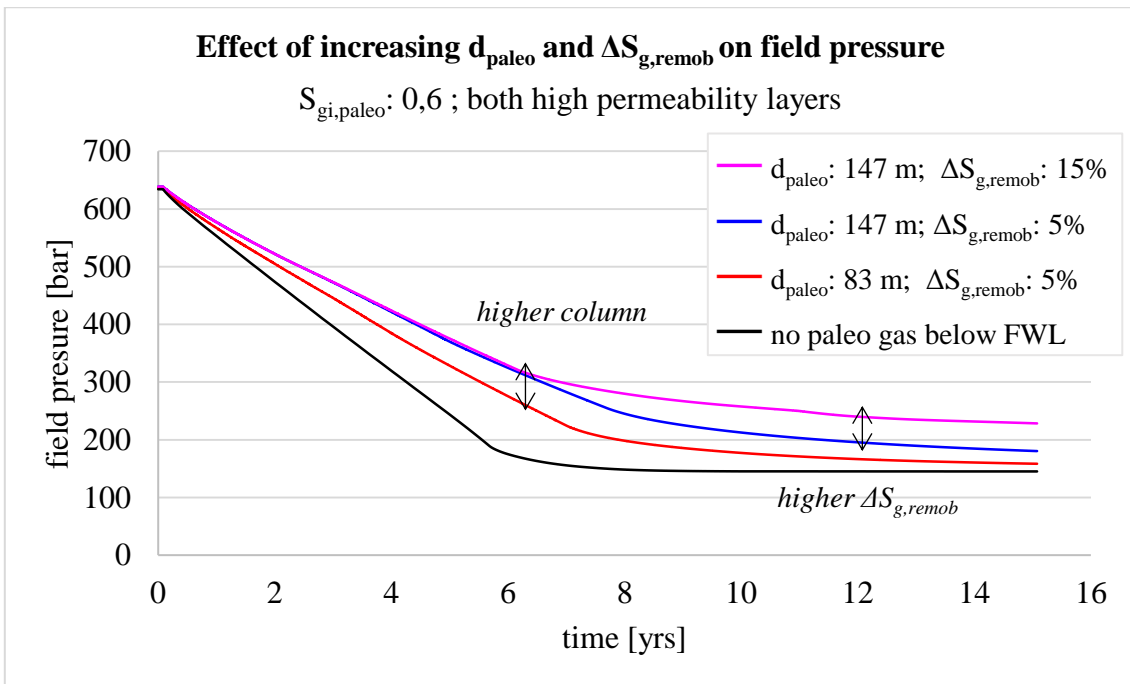


Figure 6.2-16: Field pressure vs. time: higher  $\Delta S_{g,remob}$  leads to higher pressure support.

To understand the influence of a strong aquifer system in comparison to a weak aquifer system (post-PDO reference case), the aquifer model was modified to reach a strong aquifer behavior, see Table 6.2-5: a doubled initial water volume in the aquifer  $V_{w0}$  (from  $7,1E6$  to  $14,2E6$   $Sm^3$ )

connected to a total compressibility  $c_t$  of the aquifer increased by 2,5 (from 3E-5 to 7,5 E-5 1/bar) increases the total aquifer influx substantially, see Table 6.2-6.

Changing the productivity index has a neglectable effect for this strongly expansion driven system and was therefore disregarded.

Table 6.2-5: Aquifer parameters for weak and strong aquifer behavior.

Parameter		Weak aquifer	Strong aquifer
$V_{w0}$	$\text{Sm}^3$	7,1 E6	14,26
$c_t$	1/bar	3 E-5	7,5 E-5
J	$\text{Sm}^3/\text{day}/\text{bar}$	250	250

Applying the same changes of the aquifer parameters shows different sensitivity on the resulting total aquifer production: The highest increase of the total aquifer production is observed for the case without paleo gas. The lowest increase in total aquifer production the paleo case with the higher  $\Delta S_{g,\text{remob}}$ . These effects can again be explained by the pressure support due to gas expansion before remobilization, which is has already been illustrated in Figure 6.2-16.

Table 6.2-6: Effect of aquifer influx on total water production water (both high permeability layers).

	Weak aquifer total influx		Strong aquifer total influx	
	cum. aquifer influx [ $\text{kSm}^3$ ]	cum. water production [ $\text{kSm}^3$ ]	cum. aquifer influx [ $\text{kSm}^3$ ]	cum. water production [ $\text{kSm}^3$ ]
No paleo gas	103	22	506	388
4447 – 0,6 – 0,15	61	161	110	191
4447 – 0,6 – 0,05	90	164	359	325

(column –  $S_{g,\text{paleo}} - \Delta S_{g,\text{remob}}$ )

Figure 6.2-17 presents a detail excerpt of cumulative water production over time subjected to aquifer strength. The stronger aquifer causes an earlier water breakthrough for all cases. What stands out in the figure is, the earlier water breakthrough due to stronger aquifer behavior of the case without paleo gas is extremely high (ca. 19 months) compared to the paleo gas cases. This finding confirms that the

- water breakthrough in the presence of paleo gas is associated with water expulsion due to gas expansion before remobilization instead of aquifer influx.

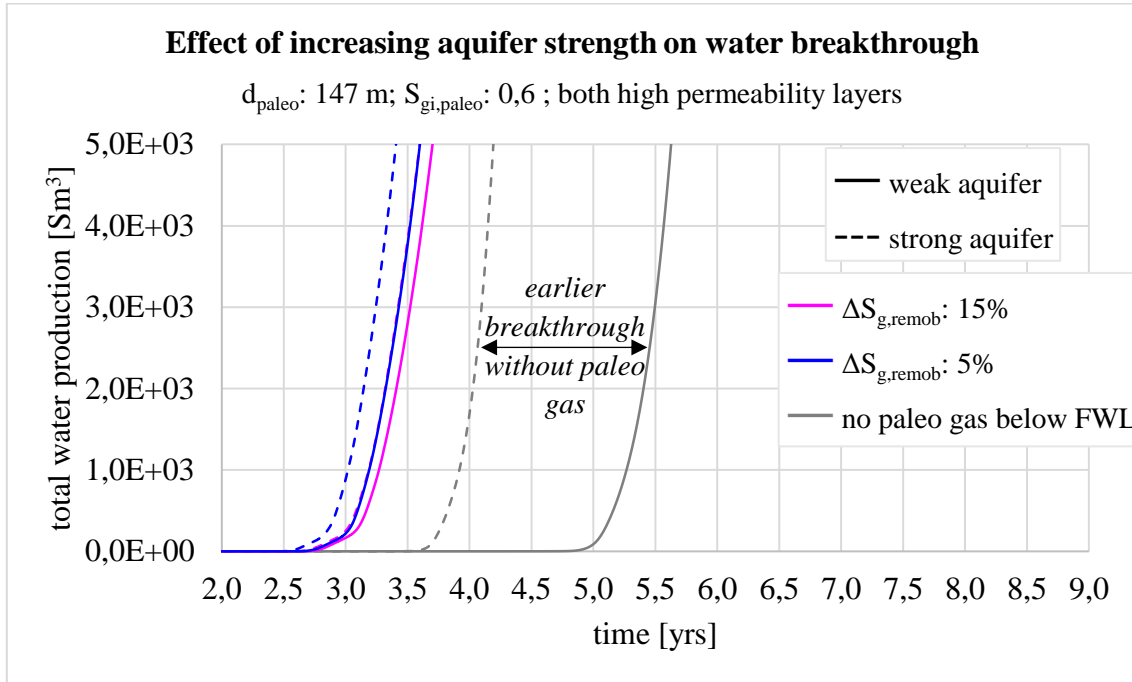


*Figure 6.2-17: Detail of cum. water production vs. time vs aquifer strength: earlier water breakthrough due to stronger aquifer behavior of the case without paleo gas is extremely high compared to the paleo gas cases.*

Another effect leading to a less significant effect of aquifer influx on water break through is the reduction of water mobility due to gas saturation in the paleo column, see Figure 6.2-18. It is evident from the figure, that the relative water permeability is constantly as high as 1 in the case without paleo gas.  $K_{\text{rw}}$  changes over time with saturation for the paleo gas cases.  $K_{\text{rw}}$  drops to 0,008 in the  $\Delta S_{\text{g,remob}}$  of 0,05 case, and even further to 0,0015 in the  $\Delta S_{\text{g,remob}}$  of 0,15 case.

- Paleo gas presence reduces relative water permeability in paleo gas column.
- A higher  $\Delta S_{\text{g,remob}}$  maintains a higher gas saturation in the paleo gas column over time, which leads to decreased water mobility.

These results reflect those of Woods, et al. (2012).



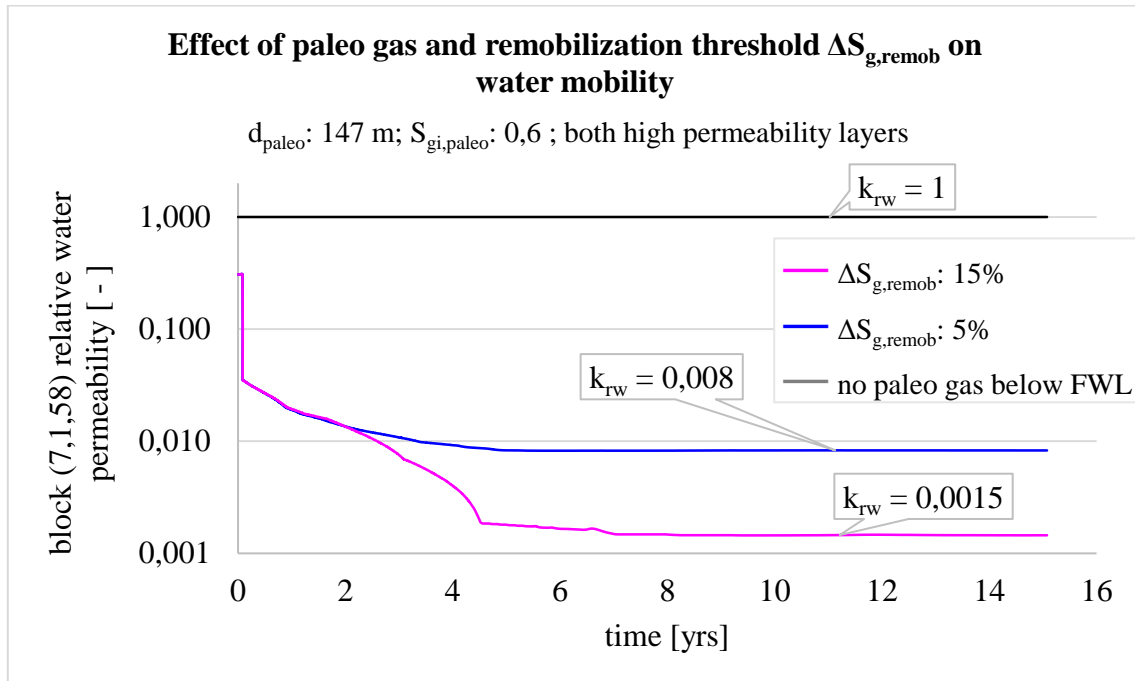


Figure 6.2-18: Log. relative water permeability vs. time: presence of paleo gas reduces water relative permeability substantially.

The last question in this part of the research was how the field specific high permeability layers would influence the water production exposed to weak and strong aquifer behavior. It has already been discussed earlier, that the absence of these high permeability layers delays water breakthrough and reduces water production rates.

Table 6.2-7 gives an overview of the effect of absence of the high permeability layers on the aquifer production and total water production in the weak and strong aquifer case. For data in presence of the high permeability layers refer to Table 6.2-6.

It can be seen, that independent of the aquifer behavior, the absence of the high permeability layers leads to less total water production. This observation is partially connected to an equivalent reduction to aquifer production linked to the absence of the permeability layers.

Table 6.2-7: Effect of aquifer influx on total water production water (no high permeability layers).

	Weak aquifer total influx		Strong aquifer total influx	
	<b>cum. aquifer influx</b>	<b>cum. water production</b>	<b>cum. aquifer influx</b>	<b>cum. water production</b>
	[kSm <sup>3</sup> ]	[kSm <sup>3</sup> ]	[kSm <sup>3</sup> ]	[kSm <sup>3</sup> ]
No paleo gas	103	10	465	329
4447 – 0,6 – 0,15	45	10	159	55
4447 – 0,6 – 0,05	77	52	270	152

(column – S<sub>gi,paleo</sub> – ΔS<sub>g,remob</sub>)

The high permeability layers lead as reflected earlier to higher productivity of the reservoir and cause henceforth a larger pressure drop. Due to this higher pressure drop, the aquifer influx in the presence of the high permeability layers is higher than in their absence.

This increased productivity is also evident when examining the water breakthrough with and without high permeability layers, see Figure 6.2-19. Water breakthrough is significantly delayed without high permeability layers. The delay for the case without paleo gas is circa 8 months and 44 months resp. 48 months for the paleo cases with  $\Delta S_{g,remob}$  of 0,05 or 0,15 respectively.

Note again, the differences in water breakthrough in paleo gas cases compared to the case without paleo gas is primarily related to expelled water from the paleo column during gas expansion before remobilization and not aquifer influx.

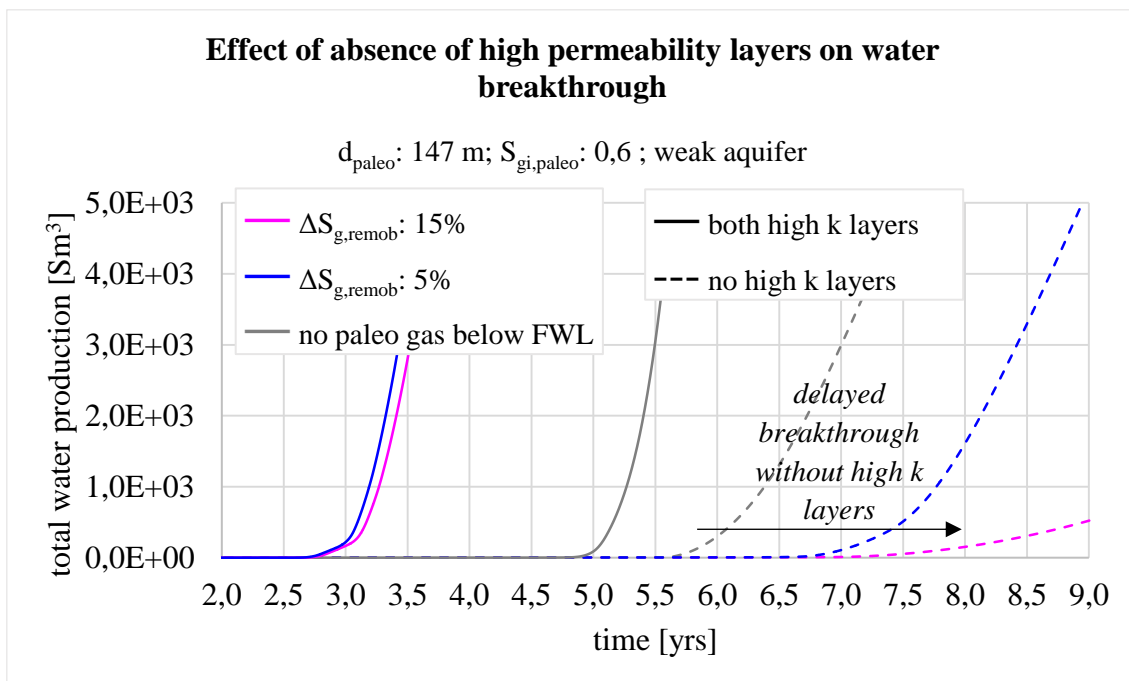


Figure 6.2-19: Detail of cum. water production vs. time: delayed water breakthrough in the absence of high permeability layers.

These results further support the idea of that the horizontal permeability controls the velocity of the water invasion. This finding has important implications for well development: high permeability layers increase the risk of water cusping due to faster water influx no matter origin of the water. This might lead to liquid charging problems in wells, if not accounted for. These results are consistent with the study of Boya Ferrero et al., (2018).

### 6.3 Limitations and Further Work

Further data collection is required to determine exactly how the paleo residual saturation affects the ultimate recovery and the water influx of the full field.

### 6.3.1 *Experimental Data*

All in all, the findings from the imbibition and depletion simulation are limited by the experimental setup of the SCAL experiments from 2013. A note of caution is due here since the experiments, which are the main data origin for the simulations, do not allow to distinct clearly between capillary and advective forces.

Moreover, the SCAL experimental data this thesis is based on originates from experiments conducted with nitrogen. Nitrogen might have shown different behavior than an actual reservoir gas sample or a sample, which is close to the composition of the reservoir gas. The ongoing experiments are conducted with methane and will therefore add substantially to the reliability of the model results when implemented.

Furthermore, the pressure conditions in the experiments were significantly lower than in the reservoir. This adds another factor of uncertainty, that can be challenged with the incoming data since the ongoing experiments are conducted at pressure levels close to reservoir conditions.

Further experimental data required to validate assumptions and quality-check present limitations, can be summarized as:

- Residual gas saturation  $S_{gr}$  dependent on rock type
- Critical gas saturation  $S_{gc}$  dependent on rock type
- Secondary drainage relative permeability functions (major KRG and KRW, minor  $N_g$  and  $N_w$ )
- Secondary drainage capillary pressure functions

### 6.3.2 *Simulations*

A major source of uncertainty is in the assumption of rather dry gas with limited liquid drop-out. This assumption justifies the choice of using a dry gas Black-Oil model for simulating the field. The Black-Oil model in ECLIPSE limits the applicable hysteresis models to classical hysteresis model, e. g. Killough and Carlson. Reliability might be increased by transferring to a compositional model and using Hustad's hysteresis model to quality-check the hysteresis influence.

This study was limited by the absence of an actual geology model. A widely simplified geology model has been applied: an uniform porosity and a largely uniform permeability distribution (despite the high permeability layers). Both porosity and permeability are average values of the actual distribution over the full field.

Therefore, the following behavior was not captured in the study: The residual gas saturation is dependent on rock type and reservoir quality, but a uniform value based on one core has been used. There are indications, that the critical gas saturation is affected by the permeability, but the value was not varied on this dependency. Intervals in the field with extremely low permeability are not captured. They can cause irreversible gas trapping.

Also, the decreasing reservoir quality with depth due to diagenetic influences is not captured in the model. This can primarily have indications for the water production and cause lower water production from the aquifer than this model suggests.

When the production of the field is going to start up, it will also be possible to check the assumption of the presence of both upper and lower high permeability layer and their continuity. Regardless, the study has shown, that neglecting the lower high permeability layer will have only marginal effects on either water influx or recovery potential.

Taken together, the results about the recovery potential suggest that paleo gas saturations can add substantially to the recoverable reserves. Studies which show no effect on the recovery are not generally published. The results about the water influx support an increased water production risk due to paleo gas presence. Again, studies which show no increasing effect on the water production are not generally published.

It was not possible to investigate the incremental production of the paleo gas leg further, nor the associated higher risk of water production, due to the absence of secondary drainage saturation functions for relative permeability as well as capillary pressure.

The secondary drainage relative permeability as source of error has been investigated. Sensitivity analysis showed that the shape of the relative permeability curves has less influence on the recovery, which excludes this source of error.

However, secondary drainage capillary curves were set equal to imbibition curves. Hence it is recommended, to insert secondary drainage capillary pressure as soon as data becomes available.

The scope of this study was limited to a two-dimensional cross-sectional model. Fluid behavior in a three-dimensional environment may differ and therefore it is necessary, to transfer the findings of this thesis into a three-dimensional or directly into the FFM to quantify the paleo residual gas impact water influx and recovery potential. It is recommended to conduct this step after the incoming experimental data has been used to validate the assumptions of the conceptual model.

Further simulation work (based on incoming experimental data to validate assumptions and quality-check for data limitations) can be summarized as:

- Include experimentally determined secondary drainage relative permeability
- Include experimentally determined secondary drainage capillary pressure
- Include experimentally determined remobilization threshold
- Quality-check hysteresis simulation by transferring to a compositional model and using Hustad's hysteresis model.
- Include paleo residual gas saturations in the FFM (as soon as data limitations are reduced with incoming data) to quantify the paleo residual gas impact water influx and recovery potential for the full field.

## 7 CONCLUSIONS

The present thesis has started with a literature review that revealed the importance of the remobilization threshold ( $\Delta S_{g,remob}$ ) and gave an estimate for it for the sensitivity study. An one-dimensional core model has been used to derive reliable saturation functions from experimental data. A two-dimensional conceptual model has been used to assess the paleo residual gas impact on water influx and recovery potential. Amongst others, different paleo column height ( $d_{paleo}$ ) scenarios have been tested as well as different initial gas saturations in the paleo column ( $S_{gi,paleo}$ ) and different  $\Delta S_{g,remob}$ . Field-specific parameters, e.g. the high permeability layers, justify implications of the general results for the field case. Limitations regarding the lack of secondary drainage experimental data, the simplified geological model and the limit to a two-dimensional model have been discussed. The analysis leads to the following conclusions:

### 7.1 Literature Study

- Due to geological movements (e. g. charge breach after gas charge), aquifer encroachment can cause imbibition processes in the reservoir. When water invades the gas bearing zone, gas becomes trapped behind the waterfront in a discontinuous phase.
- The magnitude of the trapped residual gas saturation ( $S_{gr}$ ) is governed by reservoir quality and rock type.  $S_{gr}$  decreases with decreasing shale volume, decreasing cementation and increasing sorting and grain size.  $S_{gr}$  increases with increasing initial gas saturation.
- Remobilization of trapped gas saturations is a cyclic process, which needs to be considered by hysteresis. Remobilization by pressure depletion is possible after overcoming  $\Delta S_{g,remob}$ . This saturation increase is necessary to reconnect the discontinuous gas phase. Accordingly, this process is to be modeled with secondary drainage saturation functions to obey  $\Delta S_{g,remob}$ .
- $\Delta S_{g,remob}$  varies from less than 5 % up to 15 % of increase of  $S_{gr}$  before remobilization. There is no correlation between permeability and  $\Delta S_{g,remob}$ .

### 7.2 Simulation Study

#### 7.2.1 Initialization

Paleo residual gas columns can be initialized by using negative  $P_c$  (imbibition) and hydrostatic equilibrium option.

- $d_{paleo}$  is determined by the level of the negative capillary pressure and can be computed with the density difference between gas and water.
- Endpoints govern  $S_{gi,paleo}$ .
- Killough's hysteresis model for relative permeability is able to satisfy  $\Delta S_{g,remob}$ .

#### 7.2.2 Recovery Potential

Paleo gas saturations add to recovery potential during depletion depending on  $d_{paleo}$ ,  $S_{gi,paleo}$  and  $\Delta S_{g,remob}$ .

- Larger  $d_{paleo}$  lead to an increased cumulative gas production.
- Higher  $S_{gi,paleo}$  increase cumulative gas production

- Higher  $\Delta S_{g,remob}$  cause earlier fall off of the production plateau and hence reduce cumulative gas production.
- Disregarding  $\Delta S_{g,remob}$  leads to overestimation of the recovery potential.
- In this conceptual study an incremental production of 20 % to 55 % is possible depending on the mentioned influence factors compared to having no paleo gas present. Reduction in maximum gas relative permeability can reduce this increment to 18 % or 47 % respectively.

### 7.2.3 Water Influx

Paleo gas saturations increase the water production risk under depletion depending on  $d_{paleo}$ ,  $S_{gi,paleo}$  and  $\Delta S_{g,remob}$ .

- Larger  $d_{paleo}$  lead to an increase cumulative water production.
- Lower  $S_{gi,paleo}$  increase cumulative water production.
- Higher  $\Delta S_{g,remob}$  cause higher cumulative water production. Disregarding  $\Delta S_{g,remob}$  leads to water production underestimation.

Water breakthrough is affected by paleo residual gas depending on  $\Delta S_{g,remob}$  and  $d_{paleo}$ .

- Any  $\Delta S_{g,remob}$  cause earlier water breakthrough than applying no  $\Delta S_{g,remob}$ . The water breakthrough observed is not dependent on the height of  $\Delta S_{g,remob}$ .
- A significantly later water breakthrough is observed when no  $\Delta S_{g,remob}$  is applied.
- A significantly later water breakthrough is observed when no paleo gas is present.

The water produced in this model originates from two different regions: inflowed from the aquifer and expelled from the paleo gas column by depletion induced gas expansion before remobilization.

- Water production in the paleo gas cases is less related to the aquifer influx but more result of water expulsion from the paleo gas column.
- Stronger water expulsion is experienced with higher  $d_{paleo}$ .
- Stronger water expulsion is experienced with higher  $\Delta S_{g,remob}$ .
- Water breakthrough in the presence of paleo gas is associated with water expulsion from the paleo gas column instead of aquifer influx.

The influence of the aquifer is affected by the presence of paleo residual gas.

- Higher  $\Delta S_{g,remob}$  cause lower aquifer influx due to higher pressure support by gas expansion before remobilization.
- $S_{gr}$  in the paleo column cause reduction in water mobility and hence counteract aquifer influx. A higher reduction is achieved with higher  $\Delta S_{g,remob}$ .

### 7.3 Implications for Field Case

The field-specific implications of the simulation study can be summarized as follows:

Increased recovery potential:

- Increase in total production of minimum 20 % ( $d_{\text{paleo}} 83 \text{ m} - S_{\text{gi,paleo}} 0,42 - \Delta S_{\text{g,remob}} 0,15$ ) up to maximum 55 % ( $d_{\text{paleo}} 147 \text{ m} - S_{\text{gi,paleo}} 0,6 - \Delta S_{\text{g,remob}} 0,05$ ) compared to having no residual gas below FWL.
- Falsely neglecting  $\Delta S_{\text{g,remob}}$  of the maximum case causes a total incremental production of 74 % compared to the case without paleo gas.

Increased water influx:

- Increase in cumulative water production of minimum 450 % ( $d_{\text{paleo}} 147 \text{ m} - S_{\text{gi,paleo}} 0,42 - \Delta S_{\text{g,remob}} 0,15$ ) up to maximum 1300 % ( $d_{\text{paleo}} 83 \text{ m} - S_{\text{gi,paleo}} 0,6 - \Delta S_{\text{g,remob}} 0,05$ ) compared to having no residual gas column below free water level.
- Falsely neglecting  $\Delta S_{\text{g,remob}}$  of the minimum case causes a total incremental water production of only 75 % compared to having no paleo gas below FWL.
- In the field-specific weak aquifer case, the counteracting effect of water mobility reduction in the paleo column is less significant for reducing the water production from aquifer influx. Water production is less related to aquifer influx but more result of water expulsion from the paleo column.

Influence of high permeability layers:

- The presence of the high permeability layers for the paleo gas bearing cases with  $\Delta S_{\text{g,remob}}$  shows an increase in the total gas production.
- Horizontal permeability controls the velocity of the water invasion.
- High permeability layers increase the total water production. Water breakthrough appears significantly earlier and more pronounced with high permeability layers.
- Effects show no sensitivity to removing the lower high permeability layer.

## BIBLIOGRAPHY

- Adams, S. (2003). Modeling Imbibition Capillary Pressure Curves. *SPE Annual Technical Conference and Exhibition*. Society of Petroleum Engineers.
- Ahmed, T. (2006). *Reservoir Engineering Handbook* (Third Edition). Gulf Professional Publishing.
- Babadimas, J. M. (2017). Modelling Trapped Gas Expansion in Water-Drive Reservoirs. *SPE/IATMI Asia Pacific Oil & Gas Conference and Exhibition*. Society of Petroleum Engineers.
- Boya Ferrero, M., Wahaibi, I., Elshehabi, M., Farsi, A., Winchester, A., & Aziz, A. (2018). The Hidden Threat of Irreversible Water Blockage in Low Porosity Gas Fields: Learnings from Pre-Production Paleo-Imbibition for Post-Production Field Management in Oman. *SPE Europec Featured at 80th EAGE Conference and Exhibition*. Society of Petroleum Engineers.
- Cable, A., Mogford, D., & Wannell, M. (2004). Mobilization of Trapped Gas from below the Gas-Water Contact. *Paper SCA 2004-29 Presented at the Society of Core Analysts Symposium, Abu Dhabi, 5–9*.
- Carlson, F. M. (1981). Simulation of Relative Permeability Hysteresis to the Nonwetting Phase. *SPE Annual Technical Conference and Exhibition*. Society of Petroleum Engineers.
- Cense, A., Reed, J., & Egermann, P. (2016). SCAL for Gas Reservoirs: A Contribution for better Experiments. *Paper SCA2016-23 Presented at the International Symposium of the Society of Core Analysts Held in Snowmass, Colorado, USA, 21–26*.
- Cross, K., Warren, E., Walker, G., Hospedales, A., & Partap, R. (2008). *Distribution and Origin of Palaeo-Residual Gas in the Columbus Basin*. Presented at the Tobago Gas Technology Conference, Tobago.
- Dake, L. P. (1983). *Fundamentals of Reservoir Engineering*. Elsevier.
- DEA Norge AS. (2016a). *PDO Part 1*. (Plan of Development and Operations).



- DEA Norge AS. (2016b). *PDO Subsurface Support Document*. (Plan of Development and Operations).
- DEA Norge AS. (2019). *Petrophysical Residual Gas Analysis*.
- Domenico, Sn. (1974). Effect of Water Saturation on Seismic Reflectivity of Sand Reservoirs encased in Shale. *Geophysics*, 39(6), 759–769.
- Egermann, P., Schaaf, T., & Bréfort, B. (2010). A Modified Hysteresis Relative Permeability including a Gas Remobilization Threshold for better Production Forecasts of Gas Storages. *Petrophysics*, 51(05).
- Fetkovich, M. J. (1971). A Simplified Approach to Water Influx Calculations-Finite Aquifer Systems. *Journal of Petroleum Technology*, 23(07), 814–828.
- Firoozabadi, A., Olsen, G., & van Golf-Racht, T. (1987). Residual Gas Saturation in Water-Drive Gas Reservoirs. *SPE California Regional Meeting*. Society of Petroleum Engineers.
- Fishlock, T. P., Smith, R. A., Soper, B. M., & Wood, R. W. (1988). Experimental Studies on the Waterflood Residual Gas Saturation and its Production by Blowdown. *SPE Reservoir Engineering*, 3(02), 387–394.
- Hamon, G., Suzanne, K., Billiotte, J., & Trocme, V. (2001). Field-Wide Variations of Trapped Gas Saturation in Heterogeneous Sandstone Reservoirs. *SPE Annual Technical Conference and Exhibition*. Society of Petroleum Engineers.
- Holtz, M. H. (2002). Residual Gas Saturation to Aquifer Influx: A Calculation Method for 3-D Computer Reservoir Model Construction. *SPE Gas Technology Symposium*. Society of Petroleum Engineers.
- Hustad, O. S. (2002). A Coupled Model for Three-Phase Capillary Pressure and Relative Permeability. *SPE Journal*, 7(01), 59–69.

- Hustad, O. S., & Browning, D. J. (2009). A fully coupled three-phase model for capillary pressure and relative permeability for implicit compositional reservoir simulation. *SPE/EAGE Reservoir Characterization & Simulation Conference*, cp-170-00035. European Association of Geoscientists & Engineers.
- Jerauld, G. R. (1997). Prudhoe Bay Gas/Oil Relative Permeability. *SPE Reservoir Engineering*, 12(01), 66–73.
- Killough, J. E. (1976). Reservoir Simulation with History-Dependent Saturation Functions. *Society of Petroleum Engineers Journal*, 16(01), 37–48.
- Kleppe, H., & Andersen, P. Ø. (2019). *Reservoir Simulation—Lecture Notes*. University of Stavanger.
- Kumar, M., Knackstedt, M. A., Senden, T. J., Sheppard, A. P., & Middleton, J. P. (2010). Visualizing and Quantifying the Residual Phase Distribution in Core Material. *Petrophysics*, 51(05).
- Lake, L. W., Johns, R., Rossen, W. R., & Pope, G. A. (2014). *Fundamentals of Enhanced Oil Recovery*.
- Land, C. S. (1968). Calculation of Imbibition Relative Permeability for Two- and Three-Phase Flow from Rock Properties. *Society of Petroleum Engineers Journal*, 8(02), 149–156.
- Lee, W. J., & Wattenbarger, R. A. (1996). *Gas reservoir engineering*.
- Legatski, M. W., Katz, D. L., Tek, M. R., Goring, R. L., & Nielsen, R. L. (1964). Displacement of Gas from Porous Media by Water. *Fall Meeting of the Society of Petroleum Engineers of AIME*. Society of Petroleum Engineers.
- Lenormand, R., Lorentzen, K., Maas, J. G., & Ruth, D. (2017). Comparison of Four Numerical Simulators for SCAL Experiments. *Petrophysics*, 58(01), 48–56.
- Mulyadi, H. (2002). *Determination of Residual Gas Saturation and Gas-Water Relative Permeability in Water-Driven Gas Reservoirs*. Curtin University.

- O'Sullivan, T., Praveer, K., Shanley, K. W., Dolson, J., & Woodhouse, R. (2010). Residual Hydrocarbons-A Trap for the Unwary. *SPE Oil and Gas India Conference and Exhibition*. Society of Petroleum Engineers.
- PetroWiki. (2020a). *Relative Permeability Models*. Retrieved from [https://petrowiki.org/Relative\\_permeability\\_models](https://petrowiki.org/Relative_permeability_models)
- PetroWiki. (2020b). Water Saturation Determination. In *PetroWiki*. Retrieved from [https://petrowiki.org/Water\\_saturation\\_determination](https://petrowiki.org/Water_saturation_determination)
- Schlumberger. (2016). *Eclipse Technical Description*.
- Skjaeveland, S. M., Siqueland, L. M., Kjosavik, A., Hammervold, W. L., & Virnovsky, G. A. (1998). Capillary Pressure Correlation for Mixed-Wet Reservoirs. *SPE India Oil and Gas Conference and Exhibition*. Society of Petroleum Engineers.
- Stratum. (2020). *Preliminary Data—Residual Gas under Depletion*. Stratum Reservoir.
- Taggart, I. (2019). Characterisation and Simulation Insights for Gas Reservoirs with Paleo-Contact. *SPE Europec Featured at 81st EAGE Conference and Exhibition*. Society of Petroleum Engineers.
- Undeland, E. (2012). *Residual Gas Mobility in Ormen Lange*. NTNU: Institutt for petroleumsteknologi og anvendt geofysikk.
- Weatherford. (2013). *SCAL Analysis*. Weatherford Laboratories.
- Woods, C., Conroy, T., Gyllensten, A., Hill, D., & Vallini, D. (2012). Identifying, Quantifying and Modelling Residual Gas. *SPWLA 53rd Annual Logging Symposium*. Society of Petrophysicists and Well-Log Analysts.